Geochemistry of serpentinized and multiphase altered Atlantis Massif peridotites (IODP Expedition 357): Petrogenesis and discrimination of melt-rock vs. fluid-rock processes

Citation for published version:
Whattam, SA, Früh-green, GL, Cannat, M, De Hoog, JCM, Schwarzenbach, EM, Escartin, J, John, BE, Leybourne, MI, Williams, MJ, Rouméjon, S, Akizawa, N, Boschi, C, Harris, M, Wenzel, K, Mccaig, A, Weis, D & Bilenker, L 2021, 'Geochemistry of serpentinized and multiphase altered Atlantis Massif peridotites (IODP Expedition 357): Petrogenesis and discrimination of melt-rock vs. fluid-rock processes', *Chemical Geology*. https://doi.org/10.1016/j.chemgeo.2021.120681

Digital Object Identifier (DOI):
10.1016/j.chemgeo.2021.120681

Link:
Link to publication record in Edinburgh Research Explorer

Document Version:
Peer reviewed version

Published In:
Chemical Geology

Chemical Geology

Geochemistry of serpentinized and multiphase altered Atlantis Massif peridotites (IODP Expedition 357): Petrogenesis and discrimination of melt-rock vs. fluid-rock processes

--Manuscript Draft--

Manuscript Number:	CHEMGE14168R2
Article Type:	Research paper
Keywords:	IODP Expedition 357; Atlantis Massif; oceanic core complex; mantle peridotite; fluid-rock interaction; melt-rock interaction
Corresponding Author:	Scott Andrew Whattam, Ph.D. King Fahd University of Petroleum & Minerals Dhahran, Eastern Province SAUDI ARABIA
First Author:	Scott Andrew Whattam, Ph.D.
Order of Authors:	Scott Andrew Whattam, Ph.D.
	Gretchen L. Früh-Green, PhD
	Mathilde Cannat
	Jan C. M. De Hoog
	Stéphane Rouméjon, PhD
	Norikatsu Akizawa
	Chiara Boschi
	Michelle Harris
	Kirsten Wenzel
	Javier Escartin
	Barbara E. John
	Mathew I. Leybourne
	Esther M. Schwarzenbach
	Andrew McCaig
	Dominique Weiss
	Morgan Williams
	Laura Bilenker
Abstract:	International Ocean Discovery Program (IODP) Expedition 357 drilled 17 shallow sites distributed ~ 10 km in the spreading direction (from west to east) across the Atlantis Massif oceanic core complex (Mid-Atlantic Ridge, 30 ºN). Mantle exposed in the footwall of the Atlantis Massif oceanic core complex is predominantly nearly wholly serpentinized harzburgite with subordinate dunite. Altered peridotites are subdivided into three types: (I) serpentinites, (II) melt-impregnated serpentinites, and (III) metasomatic serpentinites. Type I serpentinites show no evidence of melt-impregnation or metasomatism apart from serpentinization and local oxidation. Type II serpentinites have been intruded by gabbroic melts and are distinguishable in some cases on the basis of macroscopic and microscopic observations, e.g., mm-cm scale mafic-melt veinlets, rare plagioclase (‹0.5 modal % in one sample) or by the local presence of secondary (replacive) olivine after orthopyroxene; in other cases, 'cryptic' melt-impregnation is inferred on the basis of incompatible element enrichments. Type III serpentinites are characterized by silica metasomatism manifested by alteration of orthopyroxene to talc and amphibole, and by anomalously high anhydrous SiO_2 concentrations (59-61 wt.%) and low MgO/SiO_2 values (0.48-0.52). Although many chondrite-normalized rare earth element (REE) and primitive mantle-normalized incompatible trace element anomalies, e.g., negative Ce-anomalies, are attributable to serpentinization, other compositional heterogeneities are due to melt-impregnation. On

	the basis of whole rock incompatible trace elements, a dominant mechanism of melt-impregnation is distinguished in the central and eastern serpentinites from fluid-rock alteration (mostly serpentinization) in the western serpentinites, with increasing melt-impregnation manifest as a west to east increase in enrichment in high-field strength elements and light REE. High degrees of melt extraction are evident in low whole-rock Al_2O_3/SiO_2 values and low concentrations of Al_2O_3, CaO and incompatible elements. Estimates of the degree of melt extraction based on whole rock REE patterns suggest a maximum of ~ 20 % non-modal fractional melting, with little variation between sites. As some serpentinite samples are *ex situ* rubble, the magmatic histories observed at each site are consistent with a local source (from the fault zone) rather than rafted rubble that would be expected to show more heterogeneity and no spatial pattern. In this case, the studied sites may provide a record of enhanced melt-rock interactions with time, consistent with proposed geological models. Alternatively, sites may signify heterogeneities in these processes at spatial scales of a few km.

06-Dec-2021

Dear Editor Johannesson,

On behalf of my coauthors and myself, we would like you to thank you for the editorial handling of the second revision of our *Chemical Geology* manuscript *Geochemistry of serpentinized and multiphase altered Atlantis Massif peridotites (IODP Expedition 357): Petrogenesis and discrimination of melt-rock vs. fluid-rock processes*. We did our best to address the concerns of both reviewers.

Sincerely,

Scott A. Whattam

29-Nov-2021

Dear Editor Johannesson,

On behalf of my coauthors and myself, we would like you to thank you for the editorial handling of the revision of our *Chemical Geology* manuscript *Geochemistry of serpentinized and multiphase altered Atlantis Massif peridotites (IODP Expedition 357): Petrogenesis and discrimination of melt-rock vs. fluid-rock processes*. There was however a problem in that, for whatever reason, Reviewer 5 provided a review of the *original* manuscript, which we were not able to detect until we were about halfway addressing his/her comments, which made the responses process challenging. Nevertheless, we did our best to address the concerns of both reviewers. Please find below in blue text our responses to the comments of Reviewers 3 and 5. Where we cite particular Lines where specific changes have been made, this is in reference to the 'clean' version of the manuscript.

Sincerely,

Scott A. Whattam

Dear Dr. Whattam,

I can now inform you that the reviewers and editor have evaluated the manuscript "Geochemistry of serpentinized and multiphase altered Atlantis Massif peridotites (IODP Expedition 357): Petrogenesis and discrimination of melt-rock vs. fluid-rock processes". As you will see from the comments below and on https://www.editorialmanager.com/chemge/, moderate revision has been requested.

Given that the requested revisions are moderate the revised version is required by 24 Nov 2021.

To submit a revision, go to https://www.editorialmanager.com/chemge/ and log in as an Author. You will find your submission record under Submission(s) Needing Revision.

When resubmitting, please present any figures, tables, etc. as separate files. See the Artwork Guidelines on the home page right menu for file naming conventions, referencing and format issues.

I hope that you will find the comments to be of use to you, and I am looking forward with interest to receiving your revision.

NOTE: Upon submitting your revised manuscript, please upload the source files for your article. We cannot accommodate PDF manuscript files for production purposes. We also ask that when submitting your revision, you follow the journal formatting guidelines. For additional details regarding acceptable file formats, please refer to the Guide for

Authors at: http://www.elsevier.com/journals/<slugified journal title>/<issn>/guide-for-authors

When submitting your revised paper, we ask that you include the following items:

Response to Reviewers (mandatory)

This should be a separate file labeled "Response to Reviewers" that carefully addresses, point-by-point, the issues raised in the comments appended below. You should also include a suitable rebuttal to any specific request for change that you have not made. State the line number of any revisions that are made.

Manuscript and Figure Source Files (mandatory)

We cannot accommodate PDF manuscript files for production purposes. We also ask that when submitting your revision you follow the journal formatting guidelines. Figures and tables may be embedded within the source file for the submission if they are of sufficient resolution for production. For any figure that cannot be embedded within the source file (such as *.PSD Photoshop files), the original figure needs to be uploaded separately. Refer to the Guide for Authors for additional information.
http://www.elsevier.com/journals/chemical-geology/0009-2541/guide-for-authors

Highlights (mandatory)

Highlights consist of a short collection of bullet points that convey the core findings of the article and should be submitted in a separate file in the online submission system. Please use 'Highlights' in the file name and include 3 to 5 bullet points (maximum 85 characters, including spaces, per bullet point). See the following website for more information
http://www.elsevier.com/highlights

Graphical Abstract (optional)

Graphical Abstracts should summarize the contents of the article in a concise, pictorial form designed to capture the attention of a wide readership online. Refer to the following website for more information: http://www.elsevier.com/graphicalabstracts

Data in Brief (optional):

We invite you to convert your supplementary data (or a part of it) into an additional journal publication in Data in Brief, a multi-disciplinary open access journal. Data in Brief articles are a fantastic way to describe supplementary data and associated metadata, or full raw datasets deposited in an external

repository, which are otherwise unnoticed. A Data in Brief article (which will be reviewed, formatted, indexed, and given a DOI) will make your data easier to find, reproduce, and cite.

You can submit to Data in Brief when you upload your revised manuscript. To do so, complete the template and follow the co-submission instructions found here: www.elsevier.com/dib-template. If your manuscript is accepted, your Data in Brief submission will automatically be transferred to Data in Brief for editorial review and publication.

Please note: an open access Article Publication Charge (APC) is payable by the author or research funder to cover the costs associated with publication in Data in Brief and ensure your data article is immediately and permanently free to access by all. For the current APC see: www.elsevier.com/journals/data-in-brief/2352-3409/open-access-journal

Please contact the Data in Brief editorial office at dib-me@elsevier.com or visit the Data in Brief homepage (www.journals.elsevier.com/data-in-brief/) if you have questions or need further information.

MethodsX (optional)

We invite you to submit a method article alongside your research article. This is an opportunity to get full credit for the time and money spent on developing research methods, and to increase the visibility and impact of your work. If your research article is accepted, we will contact you with instructions on the submission process for your method article to MethodsX. On receipt at MethodsX it will be editorially reviewed and, upon acceptance, published as a separate method article. Your articles will be linked on ScienceDirect. Please prepare your paper using the MethodsX Guide for Authors: https://www.elsevier.com/journals/methodsx/2215-0161/guide-for-authors(and template available here: https://www.elsevier.com/MethodsX-template) Open access fees apply.

Include interactive data visualizations in your publication and let your readers interact and engage more closely with your research. Follow the instructions here: https://www.elsevier.com/authors/author-services/data-visualization to find out about available data visualization options and how to include them with your article.

Kind regards,

Dhilip Kumar, on behalf of

Dr. Karen H. Johannesson
Editor
Chemical Geology

....

Important note: If a reviewer has provided a review or other materials as attachments, those items will not be included in this letter. Please log on to the journal site to determine whether attachments have been provided.

COMMENTS FROM EDITORS AND REVIEWERS

Decision – Moderate Revisions
Manuscript Number: CHEMGE14168_R1
Title: Geochemistry of serpentinized and multiphase altered Atlantis Massif peridotites (IODP Expedition 357): Petrogenesis and discrimination of melt-rock vs. fluid-rock processes
Authors: S. A. Whattam, G. L. Früh-Green, M. Cannat, J. C. M. De Hoog, S. Rouméjon, N. Akizawa, C. Boschi, M. Harriz, K. Wenzel, J. Escartin, B. E. John, M. I. Leybourne, E. M. Schwarzenbach, A. McCraig, D. Weiss, M. Williams, and L. Bilenker
Editor: Johannesson

I have now received the required reviews for your manuscript and am happy to report that they favorable of publication after some moderate revisions. Reviewer 3 reviewed the original manuscript and is now only some relatively minor comments and suggestions that require your attention. Reviewer 5, who did not review the original manuscript has some additional concerns. First, this reviewer recommend that you first model the low temperature reactions that may have influenced these rocks and then discuss the possible range of temperatures experienced by the protolith rocks. The reviewer also has some question about your terminology as for example the use of peridotite and so forth. Both reviewers commented on the Eu anomalies.

In making your revisions and returning your revised manuscript, please include a detailed description of how you addressed each reviewer's comments, concerns, and recommendations.

Reviewer #3: This is is the revised version of the manuscript by Whattam et al., on expedition 357 peridotites fro the Atlantis Massif. The authors have done a nice job addressing (and refutting) this reviewer's comments. I have generally minor comments on this version, at the discretion of the authors and the Associate Editor.

Figure 3 bottom panel: typo "metasomatic Peridotite".

Fixed. Thanks.

355: contents that range

Fixed. Thanks.

387: But this is already shown here, in figure 5. Sites 0072 and 0068 are higher than the other sites (obviously), so what else do you need to show in 6.2.3. I do not understand this sentence.

We are uncertain as to the confusion.

397: extreme fractionation. I think they show simply low La/Yb. Extreme with respect to what?

We removed "but extreme LREE/HREE fractionation".

390-403. While the Ce-anomalies are discussed later, here in the result description they should be pointed out.

We appended the first sentence of Section. 5.2. so it now reads: *Significant differences in the relative degree of depletion, pattern morphology, and the existence of prominent element anomalies, e.g., conspicuous positive or negative Ce-anomalies depending on serpentinite type, are apparent on the basis of chondrite-normalized REE and PM-normalized incompatible trace element patterns (Fig. 5).*

406-412: As I said in my original comments, I disagree with the structure of alteration / metasomatism first and then depletion discussion. In terms of evolution, the rocks experienced depletion first, upon which the other processes were imposed, so that makes more sense to me. Obviously the authors see it differently, and I guess the paper structure is in the eye of the beholder.

Yes, it does appear more logical to discuss as the reviewer states above. However, and as mentioned in our responses to the first set of comments, it is necessary to provide discussion on melt-infiltration and metasomatism first, in preceding sections, as the modelling is based on taking these processes into account.

436: Just as a comment: being in a MOR setting plagioclase fractionation is important. The variable Eu anomalies in the REE patterns imply that the impregnating melts may have seen variable Plagioclase fractionation, which, in turn, can make the Sr interpretation as melt proxy quite complicated. In other words, there may be Sr addition by melt impregnation, but it might hard to interpret as such.

OK, and we now make mention of the original comment of this reviewer on Eu anomalies which was: *Melt addition results in plagioclase accumulation, which can generate a positive Eu anomaly. How do you envision a negative Eu anomaly from Plagioclase removal? Was plagioclase added and then removed (how)? And if true, why would this lead to Eu depletions, when the addition of Plagioclase results in Eu addition? This interpretation here appears too simplistic, and frankly irrelevant to the rest of the paper.*

Because of this comment, we removed any mention of the Eu-anomalies in the first revised manuscript.

439: when you say "peridotite" do you mean in general, or from this study?
We do not mention peridotite in Line 439 so we are uncertain as to where in the text the reviewer is referring.

502-505. I would clarify here that when you say "fluid-dominated peridotites ", or "melt-dominated peridotites" you mean those interpreted by Paulick as such. Paulick's interpretation was based on the then available data and specific sampling. It does not mean that their interpretations for "fluid-" or "melt-" dominated peridotite encompass the global variance. Your data alone in the eastern sites proves that. In my opinion, the patterns are more important than the absolute concentrations, and that the Paulick study pointes at patterns. So I would add a sentence or two to clarify that, what you are doing here is comparing patterns, while the absolute concentrations are subject to other processes (for example amount of melt addition? Olivine dissolution?….).

The first sentence has been changed so it now reads: *Figure 8a highlights trace element variations of mean global abyssal peridotites with compositions dominated by melt-rock interaction vs. those dominated by fluid-rock interaction associated with serpentinization (as interpreted by Paulick et al., 2006).* After this sentence, we have added*: We note that (in Fig. 8) we are comparing patterns, as absolute concentrations subject to additional processes (e.g., melt addition).*

516: "equal" is obviously a poor word choice (different elements, different concentrations). I would say melt- rock reaction mobilizes both REE and HFSE compared to fluid dominated reactions which would likely preferentially mobilize REE, resulting in distinctly different patterns.

We have changed Line 516 so it now reads: *Though melt- rock reaction mobilizes both LREE and HFSE, fluid dominated reactions preferentially mobilize LREE, resulting in distinctly different patterns (Niu, 2004).*

574-579 "The REE patterns in Figs. 5a-e show at least two distinct melts that have infiltrated the peridotites, an enriched (E) and a depleted type (D), …". I'm not sure how to derive the inference for E and D type melts from Figure 5. Yes, the Eastern site rocks are more REE enriched, and perhaps assigned a E-type endmember, but I can't see the D-endmember, particularly as the most depleted rocks are also influenced by fluids. More explanation is needed.

Enriched and depleted refer to the REE pattern of the infiltrating melt, not to the total amount of REE in the samples. The depleted endmember is similar to N-MORB (La/Sm <1; dominant in central site M0072 for example)), the enriched endmember is enriched in LREE (La/Sm >1; common in eastern site M0068)

Figure 10 is too busy. I do not see a % +D melt addition. I wonder if you can break it to 2 panels to demonstrated separate things. It is just hard too hard to read.

The +1% and +10% melt addition, subsequent to 20% non-modal fractional melting, are shown to the immediate left of the y-axis. This figure was particularly to difficult to draw due to it's complexity of various components indicating partial melting estimate and the aforementioned melt additions subsequent to partial melting. However, we are unsure of what splitting into 2 panels would accomplish as both of these parameters (partial melting estimate and melt addition subsequent to melting) would need at some point to be plotted simultaneously anyway, so we left the figure as is.

670 "were"

Fixed, thanks.

681-684. Perhaps the data also points to localized, or focused, melt transport. In that, the melts do not uniformly flow though the lithosphere but coalesce in zones of melt extraction.

Yes perhaps and I originally put this into the revised manuscript. However, a co-author asked that it be removed as she did not find that it helped in our interpretations.

Reviewer #5: Dear Editor,

The manuscript of Scott Whattam and co-author addresses the study of a set of meta-peridotites recovered during an important IODP expedition at the Atlantis Massif, in the region close to the site of the Lost City hydrothermal field.
The study focuses on a set of metamorphosed mantle rocks recording a number of fluid-dominated events superposed to mantle-derived protoliths that have previously experienced variable degrees of melt-rock interaction.
Based on major and trace element distribution and simple modelling of the melt-rock interactions the authors recognize a west-to-east trend of increasing melt impregnation apparently opposed to the degree of fluid-dominated rock interaction.
This work requires some implementation in order to clearly separate the observed processes and quantify their relative contributions. Major fluid-dominated relationships are not solved, while high-T magmatic relationships are too simplified and over interpreted.
While describing a long and complex set of fluid-dominated rock modifications (Si-metasomatism, serpentinization and carbonate veining) authors only model the protolith depletion and high-T melt-rock interaction that is the farther process recorded in these rocks severely masked by the subsequent low-T events. I would recommend modelling low-T interaction before and only after define a possible range for the protolith-related processes.

Some major points:
Terminology: carefully review rock definitions. Object of this study are the extremely metasomatized, serpentinized and weathered rocks derived from peridotitic protoliths. Bulk rock analyses do not refer to "peridotite" but to their metamorphic products. Better use terms like serpentinite, metasomatized serpentinite, or carbonate-veined serpentinite. The term "Ca-rich peridotite" should be avoided because it gives the image of a Ca-enriched mantle rock, which clearly is not the case. Restrict the use of the term "peridotite" to the discussion of the high-T protolith paragenesis or composition. Clearly separate protolith characters from the observed metamorphic products. In addition, caution should be taken on the use of "metasomatism"; it must clearly appear whether you refer to Si-metasomatism or to mantle-source metasomatism.

These are cogent points. We have now changed "peridotite" when referring to metamorphosed peridotite in all cases to serpentinite, hence our three types are now: Type I, serpentinites; Type II, melt-impregnated serpentinites; and Type III metasomatic serpenitinites. "Peridotite" is reserved for use when discussing protolith only. When "metasomatism" is used, we now indicate as to whether Si-metasomatism or mantle-source metasomatism.

Ca-rich carbonate veined serpentinites: these rocks bear a large amount of carbonates that affect the bulk composition (both dilution and addition of elements). They can be briefly discussed and cleaned out from the main discussion. Caution is required when discussing Sr behaviour. There are too many carbonates (aragonite) to ignore their effects on Sr distribution. Is there any correlation between Sr content and abundance of carbonate veining? If not why? Can this be a clue to the origin of fluids?

A correlation between Sr content and carbonate veining is evident and is noted, from Lines 414-422 of our original manuscript and in our revised manuscript, section 6.1. Evidence of fluid-dominated serpentinization processes: *Significant observations from the chondrite-normalized REE and PM-normalized patterns are: (1) prominent negative Ce-anomalies (i.e., Ce/Ce* where Ce* = √(LaCN*PrCN) and Ce = CeCN) in the western serpentinized peridotites and two serpentinized central peridotite, and positive Ce-anomalies in almost all eastern peridotites (the vast majority of other central peridotites show Ce/Ce* ~ 1); (2) extreme U-enrichment in many peridotites with values that range to nearly 300 x PM; and (3) extreme Sr-anomalies with enrichments of up 100 x PM in most Ca-rich serpentinized peridotites and depletion to below 0.1 x PM in the peridotites of Sites M0072 and M0068.* This also comprises our latest version submitted here.

Degree of melting vs. fluid-dominated processes: deriving a reliable degree of partial melting from bulk-rock data is a delicate exercise. A rigorous modelling can only be done based on relic mineral chemistry and a careful micropetrographic investigation; even in this case solving melt/rock interaction barely leads to an unambiguous result. The inferred degree of partial melting (19-21%) is high also considering that it has not been cleaned out by the serpentinization effects. The evaluation of the degree of impregnation based on La/Sm distribution is highly questionable given these elements are mobile during serpentinization and metasomatism. Not before showing the effects of low-T processes.

Partial melting estimates of such highly altered serpentinites on the basis of bulk rock chemistry is indeed a challenge. We note fundamentally however, that partial melting estimates have been made by the first author on the basis of Cr# of spinel (from Hellebrand et al., 2001, i.e., whereby F = 10ln(Cr#)+24)) for a completed manuscript that will be submitted subsequent to final decision on this manuscript, and are identical to the ones calculated on the basis of bulk chemistry for this manuscript. The partial melting estimates based on spinel Cr# are 11-19% but with the vast majority being 15-19%. Thus, our partial melting estimates based on whole rock content are robust, as the inferred degree of partial melting of 19-21% on the basis of whole rock chemistry represent *maximum* degrees as stated in the abstract. Moreover, we stress that apart from heavily altered opx (to bastite) the samples are mostly barren of relict minerals.

Based on your description, the observed patterns result from four processes: partial melting, melt/rock interaction, silica metasomatism and serpentinization (leaving apart carbonate veining that I suggest to exclude from the modelling).
I hence recommend duplicating the exercise of modelling the trace element patterns for the serpentinization and Si-metasomatic processes. Then authors may derive some relative approximations of the degree of partial melting and eventually melt/rock reactions.

We already have taken into account the serpentinization and Si-metasomatic processes already as the SE endmember in Fig. 10 is probably fluid (technically, it could be a very low-degree melt but we don't see melt with such high La/Sm anywhere). What SE actually is has been purposely left vague but it has very low HREE, so it won't affect the melt modelling much. We only see in very depleted samples because REE are so low. In more REE-rich samples, E and D components are much more significant, so the effect of serpenitization is negligible.

Melt/rock reactions: make clear which kind of melt/rock reaction you are describing in your model. Plagioclase crystallization is not a closed system melt addition but requires defining the mineral reaction coefficients. Describe and the refertilization model in the text not only in the figure caption.

We are confused with this comment as we do not even mention plagioclase in our model. The model is essentially based on adding a metasomatic agent to a peridotite. The closest equivalent natural process would be melt infiltration (as veins) in the samples. But the result of modal melt metasomatism would be quite similar (melt-rock reaction). There will also be some fluid-rock reaction on top of this, but it's effect will be limited in terms of REE patterns (see previous comment). But in essence, we simply tried to model the processes we describe in the paper.

Effects of fluid-rock interactions: effects of serpentinization and Si-metasomatism are only qualitatively described.

There is no discussion and interpretation of the opposite Ce and Eu anomalies that appear as a clear feature in the trace element patterns. The presence of both anomalies with different polarities is intriguing and deserve a deeper analyses and discussion.

With respect to Ce-anomalies, this is addressed in the manuscript (see our comment above that pertains to the relation between Sr content and volume/density of carbonate veining). Furthermore, in the original manuscript, we go on to discuss the origin of the Ce-anomalies in details in Lines 423-435 where we state: *With respect to the negative Ce-anomalies exhibited mostly by the western serpentinized peridotites (site M0071), such anomalies in peridotites have been attributed to seawater-peridotite interaction (e.g., Frisby et al., 2016a, b) and indeed, (oxygenated) seawater itself exhibits a negative Ce-anomaly (e.g., Elderfield and Greaves, 1982). The western site serpentinized peridotites range to the highest U concentrations (5.05 µg/g), whereas the melt-impregnated peridotites of central site M0072 and eastern site M0068 range to the lowest U concentrations (0.01 µg/g) (Fig. 6a, Table 3), which suggests that U enrichment is associated with serpentinization and oxidation, and not melt-impregnation. U enrichment in serpentinites is common as U is hosted by serpentine phases (e.g., Deschamps et al., 2010). Frisby et al. (2016a, b) have shown that U enrichments correlate with Ce anomalies and the amount of Nd derived from seawater, which is a proxy for water/rock ratios. Thus, U enrichments have been shown explicitly to reflect fluid-rock interaction in abyssal peridotites.*

With respect to the Eu-anomalies, we did address these in the original version of this manuscript but these were subsequently removed in the current version due to the comments of Reviewer 3 who stated:

452. Melt addition results in plagioclase accumulation, which can generate a positive Eu anomaly. How do you envision a negative Eu anomaly from Plagioclase removal? Was plagioclase added and then removed (how)? And if true, why would this lead to Eu depletions, when the addition of Plagioclase results in Eu addition? This interpretation here appears too simplistic, and frankly irrelevant to the rest of the paper.

So, we do not address Eu-anomalies in our revised manuscript.

Refertilizing melts: it appears from your model that compositionally different melts reacted with the peridotite protolith. Plot the inferred REE patterns in the model figure (Fig. 10a) and compare to the regional basalt compositions to check they have reasonable compositional characters. This will in turn justify your assumption of being the reacting melt "mafic" in composition as the melts playing around gabbroic complexes can be extremely variable in composition (see the large biblio on both Atlantis Massif and Atlantis Bank melts and veining).

We don’t understand what the reviewer means by ‘regional basalt compositions’. At any rate, we know that the reacting melts are mafic as the first author has whole-rock chemistry for many impregnates (as does Fruh-Green as presented in Lithos, 2018) which confirms this (that they are basalt) and that there is little variability between different impregnates from different sites. We now indicate this (that we know that they are mafic based on whole rock chemistry for another manuscript in preparation by the first author and as presented by Fruh-Green et al., 2018) in the revised version of this manuscript.

Grouping and averaging: looking to the means reported in figure 6A and discussed in paragraph 6.1 seems to me that the average mixes different kind of rocks: samples from M0072 are similar to samples from M0068, and different from the other central sites as you correctly discuss later. This suggests a higher variability than that corresponding to the averaged regions. M0072 alone drags your mean to higher values; taking this out in fig 6b the pattern would be comparable to that of the western sites.
Moreover, each site presents a large variation from "depleted" to "enriched" patterns. I would recommend anticipating the pattern modelling in order to understand better which the meaning of averaging these patterns is. Disentangling Si-metasomatism from serpentinization and refertilization in the trace element is a prerequisite to averaging.

Please see our initial ‘Dear Editor’ paragraph where we note that it became obvious to us that this reviewer is referring to the original manuscript; we did not originally understand the above comment as both Fig. 6 and paragraph 6.1 in the revised version, deals with absolute abundances, not averages. However, now realizing this, with respect to the original ms version, a similar comment was made by Reviewer 3 regarding the averaging of central holes, which we agreed with and because of this we subsequently parsed the original Fig. 6b (now Fig. 8) into three plots with each one representing discrete holes. Our Fig. 8 means now are representative of the range of compositions of each site, and hence the average represents a bulk average of the composition of each site. Figure 8 now clearly shows that the dominant process changes from fluid-dominated in the west to melt-dominated in the east.

Reference values: Paragraph 6.3.2 reports a long intro dedicated to the alpine lherzolite massifs. However, lherzolite massifs and abyssal peridotites are not directly comparable domains. A number of studies refer to refertilization, impregnation and melt retention in MOR domains from both bulk and mineral chemistry. Please reduce this paragraph and refer to the abyssal peridotite realm from both bulk and mineral chemistry points of view.

The domains are not identical but the processes are. Nevertheless, in order to ‘considerably shorten’ the text of our revised manuscript 2, as suggested by Reviewer 3, this paragraph was removed from revision 2 and is not included here.

Line 564: "olivine mantling Opx": this is evidence for incongruent partial melting at the best, not of melt impregnation. You should track spinel or plagioclase lineations, interstitial cpx, cpx-amph-sp blebs in opx... see the various works of Seyler and coworkers.

We don’t understand why the reviewer is insisting on these being two independent processes: Melt-impregnation resulted in incongruent partial melting of pre-existing opx and crystallization of (replacive) olivine. With respect to the aforementioned phases listed by the reviewer, as reported in the manuscript, there is rare plagioclase (two grains) in one sample only, and no cpx (these are *highly serpenitinzed* harzburgites and rare dunites). As we report in Table 2 (mode) spinel is commonly embedded in opx, particularly in the Type I serpentinized peridotites but not in the melt-impregnated ones.

Line 751-752: "… a broad correlation of La/Sm vs Yb can be observed…". There is absolutely NO correlation between these two parameters visible in figure 10b. The following considerations are hence not supported by your data.

There is no mention of a broad correlation of La/Sm vs. Yb in the second version of our manuscript.

Line 306: "…dunites … that exhibit Al2O3/SiO2 < 0.01 indicative of significantly higher degrees of melt extraction." Dunites are not the product of melt extraction strictu sensu... rephrase these two sentences

This had already been fixed in the second revision whereby Lines 309-314 reads: *In general, the Atlantis Massif harzburgites record Al2O3/SiO2 that range from ~ 0.01-0.04 indicating moderate to high degrees of magmatic depletion. Two Type I serpentinized dunites from the central sites (M0076B-3R1-78-82, M0076B-5R1-59-61, Table 1), and one dunite (1309D-31R-25-28) from Site U1309 reported by Godard et al. (2009) exhibit Al2O3/SiO2 < 0.01. Very low Al2O3/SiO2 ratios can alternatively be caused by replacive melt-rock interaction.*

Normalizing values: please report in the text which CI and PM values you normalize to.

These are indicated in the figure captions for all figures which use CI, PM or other values that are data our normalized to. In past manuscripts when I have cited in the text, I usually get requests from reviewers to remove and cite in figures only. We tend to agree with this as there is no need for extraneous text when this information can be found in the figure caption, so we leave this as is.

Graphical Abstract

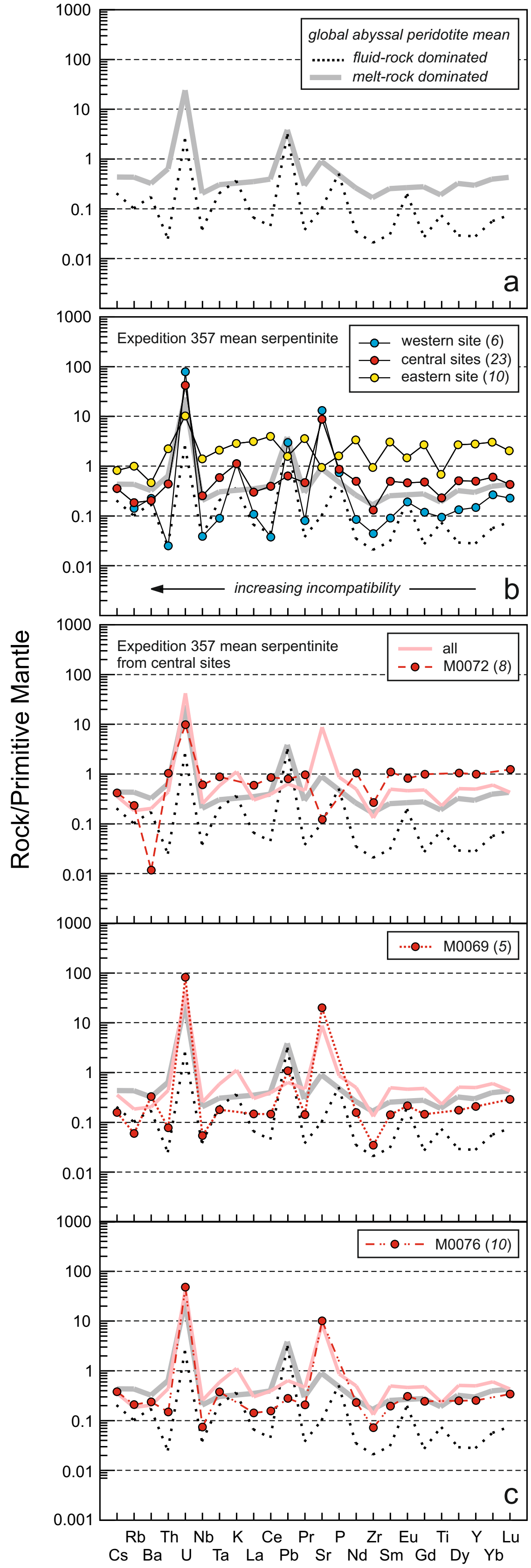

Graphical Abstract Whattam et al. (2021)

- Mantle exposed in the footwall of the Atlantis Massif OCC is predominantly nearly wholly serpentinized harzburgite
- Altered peridotites comprise three types: (I) serpentinites, (II) melt-impregnated serpentinites, and (III) silica metasomatized serpentinites
- A dominant mechanism of melt-impregnation is distinguished in the central and eastern serpentinites from fluid-rock alteration (mostly serpentinization) in the western serpentinites
- Increasing melt-impregnation is manifest as a west to east increase in enrichment in HFSE and LREE
- Estimates of the degree of melt extraction suggest a maximum of ~ 20 % non-modal fractional melting, with little variation between sites

Revised manuscript with changes marked

Geochemistry of serpentinized and multiphase altered Atlantis Massif peridotites (IODP Expedition 357): Petrogenesis and discrimination of melt-rock vs. fluid-rock processes

Scott A. Whattam[a*], Gretchen L. Früh-Green[b], Mathilde Cannat[c], Jan C. M. De Hoog[d], Esther M. Schwarzenbach[e], Javier Escartin[f], Barbara E. John[g], Mathew I. Leybourne[h], Morgan J. Williams[i], Stéphane Rouméjon[b], Norikatsu Akizawa[j], Chiara Boschi[k], Michelle Harris[l], Kirsten Wenzel[m], Andrew McCaig[n], Dominique Weis[o], Laura Bilenker[p]

[a]*Department of Geosciences, King Fahd University of Petroleum and Minerals, Dhahran, 31261, Saudi Arabia*

[b]*Institute of Geochemistry and Petrology, ETH Zurich, Clausiusstrasse 25, 8092 Zürich, Switzerland*

[c]*Institut de Physique du Globe de Paris, CNRS, 1 rue Jussieu, 75238 Paris, Cedex 05, France*

[d]*School of Geosciences, Grant Institute, The University of Edinburgh, James Hutton Road, EH9 3FE, United Kingdom*

[e]*Institute of Geological Sciences, Freie Universität Berlin, Malteserstrasse 74-100, 12249 Berlin, Germany*

[f]*Laboratoire de Géologie – CNRS, UMR 8538, École Normale Supérieure, PSL University, Paris, France*

[g]*Department of Geology and Geophysics, University of Wyoming, Laramie, WY 82071*

[h]*Queen's Facility for Isotope Research, Department of Geological Sciences and Geological Engineering, and Arthur B. McDonald Canadian Astroparticle Physics Research Institute, Department of Physics, Engineering Physics & Astronomy, Queen's University, Kingston, ON, Canada, K7L 3N6*

[i]*CSIRO Mineral Resources, 26 Dick Perry Avenue, Kensington WA 6151, Australia*

[j]*Kanazawa University, Department of Earth Sciences, Kakuma Kanazawa, Ishikawa 920-1192, Japan*

[k]*Institute of Geosciences and Earth Resources – CNR, Via Moruzzi 1, 56124 Pisa, Italy*

[l]*School of Geography, Earth and Environmental Sciences, 109 Fitzroy Building, Plymouth University, Plymouth PL4 8AA, United Kingdom.*

[m]*GeoZentrum Nordbayern, Friedrich-Alexander-University Erlangen-Nuremberg, Schlossgarten 5a, 91054 Erlangen, Germany*

[n]*School of Earth and Environment, Leeds University, Woodhouse, Leeds LS2 9JT, United Kingdom*

[o]*Pacific Centre for Isotopic and Geochemical Research, Earth, Ocean and Atmospheric Sciences, University of British Columbia, Earth, Ocean and Atmospheric Sciences, 2020-2207 Main Mall, Vancouver BC V6T-1Z4, Canada*
[p]*Deparment of Geosciences, Auburn University, Auburn, AL 36849*

*Corresponding author: Scott A. Whattam
E-mail address: sawhatta@gmail.com

Abstract

International Ocean Discovery Program (IODP) Expedition 357 drilled 17 shallow sites distributed ~ 10 km in the spreading direction (from west to east) across the Atlantis Massif oceanic core complex (Mid-Atlantic Ridge, 30 °N). Mantle exposed in the footwall of the Atlantis Massif oceanic core complex is predominantly nearly wholly serpentinized harzburgite with subordinate dunite. Altered peridotites are subdivided into three types: (I) serpentinites, (II) melt-impregnated serpentinites, and (III) metasomatic serpentinites. Type I serpentinites show no evidence of melt-impregnation or metasomatism apart from serpentinization and local oxidation. Type II serpentinites have been intruded by gabbroic melts and are distinguishable in some cases on the basis of macroscopic and microscopic observations, e.g., mm-cm scale mafic-melt veinlets, rare plagioclase (<0.5 modal % in one sample) or by the local presence of secondary (replacive) olivine after orthopyroxene; in other cases, 'cryptic' melt-impregnation is inferred on the basis of incompatible element enrichments. Type III serpentinites are characterized by silica metasomatism manifested by alteration of orthopyroxene to talc and amphibole, and by anomalously high anhydrous SiO_2 concentrations (59-61 wt.%) and low MgO/SiO_2 values (0.48-0.52). Although many chondrite-normalized rare earth element (REE) and primitive mantle-normalized incompatible trace element anomalies, e.g., negative Ce-anomalies, are attributable to serpentinization, other compositional heterogeneities are due to melt-impregnation. On the basis of whole rock incompatible trace elements, a dominant mechanism of melt-impregnation is distinguished in the central and eastern serpentinites from fluid-rock alteration (mostly serpentinization) in the western serpentinites, with increasing melt-impregnation manifest as a west to east increase in enrichment in high-field strength elements and light REE. High degrees of melt extraction are evident in low whole-rock Al_2O_3/SiO_2 values and low concentrations of Al_2O_3, CaO and incompatible elements. Estimates of the degree of melt extraction based on whole rock REE patterns suggest a maximum of ~ 20 % non-modal fractional melting, with little variation between sites. As some serpentinite samples are *ex situ* rubble, the magmatic histories observed at each site are consistent with a local source (from the fault zone) rather than rafted rubble that would be expected to show more heterogeneity and no spatial pattern. In this case, the studied sites may provide a record of enhanced melt-rock interactions with time, consistent with proposed geological models. Alternatively, sites may signify heterogeneities in these processes at spatial scales of a few km.

Keywords: IODP Expedition 357; Atlantis Massif; mantle peridotite; fluid-rock interaction; melt-rock interaction

1. Introduction

Spreading rate exerts a profound influence on the geometry and architecture of the oceanic crust. Slow-spreading ridges (≤ 5 cm/year), as exemplified by the Mid-Atlantic ridge (MAR), are characterized by wide (up to 30 km) and deep (1–2 km) axial valleys bounded by uplifted shoulders and transient magma reserves. In contrast, fast-spreading ridges (≥ 9 cm/year), as characterized by the East Pacific Rise, exhibit much narrower to absent axial troughs (a few hundred meters wide) and a more continuous magma supply (e.g., Macdonald, 1982; Karson, 2002; Stewart et al., 2005). Analogous with 'metamorphic core complexes' found in extended continental regions (e.g., John, 1987), 'oceanic core complexes' (OCCs), such as the Atlantis Massif (30 °N, Fig. 1a) along the MAR, represent segments of a slow spreading ridge comprised of elevated seafloor massifs that display flat or gently curved upper surfaces with prominent corrugations or 'megamullions' (Escartin et al., 2017; Tucholke et al., 1998). OCCs comprise segments of lower crustal and upper mantle rocks exposed at the seafloor (Cann et al., 1997; Blackman et al., 1998; Tucholke et al., 1998) and represent uplifted footwalls of large-offset low-angle normal faults, commonly referred to as detachment faults. Mantle rocks of OCCs characteristically comprise olivine-rich peridotite (i.e., harzburgite, dunite) that interacted with seawater to produce serpentinite over a range of temperatures (Andreani et al., 2007; Blackman et al., 1998; Boschi et al., 2006a; Boschi et al., 2006b; Cann et al., 1997; Cannat, 1993; Früh-Green et al., 2004; Karson et al., 2006; Kelemen et al., 2007; Rouméjon et al., 2015; Rouméjon et al., 2018a; Schroeder et al, 2002).

Four OCCs have been drilled by the Ocean Drilling Program (ODP), the Integrated Ocean Drilling Program (IODP) and the International Ocean Discovery Program (IODP). The Atlantis Massif is one of the best studied and well-known OCC as it hosts the off-axis, peridotite-hosted Lost City hydrothermal field (Kelley et al., 2001) on its southern wall (Fig. 1b). Other drilled OCCs include the Atlantis Bank, SW Indian Ridge (ODP Hole 735B, Dick et al., 2000), the MARK (Mid-Atlantic Ridge Kane fracture zone) at 23°32′ N (ODP Leg 153, Sites 921–924, Cannat et al., 1995), and an OCC on the MAR at 15°44′ N (ODP Leg 209, Site 1275, Kelemen et al., 2004). The Atlantis Massif (30 °N, Fig. 1a) was drilled during IODP Expeditions 304/305 (Blackman et al., 2006), at Site U1309 and Expedition 357 (Früh-Green et al., 2017, 2018; Roumejon et al., 2018a, 2018b; Akizawa et al., 2020).

Research on detachment faulting at OCCs implies that oceanic spreading is closely linked to the development of hydrothermal circulation patterns and encompasses a wide variety of fluid flow and hydrothermal regimes (McCaig et al., 2007; Escartin et al., 2008). High-temperature fluid circulation both within the footwall and along the fault zone is well documented on the basis of mineralogy and geochemistry (Schroeder and John, 2004; Boschi et al., 2006a; McCaig et al., 2010, Picazo et al., 2012, Verlaguet et al., 2021). Importantly, uplift along detachment faults appears to promote circulation and alteration within the footwall. Several studies propose a temporal evolution in the style of hydrothermal circulation associated with OCC formation. High-temperature systems are hosted in the basaltic hanging wall within the rift valley, whereas high-temperature ultramafic-hosted systems occur within the OCC footwall. Ultimately, hydrothermal circulation transitions to off-axis ultramafic-hosted systems within the footwall (Andreani et al., 2007; McCaig et al., 2007; Fouquet et al., 2010). In ultramafic and mafic systems, metasomatic assemblages of talc-tremolite-chlorite or quartz form at > 350 °C (Boschi et al., 2006a, 2008; McCaig et al., 2010; Verlaguet et al., 2021), typical of black smoker discharge zones, whereas serpentine-prehnite-hydrogarnet assemblages form at lower temperatures (Frost et al., 2008; Bach and Klein, 2009).

Cores recovered during IODP Expedition 357 have highly heterogeneous rock types, and are variably altered and deformed. Ultramafic rocks are dominated by serpentinized harzburgite with intervals of serpentinized dunite and minor pyroxenite veins; gabbroic layers occur as melt impregnations and veins. Dolerite dikes and basalts are the latest phase of magmatism. Overall, the peridotites show a high degree of serpentinization (> 80 %) and are locally oxidized. In cores with gabbroic intrusions, hydrothermal alteration of mixed peridotite and gabbroic lithologies forms serpentine-talc-amphibole-chlorite assemblages (Boschi et al., 2006b; Picazo et al., 2012).

The petrogenesis of mantle-derived peridotites recovered during IODP Expedition 357 is the subject of this communication. In this paper we use whole rock major, trace and rare earth element (REE) chemistry of Expedition 357 peridotites to discriminate dominant melt-impregnation vs. fluid-dominated processes (i.e., serpentinization, Si metasomatism) and constrain the degrees of partial melting recorded in the peridotites. The altered peridotites are subdivided into Type I serpentinites, Type II melt-impregnated serpentinites and Type III metasomatic serpentinites. Type I serpentinites show no evidence of melt-impregnation or metasomatism apart from serpentinization and local oxidation. Type II serpentinites are distinguishable in some cases on the basis of macroscopic or microscopic evidence and in other cases, are inferred on the basis of incompatible element enrichment in the case of ‘cryptically’ melt-impregnated serpentinites. Type III serpentinites are characterized by silica metasomatism and the formation of talc-rich alteration assemblages and anomalously high anhydrous SiO_2 concentrations and low MgO/SiO_2 values. In so doing, we geochemically characterize the evolution of mantle lithosphere at a slow-spreading ridge associated with OCC formation, and document spatial compositional variations.

2. Geological setting

The dome-shaped Atlantis Massif OCC is located at 30 °N on the western edge of the MAR axial valley where it intersects the Atlantis Fracture Zone (Fig. 1b). The OCC stretches 15-20 km N–S parallel to the ridge and is 8-12 km wide. Exhumation occurred via low-angle detachment faulting (Cann et al., 1997; Blackman et al., 2002; Schroeder and John, 2004; Karson et al., 2006; Ildefonse et al., 2007). On the basis of its distance from the spreading axis and a calculated spreading half-rate of 12 mm/yr (Zervas et al., 1995), the lithosphere of the massif is considered to be 2.0 to 0.5 Ma (Blackman et al., 2006), a span which encompasses eighteen SHRIMP U/Pb zircon ages of oxide gabbro and felsic dike melt intrusions recovered from Hole U1309D, which range from 1.28 ± 0.05 to 1.08 ± 0.07 Ma (Grimes et al., 2008). Dredging and submersible dives at the massif revealed the dominance of serpentinized peridotite (Blackman et al., 2002; Boschi et al., 2006a; Karson et al., 2006) concentrated primarily along the southern and most elevated portion of the detachment. Samples recovered during IODP Expeditions 304/305, with a drill hole reaching ~ 1500 m depth, consisted almost entirely of olivine-rich mafic intrusive rocks of gabbro and troctolite (Drouin et al., 2009; Ferrando et al., 2018; Godard et al., 2009; Suhr et al., 2008). These geological observations suggest a compositional change of the footwall, with peridotites decreasing in abundance from the segment end towards the north, and also reflecting variations in time of the emplacement of magma in the footwall (Ildefonse et al., 2007).

IODP Expedition 357 cored seventeen shallow holes at nine sites (Fig. 1b) along the detachment fault surface of the Atlantis Massif (Früh-Green et al., 2016). The two eastern sites (M0075, M0068) and one western site (M0071) recovered fault scarp deposits whereas the central sites yielded *in situ* sequences. Most of the sites are aligned along the southern edge of the detachment fault by the Atlantis Fracture Zone wall, with the northernmost hole (M0074) located ~ 6 km north of the detachment's southern edge, and ~ 1 km to the southwest of U1309D. In terms of igneous lithologies and their metamorphosed equivalents, IODP Expedition 357 recovered primarily serpentinized peridotite comprising harzburgite with subordinate dunite (Fig. 1c) and wehrlite with lesser amounts of variably altered mafic inclusions of basalt, gabbro and dolerite (Früh-Green et al., 2018; Rouméjon et al., 2018a; Akizawa et al., 2020). Core lengths range from approximately 1.3 to 16.5 m. Recovery was ~ 75 %.

3. Samples and petrography

Except for one talc schist, the protolith of which was mafic, all rocks chosen for study are serpentinized peridotites, and from holes immediately adjacent to the transform fault scarp and drilled at the southern edge of the detachment fault surface (Figs. 1b, c). All peridotites were subjected to high degrees of serpentinization on the order of > 80 %. On the basis of collective macroscopic, microscopic and whole rock chemistry evidence, the studied samples are divided into three types: Type I are serpentinites, Type II are melt-impregnated serpentinites, and Type III are metasomatic serpentinites. Type I serpentinites are ones primarily subjected to serpentinization only, and Types II and III serpentinites have been subjected to mm- to cm-scale mafic melt intrusions and subsequent silica metasomatism, respectively. In the case of melt-impregnation, this is evident in Type II serpentinites by the presence of small veinlets of dolerite (as reported in Expedition 357 petrology logs), and in one case by the presence of rare plagioclase and in another case, by the presence of recrystallized olivine along the peripheries of partially dissolved orthopyroxene (see Fig. 2). Further details regarding evidence for classification of Types II and III are provided in Table 1.

All samples were studied by polarization microscopy. Representative thin section images are given in Figure 2. Sample numbers are taken directly from Früh-Green et al. (2017, Supplementary material). Below, we describe the petrography of each sample type. The mineralogy and mode of the serpentinites are summarized in Table 2.

3.1. Type I serpentinites

Type I serpentinites (Fig. 2a-d) consist of dominant harzburgite (14 of 20 samples) and lesser dunite. Outlines of olivine are generally clear under plane-polarized light (PPL) as serpentinization is most intense around grain boundaries and fractures cutting olivine (e.g., Fig. 2a). Classic mesh-textures are commonly observed. In the harzburgite, orthopyroxene is always altered to bastite, but is nonetheless recognizable under crossed polars by remnant and deformed (curved) cleavage and parallel extinction. Orthopyroxene is typically < 2 mm and olivine is 2-4 mm. Reddish-orange to brown spinel is easily identifiable under PPL and is typically less than 0.5 mm but in some cases up to 4 mm. Spinel occurs both as isolated, angular grains and as subangular and rounded grains commonly arranged in masses or trails of multiple grains. Clinopyroxene was not observed in any samples, reflecting the high degrees of partial melting and melt extraction that many of these peridotites have undergone (see Fig. 3). Modal percentages of the volumetrically dominant harzburgite lie in the range of 75-90 % for olivine and 10-25 % for orthopyroxene; spinel ranges from 0-3 % (Table 2). In the dunite, orthopyroxene is absent and spinel is less common (0 to <1 %) than in the harzburgite.

Four Type I serpentinites exhibit anomalously high CaO contents ranging from 6-13 wt.% (see Table 3). Microscopic inspection reveals that the Ca-rich peridotites exhibit an extensive and densely concentrated, anastomosing network of ~ 0.1 mm thick carbonate veinlets (Fig. 2d).

3.2. Type II Melt-impregnated serpentinites

Melt-impregnated serpentinites consist of harzburgite only and comprise six of the 29 studied samples (Table 1). Type II serpentinites in most cases are observed to have mm to cm-scale mafic veins at the scale of drill core (Table 2) although these are not obvious in thin section. Orthopyroxene ranges from ~ 1-5 mm. Modal percentages of olivine and orthopyroxene are 70-90 % and 10-30 %, respectively, with spinel typically absent but reaching 2-3 % in one sample (Table 2).

In some Type II serpentinites, other petrographic evidence is present to confirm melt-impregnation. For example, one central harzburgite (76B-7R1-81-83) is the only one in which rare 0.5-0.7 mm plagioclase (< 0.5 % of the mode) is present (Fig. 2e). Plagioclase is highly altered (epidote, sericite) but preserves relict twinning. In another harzburgite from eastern Site M0068B, fresh, 0.5-1 mm olivine constitutes ~ 5 % of the mode, and is observed mantling orthopyroxene (Fig. 2f), which we interpret as replacive following dissolution of orthopyroxene accompanying melt injection.

3.3. Type III Metasomatic serpentinites

Type III serpentinites from this study include two harzburgites that are restricted to the eastern sites (Fig. 1c), and are distinguishable on the basis of talc-amphibole alteration of orthopyroxene (Fig. 2e) and whole rock chemistry (see Section 5.1). Orthopyroxene ranges from 1-6 mm. Brown spinel ranges from 0.5-2 mm and are always embedded in orthopyroxene. Modal percentages of olivine and orthopyroxene are ~ 70 % and 30 % respectively, with spinel occupying around 2 % (Table 2).

4. Analytical methods and data compilation

4.1. Whole rock geochemistry

Major and trace element contents of the serpentinites were determined by inductively coupled plasma mass spectrometry (ICP-MS) and atomic emission spectroscopy (ICP-AES) at ALS Geochemistry, North Vancouver, Canada. Prior to shipping to ALS, samples for whole-rock analysis were trimmed to remove weathered surfaces. Samples sent to ALS were crushed to > 70 % passing through a 2 mm mesh, and a 250-g split was pulverized to > 85 % of the material being < 75 µm in diameter. Powders were then analyzed for whole rock major and trace element determinations. For major element oxides, 100 mg of powered sample was added to lithium metaborate/lithium tetraborate flux, mixed well and fused in a furnace at 1000 °C. The resulting melt was dissolved in 100 mL of 4 % HNO_3/2 % HCl. This solution was then analyzed by ICP-AES (ALS Geochemistry method ME-ICP06) and the results were corrected for spectral inter-element interferences. Major element detection limits are 0.01% for all oxides except Cr_2O_3, which is 0.002 % (Supplementary Table S1). For loss on ignition (LOI), 1 g of sample powder was heated at 1000° C for one hour, cooled and then reweighed, with percent LOI calculated by the difference in weight.

For trace and rare earth elements, the ME-MS61L Super Trace and MS61L-REE methods (https://www.alsglobal.com/) were employed, which combines a four-acid digestion with ICP-MS instrumentation utilizing collision/reaction cell technologies to provide the lowest detection limits available. In the first method, analyzed elements include Ba, Cd, Ce, Co, Cr, Cs, Cu, Ga, Hf, La, Li, Mo, Nb, Ni, Pb, Rb, Sc, Sn, Sr, Ta, Te, Th, U, V, W, Zn and Zr; in the second method, analyzed elements include Dy, Er, Eu, Gd, Ho, Lu, Nd, Pr, Sm, Tb, Tm and Yb. This trace method has been optimized for long-term robust ICP-MS signal stability, in particular for samples with high Ca content. The prepared samples (nominal weight 0.25 g) were digested with 1.5 mL concentrated HNO_3

and $HClO_4$, followed by concentrated HF. Subsequently, the mixture was heated at 185 °C until incipient dryness, leached with 50 % HCl and diluted with weak HCl. The final solution was then analyzed by ICP-MS with results corrected for spectral inter-element interferences. Apart from Ba, Cr, Sn, V, W and Zr with detection limits that range from 0.3-5 µg/g, detection limits of the remaining trace elements ranged from 0.001-0.2 µg/g (Supplementary Table S1).

Results of duplicate analyses and analytical standards used are provided in Supplementary Table S2. Reproducibility of these reference samples is generally better than 5 % for concentrations more than 10 x above the detection limit, and typically 5-20 % closer to the detection limit.

4.2. Data compilation

The stratigraphic location of samples analyzed for whole rock chemistry in this study are shown in Fig. 1c. The new whole rock geochemical data of 29 whole rock ICP-MS and ICP-AES geochemical analyses from this study (Table 3) are compared with the ten Expedition 357 peridotite samples of Früh-Green et al. (2018) and the four Atlantis Massif peridotite samples of Godard et al. (2009) from Site 1309 in Figs. 3-10. We also compare these data with whole rock geochemical data compiled from global abyssal peridotites of Niu (2004), Paulick et al. (2006), and Godard et al. (2008).

5. Results

5.1. Whole rock chemistry major elements and Ni and Cr abundances

In MgO/SiO_2 vs. Al_2O_3/SiO_2 space (Fig. 3) the 'terrestrial array' represents the successive magmatic depletion (or melt extraction) trend of primitive mantle. Highly depleted compositions are characterized by low Al_2O_3/SiO_2 of < 0.01 (Jagoutz et al., 1979; Hart and Zindler, 1986). Verification of this melt extraction trend is reflected by a global data set of MOR peridotites (compilation of Niu, 2004; Paulick et al., 2006; Godard et al., 2008). Atlantis Massif serpentinized harzburgites record Al_2O_3/SiO_2 that range from ~ 0.01-0.04 indicating moderate to high degrees of magmatic depletion. Two Type I serpentinized dunites from the central sites (M0076B-3R1-78-82, M0076B-5R1-59-61, Table 1), and one dunite (1309D-31R-25-28) from Site U1309 reported by Godard et al. (2009) exhibit $Al_2O_3/SiO_2 < 0.01$. Very low Al_2O_3/SiO_2 values can alternatively be caused by replacive melt-rock interaction. Vertical deviations from the terrestrial array are indicative of Mg-Si mass transfer; peridotites that exhibit MgO/SiO_2 below the terrestrial array may reflect magnesium loss or silica addition during serpentinization or magnesium loss during seafloor weathering (Snow and Dick, 1995; Niu, 2004). A trend defined by increasing Al_2O_3/SiO_2 with most samples offset to moderately low MgO/SiO_2, as seen in the Atlantis Massif serpentinites (Fig. 3), can also be partially attributed to melt-impregnation processes (Niu, 2004). Half of the eight Type II melt-impregnated serpentinites of the eastern and central sites from this study and the study of Früh-Green et al. (2018) exhibit MgO/SiO_2 of < 0.9, consistent with this process; nonetheless, all melt-impregnated serpentinites plot within the range of the Type I serpentinites. Two central serpentinites yield MgO/SiO_2 values of ~ 0.76-0.86, within the lower range of the melt-impregnated serpentinites, which suggests that these two samples may also have been subjected to processes associated with melt-impregnation. Silica-metasomatism is characterized by low MgO/SiO_2 (< 0.55) and low Al_2O_3/SiO_2 (< 0.025). One exception is the talc schist, which exhibits low MgO/SiO_2 (~ 0.4) but high Al_2O_3/SiO_2 of 0.11, which suggests the addition of silicic melt (Paulick et al., 2006).

In Fig. 4 we plot MgO vs. selected major element oxides and loss on ignition (LOI) to illustrate the effects of serpentinization and multiphase alteration processes on major element chemistry. In terms of MgO and other major element oxides, the Type I serpentinites generally plot similarly to global MOR peridotites. Apart from two serpentinized harzburgites, which exhibit anomalously high Al_2O_3 and CaO, the remaining serpentinites have MgO contents that ranges from 41.25 to 46.06 wt.% and Mg# (Mg/Mg+Fe^{2+}) of 87.6-91.8 (Table 3). In SiO_2 vs. MgO space (Fig. 4a) the serpentinites and melt-impregnated serpentinites fall almost completely within the range of global abyssal peridotite and plot similarly to, but with slightly lower SiO_2 contents than the bulk composition of serpentine. In contrast, the Type III talc-altered serpentinites and talc schists plot near the bulk composition of talc and ODP Leg 209 talc-altered peridotites, but with slightly lower SiO_2 and MgO. The Ca-rich Type I serpentinites (6.66-13.30 wt.% CaO) plot off the linear array of the serpentinites and melt-impregnated peridotites in SiO_2 vs. MgO space with significantly lower SiO_2 at similar MgO. Fe_2O_3, Al_2O_3 and CaO contents (Figs. 4b-d) of the talc-altered serpentinites and talc schists generally fall within the range of the Type I and II serpentinites. Apart from two Type II melt-impregnated serpentinized harzburgites, which exhibit slightly higher Al_2O_3 contents than the remaining serpentinites, other major element oxide concentrations of the melt-impregnated serpentinites are similar to those of the serpentinites. CaO contents in the western site Type I serpentinites (Fig. 4d) record lower concentrations (0.05-0.30 wt.%) than those of the central and eastern sites. Similar to the SiO_2 vs. MgO plot, significant differences exist in LOI values between the Ca-rich serpentinites and all other serpentinites (Fig. 4e). Whereas the bulk of the peridotites exhibit LOI of ~ 12-14 wt.%, similar to those of global MOR peridotites and the talc-altered harzburgites and schists have low LOI contents that range from ~ 4-6 wt.%, similar to ODP Leg 209 talc-altered peridotites, the Ca-rich serpentinites have high LOI of ~ 16-20 wt.%. The Type II melt-impregnated serpentinites have LOI values that are up to ~ 9 wt.%, intermediate between those of the Type I and serpentinites and Type III serpentinites and schists.

The majority of the Expedition 357 serpentinites have Ni and Cr concentrations of ~ 1000-3000 µg/g (Table 3), similar to that of primitive mantle (PM), and fall within the range of global MOR peridotites (Supplementary Fig. S1). Exceptions are two central and two western serpentinite samples from Früh-Green et al. (2018), which range to Ni > 10000 µg/g and Cr > 30000 µg/g, and two central serpentinized dunites and two eastern melt-impregnated harzburgites from our study, which exhibit low Cr (< 400 µg/g).

5.2. Whole rock trace element concentrations

Significant differences in the relative degree of depletion, pattern morphology, and the existence of prominent element anomalies, e.g., conspicuous positive or Ce-anomalies depending on serpentinite type, are apparent on the basis of chondrite-normalized REE and PM-normalized incompatible trace element patterns (Fig. 5). Patterns range from those similar to and significantly more depleted than depleted MORB mantle (DMM) and mean abyssal peridotite in western Site M0071, central Sites M0069 and M0076, and Atlantis Massif IODP Site U1309 (Godard et al., 2009) to patterns enriched relative to DMM and mean abyssal peridotite as shown by central Site M0072 and most of eastern Site M0068. The serpentinites from eastern Site M0068 are atypical to other Expedition 357 serpentinites in that they exhibit LREE enrichments but HREE concentrations intermediate to that of DMM and mean abyssal peridotite. Central Site M0072 and eastern Site M0068 serpentinites typically exhibit REE concentrations that are more enriched than DMM and range from ~ 1-10 x chondrite; two M0068 talc schists are exhibit high REE concentrations of ~ 20 x chondrite.

Type I serpentinites sampled at western Site M0071, and central Sites M0069 and M0076 exhibit low Yb as well as low abundances of other incompatible elements, for example the high-field strength elements (HFSE) Nb and Zr (Table 3). Apart from one central Site M0072 serpentinized dunite with similarly low Yb, Nb and Zr, the remaining central Site M0072 and eastern site serpentinites, many of which are Type II melt-impregnated or Type III metasomatic serpentinites, exhibit comparatively higher concentrations of these incompatible elements (Table 1). As we show in Section 6.2.3, the melt-impregnated serpentinites, in particular in central Site M0072 and eastern Site M0068, show high concentrations of most incompatible elements relative to other sites.

Although the highly depleted Type I serpentinites from the western and central sites exhibit mostly concave upwards REE patterns with a steady decrease in REE abundances from the HREE to LREE, central Site M0072 Type I and Type II serpentinites exhibit flatter patterns; the eastern Types I, II and III serpentinites are atypical relative to the serpentinites to the west (i.e., at the central and western sites) in that they exhibit LREE enrichment. Excluding the lone, Ca-rich (12.46 wt.% CaO) serpentinized dunite with La/Sm_{CN} (CN denotes chondrite-normalized) of 4.70 and La/Yb_{CN} of 2.39, the western Type I serpentinites from Site M0071 exhibit mostly moderate but variable LREE/MREE fractionation (La/Sm_{CN} of 0.40-3.03) with La/Yb_{CN} ranging from 0.11-0.68. In contrast, the two eastern Type I serpentinites exhibit relatively minor LREE enrichment with La/Sm_{CN} and La/Yb_{CN} ranging from 1.08-1.17 and 1.13-1.30, respectively; the eastern Type II melt-impregnated serpentinites have higher LREE enrichments with La/Sm_{CN} = 1.72-2.15 and La/Yb_{CN} = 1.43-1.68 and the Type III metasomatic serpentinites have $LaSm_{CN}$ = 0.41-1.41 and La/Yb_{CN} = 0.48-1.36.

6. Discussion

On the basis of trace and rare earth element chemistry, we address differences in the compositions of the different serpentinite types to discriminate dominant fluid-rock interaction processes associated with serpentinization, from processes associated with mafic melt-rock interaction. We then provide estimates of degrees of partial melting (melt extraction) recorded in serpentinites sampled across the Atlantis Massif (IODP Exp. 357), before linking the geochemistry to processes associated with oceanic core complex formation.

6.1. Evidence of fluid-dominated serpentinization processes

Significant observations from the chondrite-normalized REE and PM-normalized patterns are: (1) prominent negative Ce-anomalies (i.e., Ce/Ce* where Ce* = $\sqrt{(La_{CN}*Pr_{CN})}$ and Ce = Ce_{CN}) in the western Type I serpentinites and two central Type I serpentinites, and positive Ce-anomalies in almost all eastern serpentinites (the vast majority of other central serpentinites show Ce/Ce* ~ 1); (2) extreme U-enrichment in many serpentinites with values that range to nearly 300 x PM; and (3) extreme Sr-anomalies with enrichments of up 100 x PM in most Ca-rich Type I serpentinites and depletion to below 0.1 x PM in the serpentinites of Sites M0072 and M0068.

With respect to the negative Ce-anomalies exhibited mostly by the western Type I serpentinites (site M0071), such anomalies in peridotites have been attributed to seawater-peridotite interaction (e.g., Frisby et al., 2016a, b) and indeed, (oxygenated) seawater itself exhibits a negative Ce-anomaly (e.g., Elderfield and Greaves, 1982).

The western site Type I serpentinites range to the highest U concentrations (5.05 µg/g), whereas the Type II melt-impregnated serpentinites of central site M0072 and eastern site M0068 range to the lowest U concentrations (0.01 µg/g) (Fig. 6a, Table 3), which suggests that U enrichment is associated with serpentinization and oxidation, and not melt-impregnation. Uranium enrichment in serpentinites is common as U is hosted by serpentine phases (e.g., Deschamps et al., 2010). Frisby et al. (2016a, b) have shown that U enrichments correlate with Ce anomalies and the amount of Nd derived from seawater, which is a proxy for water/rock values. Thus, U enrichments have been shown explicitly to reflect fluid-rock interaction in abyssal peridotites.

In the case of Sr enrichment (Fig. 6b), evidence is not as clear. However, we note that the Type II melt-impregnated central site M0072 and eastern site M0068 serpentinites range to the lowest Sr concentrations, with the former exhibiting the lowest concentrations of Sr (1.02-4.01 µg/g) of all sites, whereas the other sites locally show distinct Sr enrichments. This suggests that Sr enrichment is not associated with melt-impregnation.

6.2. Evidence for melt-impregnation processes: Enrichment in incompatible elements, LREE, LREE fractionations and ΣREE

As explained above, we infer melt-impregnation in central site M0072 serpentinites on the basis of compositional similarities with melt-impregnated serpentinites constrained on the basis of macroscopic and microscopic evidence, even though site M0072 serpentinites lack observable evidence of melt-impregnation at the scale of core and thin section. Hence, due to the absence of such mineralogical evidence, we term these M0072 serpentinites 'cryptically melt-impregnated'.

The HFSE, e.g., Th, Hf, Zr (Figs. 7a-c), Nb, and Ti are highest in Type II melt-impregnated serpentinites at central Site M0072 and eastern Site M0068 and lowest in western sites Type I serpentinites. In addition, Figures 7d and 7e show an increase in LREE and ΣREE, and possibly LREE fractionation from Type I serpentinites to Types II and III serpentinites, and from west to central to east. For example, apart from a lone Ca-rich Type I serpentinized dunite, which exhibits anomalously high La and anomalously low Ce and La/Yb_{CN} of 2.39, the remaining western Type I serpentinites yield La/Yb_{CN} of 0.11-0.47 and mean ΣREE of 0.39 µg/g (including the Ca-rich dunite). The central Type I and II serpentinites yield a range of La/Yb_{CN} of 0.15-1.31 and mean ΣREE of 2.40 µg/g, and the eastern Types I, II and III serpentinites yield a range of La/Yb_{CN} of 0.61-1.68 and mean ΣREE of 12.66 µg/g. Thus, overall, melt impregnation produces less LREE fractionation and more elevated ΣREE compared to processes dominated by fluid-rock interaction.

6.3. Evidence of silica metasomatism

Talc- and amphibole-rich fault rocks form as the result of silica metasomatism and have been recovered from detachment fault surfaces along slow and ultra-slow spreading mid-ocean ridges including oceanic core complexes (e.g., Escartín et al., 2003; Schroeder and John, 2004; Boschi et al., 2006b; McCaig et al., 2007; Picazo et al., 2021). These rocks record heterogeneous deformation under greenschist-facies conditions and are commonly restricted to localized shear zones (< 200 m), which are associated with intense talc-amphibole metasomatism (Escartín et al., 2003; Boschi et al., 2006b). Talc is mechanically weak and thus may be critical to the development of such fault zones and may enhance unroofing of upper mantle peridotites and lower crustal gabbroic rocks during seafloor spreading. In the case of the Atlantis Massif, talc metasomatism is associated with serpentinite dehydration (Boschi et al., 2008). Strontium isotope compositions of talc-rich fault rocks indicate that talc metasomatism along detachment faults occurs at low water/rock values (0.2–0.7) and reflect interaction with Si-rich, evolved fluids with a mafic component derived from interaction with gabbro lenses within a peridotite-dominated ridge segment (Boschi et al., 2008).

In our study, silica metasomatism is reflected by plots of MgO/SiO_2 vs. Al_2O_3/SiO_2 (Fig. 3) and MgO vs. SiO_2 (Fig. 4a). These figures demonstrate the distinct whole rock geochemistry of the talc-altered Type III metasomatic serpentinites and talc schists from the eastern site M0068. In MgO vs. SiO_2 space (Fig. 4a), the talc-bearing serpentinites and talc schists are clearly distinct from all other Exp. 357 serpentinites by much lower MgO and much higher SiO_2 contents. These low MgO/SiO_2 and Al_2O_3/SiO_2 values of < 0.02 are indicative of silica metasomatism and are close to compositions of talc-bearing harzburgites recovered during ODP Leg 209 (Paulick et al., 2006).

6.4. Discrimination of fluid-rock vs. melt-dominated processes

6.4.1. Comparison with global abyssal peridotites

Figure 8a highlights trace element variations of mean global abyssal peridotites with compositions dominated by melt-rock interaction vs. those dominated by fluid-rock interaction associated with serpentinization (as interpreted by Paulick et al., 2006). We note that (in Fig. 8) we are comparing patterns, as absolute concentrations are subject to other processes (e.g., melt addition). Serpentinites subjected to mafic melt-impregnation exhibit enrichments in incompatible elements relative to those that have not been affected by melt-impregnation (Fig. 8a). In Figure 8b, we plot the mean serpentinite composition of each Expedition 357 location (i.e., west, central, east) vs. the mean compositions of melt-dominated and fluid-dominated global abyssal peridotites as shown in Fig. 8a. In Fig. 8c, we parse the mean peridotite compositions according to borehole of the central sites. There are clear differences in incompatible element concentrations between Exp. 357 Type II melt-impregnated serpentinites and Type III metasomatic serpentinites relative to Type I serpentinites, with Types II and III exhibiting greater abundances of all incompatible elements (Fig. 8b). In particular, the Type I serpentinites from the western site have PM-normalized incompatible element abundances that are most similar to fluid-dominated peridotites, whereas central sites serpentinites exhibit concentrations most similar to melt-dominated peridotites; eastern site serpentinites have incompatible abundances more enriched than melt-rock dominated peridotites (Fig. 8b). Apart from U and Sr, the Exp. 357 serpentinites show a clear enrichment in all other incompatible elements from the western to central to eastern sites (Fig. 8b).

6.4.2. HFSE vs. LREE

On the basis of selected HFSE vs. LREE and HFSE vs. MREE/HREE variations, Paulick et al. (2006) showed that the global abyssal peridotite dataset of Niu (2004) exhibit relatively steep positive trends, which was interpreted as indicative of dominant melt-rock interaction processes. The reason for this trend is related to differences in the behavior of LREE and HFSE; LREE are more hydrophilic than HFSE, and so are more readily transported in solution. Although melt-rock reaction mobilizes both LREE and HFSE, fluid-dominated reactions preferentially mobilize LREE, resulting in distinctly different patterns (Niu, 2004). A trend defined by only minor increase in HFSE concentrations (i.e., a sub-horizontal as opposed to steep positive trend) on the other hand, is indicative of dominantly hydrothermal alteration processes (i.e., fluid-rock interaction), which affect the more immobile HFSE to a lesser extent than the REE (Paulick et al., 2006). In the dataset of ODP Leg 209 peridotites, Paulick et al. (2006) showed that those at Sites 1270 and 1271 exhibit steep trends similar to the dataset of Niu (2004), whereas those of Sites 1268, 1272 and 1274 show less steep, subhorizontal trends, which they interpreted as more consistent with fluid-rock interaction.

Fig. 9 shows Expedition 357 serpentinites vs. the trends of global abyssal peridotites, with compositions dominated by (i) melt-rock interaction, and (ii) fluid-rock interaction in Nb vs. La and Ti vs. Dy space. These plots produce two distinct linear trends, which mimic the two described above, in agreement with the observations presented in Fig. 8. The serpentinites of the central and eastern sites, which show ample evidence of melt-impregnation, exhibit steep trends indicative of compositions dominantly controlled by melt-rock interaction similar to those of the global MOR peridotite dataset of Niu (2004) and ODP Leg 209 Sites 1270 and 1271 of Paulick et al. (2006). In contrast, Type I serpentinites from the western site, which show minimal evidence of melt-impregnation, instead show flatter, subhorizontal trends suggestive of compositions mostly controlled by fluid-rock reactions, similar to trends of peridotites of ODP Leg 209 Sites 1268, 1272 and 1274. We note also that similar relations and trends occur on other plots of HFSE vs. LREE and MREE (e.g., Th vs. Ce, Ti v. Ce, Hf vs. Pr, Nb vs. $[Gd/Lu]_{CN}$ and Ti vs. $[Gd/Lu]_{CN}$, Supplementary Fig. S2). In the case of Expedition 357 serpentinites, in all instances, the slope of the trends of the central and eastern site serpentinites are steeper than the slope of the trend of the western site serpentinites, consistent with compositions of the former being the result of dominant melt-rock reaction and compositions of the latter being the result of dominantly fluid-rock interaction. When the central location is parsed into discrete sites, compositions of serpentinites from central Site M0069 are consistent with being dominated by fluid-rock interaction, whereas those of central Sites M0072 and M0076 are consistent with being dominated by melt-rock interaction.

6.5. Petrogenesis: Estimates of degrees of melt extraction

Chondrite-normalized REE and PM-normalized patterns (Fig. 5) are used to explain differences in the relative depletion of peridotites of each site investigated and provide evidence of fluid-dominated processes and melt-impregnation processes

(Sections 6.1.-6.4.), based on the compositional variation of Expedition 357 serpentinites. Below, we model estimates of partial melting undergone by the peridotites based on trace and REE chemistry.

Various highly incompatible and immobile trace elements (Yb, Nb, Zr) in serpentinites from western Site M0071 and central Sites M0069 and M0076 exhibit extreme depletion relative to DMM, in contrast to the central Site M0072 serpentinites that exhibit enriched chondrite-normalized patterns relative to DMM apart from a lone moderately depleted Type I serpentinized dunite. The eastern Site M0068 serpentinites exhibit LREE concentrations more enriched than DMM but HREE slightly to moderately more depleted than DMM. Evidence in support of high degrees of melt depletion includes the high depletion in Al_2O_3 and CaO (Fig. 4), and the aforementioned other incompatible trace elements (Fig. 7, Table 3). Below, we provide estimates of the maximum degrees of melt extraction based on modelling of whole rock REE concentrations and note that REE patterns of many samples are strongly affected by refertilization, which thus needs to be taken into account to derive accurate estimates of melt depletion.

The REE patterns of the most melt-depleted sample for each of the five sites are shown in Fig. 10 and compared with curves predicted by modeling of melt depletion followed by subsequent metasomatism. As LREE are most strongly depleted during partial melting, and therefore sensitive to refertilization, this part of the REE pattern is essentially that of the metasomatizing agent. As a result, different amounts of metasomatism will shift the LREE pattern up or down, but the slope of the LREE pattern (La/Sm) is barely affected. This slope is strongly variable in our dataset, ranging from LREE-depleted ($[La/Sm]_{CN}$ = 0.3-0.9) to strongly enriched ($[La/Sm]_{CN}$ = 2-5). The REE patterns in Figs. 5a-e show at least two distinct melts that have infiltrated the peridotites, an enriched (*E*) and a depleted type (*D*), of which the most REE-rich examples are from eastern Site M0068 (samples 68A-1R1-34-35 and 68A-1R1-1-6). In these samples, the original peridotite REE patterns have been completely overprinted by the infiltrating melts. Therefore, we chose these peridotites to estimate the composition of the two endmember contaminants during modeling (*E* and *D*, respectively). Both types can be observed at each site, although central Sites M0072 and M0076 are dominated by a *D*-type contaminant. Some serpentinites show evidence of infiltration by an even more enriched contaminant (*SE*), the composition of which is more difficult to estimate. As this contaminant is strongly LREE-enriched and therefore relatively HREE poor, its exact composition will have little effect on our melt fraction estimates, which are based on the HREE part of the patterns.

The calculated volume of fractional non-modal melt extraction (see Fig. 10 caption for model parameters) of the most depleted sample from each site ranges from 19 to 21 % (Fig. 10), which indicates little difference in the maximum amount of melt extraction between the sites. The difference in the REE patterns between the sites are primarily due to small but variable amounts of infiltrating melts (<1 % for each of the five most depleted samples, Fig. 10).

These modeling results show little difference in the maximum amount of melt extraction between the different sites across the footwall. Unfortunately, significant melt infiltration experienced by many of the serpentinites makes it difficult to evaluate the average amount of melt extraction experienced by serpentinites of the different sites. For example, nearly all whole rock compositions of eastern Site M0068 and central Site M0072 are more enriched than DMM, which could be interpreted as very limited melt extraction, but refertilization of these samples will have obliterated any previous melt extraction history. Our modeling results suggest that differences in REE patterns observed between sites are probably due to differences in refertilization, not partial melting.

6.6. Spatial variations in geochemical processes and peridotite composition

It was noted by Früh-Green et al. (2018) that there exists a weakly defined enrichment in peridotites from west to east. This pattern is actually strongly defined in terms of enrichment in LREE, LREE fractionation, ΣREE, and HFSE (Figs. 7-9 and Supplementary Fig. S2). For example, Fig. 8 shows a distinct increase in all incompatible elements except U, Pb, and Sr in the mean serpentinite compositions moving from west to central to east. Specifically, the western Type I serpentinites exhibit the lowest concentrations of HFSE of Nb, Zr, and Th whereas the eastern serpentinites exhibit the highest concentrations of these elements (Figs. 7a-c); the central serpentinites have concentrations intermediate to the western and eastern serpentinites. However, as we have also noted, there are distinctions in the central location when parsed into individual sites with central Site M0069 being depleted to the same degree as the western serpentinites and with the two other central sites (M0072 and M0076) being comparatively more enriched.

Moreover, this pattern of west to east enrichment is complementary to the relative volume of melt-impregnation and silica metasomatism recorded in sampled peridotite at each site. The eastern site comprises the largest percentage of melt-impregnated and silica-metasomatized peridotites (70%), relative to the central sites (35%), and the western site (a single sample out of nine, or 11%, is melt-impregnated, with no Type III silica-metasomatized serpentinites). However, the calculation for the central sites is underestimated as we do not include here the four cryptically melt-impregnated serpentinites of central Site M0072 from our dataset, which show no macroscopic or microscopic evidence of melt-impregnation. If we recalculate with the inclusion of these four M0072 serpentinites, the percentage of melt-impregnated and silica-metasomatized peridotites from the central sites increases to 52 %.

6.7. Links to OCC processes

The observed spatial variations in serpentinite composition needs to be interpreted in the context of both the limitations of our observations and taking into account the complex history of detachment fault formation and exhumation. We have shown that the western site Type I serpentinites record compositions consistent with dominantly fluid-rock interaction processes, whereas the central site serpentinites, considered collectively, and those from the eastern site record compositions consistent with having undergone dominant melt-rock interaction. Furthermore, there is a clear progression in the volume of melt-impregnations from west to central and east and a corresponding increase in incompatible element enrichment, a record of these increasing volumes of melt-enrichment.

Serpentinites from the western sites originated from shallower borehole depths of ~ 0-10 m relative to those of the central sites (a maximum of ~ 16 m in the cases of central Sites M00069A and M0076A, Fig. 1c). The present-day position of these samples cannot be directly related to that of the history of each sample, from lithospheric emplacement, subsequent interaction with melt, alteration, and exhumation. First, the detachment fault zone is likely a complex, anastomosing structure, with a thickness of ~100 m to ~ a few 100s of m (e.g., Karson et al., 2006; Escartín et al., 2017; Parnell-Turner et al., 2018), where fault blocks are transposed in the across-axis direction. In this case, variations in composition vs. borehole depth may not correspond to actual structural depths relative to the fault surface exposed at the seafloor, and now adjacent materials may have originated from different positions in the deformed fault zone. Second, the boreholes also include talus material that is therefore not *in situ*. The present-day location of these samples cannot be directly interpreted as an indicator of spatial and temporal relationships with samples *in situ*, and therefore have an ambiguous structural position. If these debris fields correspond to local mass-wasting deposits, visible at small scales over the detachment fault, the present-day position may be close to the original *in situ* position. Oceanic detachments also display a cover of rubble and sediment that is sourced from the hanging wall, and rafted during extension (e.g., Dick et al., 2008; Escartín et al., 2017). Thus, if the talus material corresponds to rubble cover, its source may be the hanging wall rather than the fault zone or footwall instead, and its present-day location does not necessarily reflect its position at the time of formation, emplacement, impregnation, or alteration.

The consistent grouping of samples with a similar melt-impregnation (or lack thereof) and alteration history at the eastern, central, and western sites may suggest that *in situ* samples have not witnessed significant (km-scale), lateral transposition along the fault zone, or at least at spatial scales that are smaller than any local spatial variation associated with melt-rock interactions. Similarly, the samples that are not *in situ*, with similar melt impregnation and alteration histories, suggest a local source; sampling of hanging wall rubble would likely result in an extremely heterogeneous and variable set of ultramafic samples, as observed from the rubble cover from other oceanic detachments (e.g., Escartín et al., 2007). The homogeneity is therefore consistent with a local origin, with material sourced from the mass-wasted fault zone, eventually mixed with basaltic rubble that is present in the boreholes (e.g., Früh-Green et al., 2018).

If the samples were either *in situ*, or sourced locally where *ex situ*, and if the lateral transposition of material within an anastomosing fault zone occurs at a smaller scale (< 1 km parallel to extension) than the distance between sites (3-5 km), then spatial patterns observed may be interpreted in the context of the internal structure and evolution of the

OCC and its detachment fault. Ildefonse et al. (2007) suggested a temporal variation in melt supply to the ridge axis, with an initial phase of accretion that has limited melt supply, and a late phase of accretion with increased melt supply and the emplacement of gabbros in the footwall. This interpretation is consistent with early peridotites just showing melt extraction (western sites), and melt-rock reactions in more recent time associated with this recent magmatic phase (eastern sites).

Alternatively, the sites may simply record an inherently heterogeneous system, where melt percolation, and hence melt-rock reactions, are inherently inhomogeneous. If this is the case, the east-west patterns may not reflect a temporal evolution but instead indicate that these heterogeneities occur over distances of a few km, corresponding to the separation among the different sites. This interpretation is consistent with geological observations and drilling that document a change in footwall composition along-axis, with peridotites near the transform fault wall, and gabbros ~ 10 km to the north, hence at spatial scales similar to those shown by the western, central, and eastern sites.

7. Conclusions

Peridotites sampled during IODP Expedition 357 comprise predominantly Type I serpentinites, with lesser Type II melt-impregnated and Type III metasomatic serpentinites. A principal variation in the nature and composition of Expedition 357 serpentinites is an increase in the volume of melt-impregnation products and a concomitant increase in HFSE and LREE enrichments from the western to central to eastern sites. Whole rock chemical compositions of western site Type I serpentinites are consistent with dominantly fluid-rock interaction associated with serpentinization and oxidation, whereas compositions of eastern site Type II melt-impregnated and Type III metasomatic serpentinites are dominated by melt-rock interaction processes. High to moderate degrees of melt extraction in the peridotites are evident in low concentrations of Al_2O_3, CaO and incompatible elements. Degrees of melt extraction based on whole rock REE suggest a high range of 19-21 % with no apparent variation between sites. Some serpentinite samples are rubble and therefore *ex situ*. Thus, the coherent magmatic history observed at each site may be consistent with a local source originating in the fault zone rather than rafted rubble that would be expected to show more heterogeneity and no spatial pattern. If this is accurate, our sites may provide a time-record of enhanced melt-rock interaction with time, consistent with proposed geological models. Otherwise, the magmatic history may represent heterogeneities in these processes at spatial scales of a few km.

Acknowledgments

This research used samples and data provided by the International Ocean Discovery Program (IODP). This project would not have been possible without the support of the entire IODP Expedition 357 scientific party and support staff from the ECORD Science Operator. In particular, we thank co-Chief Scientist Beth Orcutt, Expedition Project Managers Carol Cotterill and Sophie Green, Offshore Operations Manager David Smith, the ESO Laboratory and Curation Manager Ursula Roehl, and the entire team of the Bremen Core Repository at MARUM. Funding for Expedition 357 was provided by the European Consortium for Ocean Research Drilling (ECORD). SAW acknowledges financial support from the Korea International Ocean Discovery Program (K-IODP) funded by the Ministry of Oceans and Fisheries, Korea and internal funds provided by KFUPM Dept. of Geosciences. GFG acknowledges funding by the Swiss National Science Foundation (SNF) project No. 200021_163187 and Swiss IODP. MIL acknowledges that this research was undertaken thanks in part to funding from the Canada First Research

Excellence Fund through the Arthur B. McDonald Canadian Astroparticle Physics Research Institute.

Figure captions

Figure 1. (a) Location of the Atlantis Massif at 30°N within the context of the greater MAR spreading system (modified from Kelley et al., 2001). (b) Bathymetric map centered on the southern wall of the Atlantis Massif (modified after Rouméjon et al., 2018a). Inset shows the location of the Atlantis Massif on the western flank of the Mid-Atlantic Ridge axial valley, bordered to the south by the Atlantis Fracture Zone. Circles with numbers in italics and beginning with M00 represent shallow drill hole locations from IODP Exp. 357 (Früh-Green et al., 2017, 2018). White circles indicate drill holes with no recovered peridotite; blue, red and yellow circles represent western (M0071), central (M0069, M0072, M0076) and eastern (M0068) sites, with recovered peridotite samples investigated in this study. White squares represent sites (U1309, U1310, U1311) drilled during Exp. 304/305 (Blackman et al., 2006); white star shows the location of the Lost City Hydrothermal Field (LCHF) (Kelley et al., 2001). (c) Simplified downhole plots showing dominant rock types recovered in the seven drill holes hosting serpentinized peridotites (modified from Roumejon et al., 2018a; see Fruh-Green et al., 2018 for complete expedition drill hole vertical sections). The sections are arranged from right to left according to longitude (see Fig. 1b), and from hole top to bottom. The central holes embody *in situ* segments of the detachment footwall, whereas the western and eastern site holes which yield rubbly intervals and sedimentary structures are interpreted as artefacts of mass wasting and local faulting. Symbols: circles, harzburgite; squares, dunite; triangles, Ca-rich harzburgite; triangles with slash, Ca-rich dunite; crosses, melt-impregnated harzburgite; x's, plagioclase-impregnated harzburgite; diamonds, talc-

amphibole altered harzburgite; diamonds with slash; talc-amphibole-chlorite schist. Blue, red and yellow symbols represent samples of western, central and eastern serpentinized harzburgites and dunites, respectively, analyzed for whole rock chemical analysis. Note 'metamafic' includes metabasalt, metadolerite and metagabbro composition samples.

Figure 2. Representative thin section images of Expedition 357 Type I serpentinites (a-d), Type II (mafic) melt-impregnated (mm-i) serpentinite (e, f) and Type III metasomatic serpentinites (msp) (g, h). 'Typical' completely serpentinized peridotite samples from (a, b) 71A-1R2-85-89, harzburgite and (c) 71C-5R1-6-8, harzburgite. (d) Ca-rich serpentinized harzburgite 69A-9R2-8-12 showing extensive network of carbonate veinlets. (e, f) Mafic melt-impregnated (mm-i) harzburgites 76B-7R1-81-83 and 68B-4R1-23-29 with (e) the presence of rare plagioclase feldspar (f) and secondary (replacive) olivine mantling partially dissolved orthopyroxene porphyroclast. (e) Talc-amphibole altered (t-aa) harzburgite 68B-1R1-10-13, showing replacement of orthopyroxene by talc (Tlc) and tremolite (Tr), and (f) talc-schist 68B-1R1-1-6. Image (a) is under plane polarized light; images in (b-h) are under cross-nicols.

Figure 3. Plot of MgO/SiO_2 vs. Al_2O_3/SiO_2 for all studied serpentinites (top panel, Type I serpentinites, bottom panel, Type II melt-impregnated and Type III metasomatic serpentinites). The lighter shaded samples (light yellow, light blue and pink) of the same shape here and in all other figures are Expedition 357 Atlantis Massif peridotites from Früh-Green et al. (2016); light orange circles and squares harzburgites and dunites, respectively, from IODP Site U1309 Atlantis Massif peridotites (Godard et al., 2009). Global abyssal peridotite data from Niu (2004), Paulick et al. (2006) and Godard et al. (2008), unless stated otherwise. Fields of serpentinized peridotite and talc-altered

peridotite are from Paulick et al. (2006) and melt-impregnated peridotites (MIP) are from Paulick et al. (2006), Godard et al. (2008) and as referenced in Whattam et al. (2011). DMM (depleted MORB mantle) and PM (primitive mantle) from Workman and Hart (2005) and Palme and O'Neill (1983) respectively. The terrestrial array is from Jagoutz (1979).

Figure 4. Variation diagrams of MgO vs. (a) SiO_2, (b) Fe_2O_3, (c) Al_2O_3, (d) CaO and (e) LOI of Atlantic Massif serpentinites from this study, and peridotites of Godard et al. (2009) and Früh-Green et al. (2018) compared with global MOR peridotite and bulk compositions of serpentine and talc (Blanco-Quintero et al. 2011, mean of ten and eight serpentine and talc analyzes). Symbols as in Fig. 3.

Figure 5. (a-e) Chondrite-normalized REE and (f-j) primitive mantle-normalized incompatible element plots of Atlantis Massif serpentinites from this study and peridotites of the study of Früh-Green et al. (2018). Chondrite and primitive mantle values are from McDonough and Sun (1995). Shown for comparison is mean abyssal peridotite composition determined on the compilations of Niu (2004) and Bodinier and Godard (2003) by Godard et al. (2008), and depleted MORB mantle (DMM) (Workman and Hart, 2005).

Figure 6. IODP Expedition 357 serpentinite samples from this study, and peridotites of the study of Früh-Green et al. (2018) on plots of (a) U and (b) Sr vs. site. Note that three of the four high-CaO Type I serpentinites (with 5.59-10.50 wt.% CaO) also exhibit the highest concentrations of Sr (> 1000 µg/g). Symbols as in Fig. 3.

Figure 7. Expedition 357 Atlantis Massif serpentinites from this study and peridotites of the study of Früh-Green et al. (2018) in plots of (a) Th, (b) Hf, (c) Zr, (d) Ce/Yb and (e) total REE vs. site. Plotted for comparison are the ranges of fluid-rock dominated and melt-rock dominated global abyssal peridotite (GAP, references as in the caption for Fig. 5). Depleted mantle (DM) and primitive mantle (PM) compositions are from Workman and Hart (2005) and Lyubetskaya and Korenaga (2007), respectively. Symbols as in Fig. 3.

Figure 8. Primitive mantle-normalized plots of the mean compositions of (a) global abyssal peridotites interpreted as being dominated by fluid-rock and melt-rock reactions, (b) Atlantis Massif serpentinites from this study and (c) central serpentinites parsed into site. The fluid-rock dominated peridotite is from Paulick et al. (2006) and represent peridotites collected during ODP Leg 209, Sites 1268, 1772, 1274. The melt-rock dominated peridotite is from Niu (2004) and Paulick et al. (2006) and in the case of Paulick et al. (2006), represent peridotites collected from ODP Leg 209, Sites, 1270, 1271. Symbols as in Fig. 3

Figure 9. Expedition 357 Atlantis Massif serpentinites from this study and peridotites of the studies of Godard et al. (2009) and Früh-Green et al. (2018) in plots of (a, b) Nb vs. La, and (c, d) Ti vs. Dy. Element abundances listed as '0' were assumed to be below detection limit and not used in calculation of the regression. Colors of the regressed lines and text for the Expedition 357 serpentinites include: blue, western; red, central; and black, eastern. In (b) and (d), the light blue, pink and light grey regressed lines represent mean of the western, central and eastern sites (i.e., the blue, red and black lines in (a) and (c)). R^2 values shown for Exp. 357 serpentinites represent ones which include the peridotite samples of Früh-Green et al. (2018) in addition to the serpentinites from this

study and the numbers in italics in brackets beside R^2 values represent number of samples used in regression calculation. The orange line represents the dataset of Atlantis Massif peridotites from Site U1309 (Godard et al., 2009). Linearly regressed vectors (grey) labelled *A*, *B*, and *C* in (a) and (c) represent data from global abyssal peridotite (GAP) and for visual clarity, samples are omitted from the plot. The *A* trend represents the dataset of Niu (2004) which was interpreted by Paulick et al. (2006) as being representative of dominant melt-rock interaction (i.e., melt-impregnation); *B* and *C* are from Paulick et al. (2006) and represent peridotites interpreted as having compositions dominantly associated with melt-rock reaction (*B*, ODP Leg 209, MAR, Sites, 1270, 1271) and fluid-rock reaction (*C*, Sites 1268, 1772, 1274). Depleted mantle (DM) and primitive mantle (PM) compositions from Workman and Hart (2005) and Lyubetskaya and Korenaga (2007), respectively. Symbols as in Fig. 3.

Figure 10. (a) REE compositions of the most melt-depleted sample from each site compared with model estimates of 10, 15, and 20 % partial melting of DMM as well as three ‘best fit’ models of melting and subsequent refertilization to estimate the extent of melting experienced by these samples. Modeling is of non-modal fractional melting (dashed curves encompassing light green shade) of partial melting in % (10, 15, 20) of a four phase DMM spinel lherzolite source comprising ol: opx: cpx: sp in modal proportions of 0.53: 0.27: 0.17: 0.03 and a melt mode of -0.06: 0.28: 0.67: 0.11 (Hellebrand et al. 2002). Initial source composition, DMM from Workman and Hart (2005). Partition coefficients from Suhr et al.,1998; missing REE interpolated. Also indicated are compositions of rocks after 20 % non-modal fractional melting and subsequent 1 % or 10 % addition of a mafic melt (mm, uppermost grey shaded area) with a REE composition of the most enriched sample (eastern site M0068A-1R1-34-35 talc-

schist, Früh-Green et al., 2018, see Fig. 4e) as a proxy for a slightly LREE-enriched melt (darker green shade). Symbols as in Fig. 3.

Table captions

Table 1 Evidence and means for classification of Expedition 357 serpentinites subjected to melt-impregnation and (silica) metasomatism.

Table 2 Mineralogy and modalogy of Expedition 357 serpentinites.

Table 3 Whole rock ICP-AES and ICP-MS analyses of Expedition 357 Atlantis Massif serpentinites from this study.

Supplementary material

See Supplementary Document

References

Absalov, M.Z., 1998. Chrome-spinels in gabbro-wehrlite intrusions of the Pechenga area, Kola Peninsula, Russia: emphasis on alteration features. Lithos 43, 109-134.

Andreani, M., Mével, C., Boullier, A.-M., Escartin, J., 2007. Dynamic control on serpentine crystallization in veins: constraints on hydration processes in oceanic peridotites. Geochemistry, Geophysics, Geosystems 8 (2), Q02012.

Akizawa, N., Früh-Green, G.L., Tamura, A., Tamura, C., Morishita, T., 2020. Compositional heterogeneity and melt transport in mantle beneath Mid-Atlantic Ridge constrained by peridotite, dunite, and wehrlite from Atlantis Massif. Lithos 354-355, 105364. https://doi.org/10.1016/j.lithos.2019.105364.

Andreani, M., Mevel, C., Boullier, A.-M., Escartin, J., 2007. Dynamic control on serpentine crystallization in veins: constraints on hydration processes in oceanic peridotites. Geochemistry, Geophysics, Geosystems 8.

Arai, S., Abe, N., Hirai, H., 1998. Petrological characteristics of the sub-arc mantle: An overview on petrology of peridotite xenoliths from the Japan Arcs. Trends in Mineralogy 2, 39-55.

Arai, S., Matsukage, K., 1996. Petrology of gabbro-troctolite–peridotite complex from Hess Deep, equatorial Pacific: implications for mantle–melt interaction within the oceanic lithosphere. In: Mével, C., Gillis, K.M., Allan, J.F., Meyer, P.S. (Eds.), Proceedings of the Ocean Drilling Program: Scientific Results, 147, pp. 135-155.

Arai, S., Shimizu, Y., Ismail, S.A., Ahmed, A.H., 2006. Low-T formation of high-Cr spinel with apparently primary chemical characteristics within podiform chromitite from Rayat, northeastern Iraq. Mineralogical magazine 70(5), 499-508.

Aswad, K.J.A., Aziz, N.R.H., Koyi, H.A., 2011. Cr-spinel compositions in serpentinites and their implications for the petrotectonic history of the Zagros Suture Zone, Kurdistan Region, Iraq. Geological Magazine 148(5-6), 802-818. doi:10.1017/S0016756811000422.

Bach, W., Klein, F. 2009. The petrology of seafloor rodingites:: Insights from geochemical reaction path modelin. Lithos 112(1-2), 103-117. http://dx.doi.org/10.1016/j.lithos.2008.10.022.

Ballhaus, C., Berry, R.F., Green, D.H., 1991. High pressure experimental calibration of the olivine-orthopyroxene-spinel oxygen barometer, implications for the oxidation of the mantle. Contributions to Mineralogy and Petrology 107, 27-40.

Barnes, S.J., 2000. Chromite in komatiites II. Modification during greenschist to mid-amphibolite facies metamorphism. Journal of Petrology, 41, 387-409.

Barnes, S.J., Roeder, P.L., 2001. The range of spinel compositions in terrestrial mafic and ultramafic rocks. Journal of Petrology 42(12), 2279-2302.

Barra, F., Gervilla, F., Hernández, E., Reich, M., Padrón-Navarta, J.A., González-Jiménez, J.M., 2014. Alteration patterns of chromian spinels from La Cabaña peridotite, south-central Chile. Mineralogy and Petrology 108, 819-836. DOI 10.1007/s00710-014-0335-5.

Bedini, R.M., Bodinier, J.-L., 1999. Distribution of incompatible trace elements between the constituents of spinel peridotite xenoliths: ICP-MS data from the East African Rift. Geochimica et Cosmochimica Acta, 63(22), 3883-3900.

Bhat, I.M., Ahmad, T., Subba Rao, D.V., 2019. Alteration of primary Cr-spinel mineral composition from the Suru Valley ophiolitic peridotites, Ladakh Himalaya: Their low-temperature metamorphic implications. Journal of Earth System Science 128:188. https://doi.org/10.1007/s12040-019-1222-6.

Blackman, D.K., Cann, J.R., Janssen, B., Smith, D.K., 1998. Origin of extensional core complexes: evidence from the Mid-Atlantic Ridge at Atlantis Fracture Zone. Journal of Geophysical Research: Solid Earth 103, 21315-21333.

Blackman, D.K., Karson, J.A., Kelley, D.S., Cann, J.R., Früh- Green, G.L., Gee, J.S., Hurst, S.D., John, B.E., Morgan, J., Nooner, S.L., Ross, D.K., Schroeder, T.J., Williams, E.A., 2002. Geology of the Atlantis Massif (Mid-Atlantic Ridge, 30° N): implications for the evolution of an ultramafic oceanic core complex. Marine Geophysical Researches 23, 443-469.

Blackman, D.K., Ildefonse, B., John, B.E., Ohara, Y., Miller, D.J., MacLeod, C.J., 2006. Proceedings of the IODP, 304/305. College Station TX. doi:10.2204/iodp.proc.304305.2006. (Integrated Ocean Drilling Program Management International, Inc.).

Blanco-Quintero, I.F., Proenza, J.A., García-Casco, A., Tauler, E., Galí, S., 2011. Serpentinites and serpentinites within a fossil subduction channel: La Corea mélange, eastern Cuba. Geologica Acta 9 (3-4), 389-405. DOI :10.1344/105.000001662.

Bodinier, J.L., Godard, M., 2003. Orogenic, ophiolitic, and abyssal peridotites. Treatise on Geochemistry, vol. 2. Elsevier, Amsterdam, pp. 103-170.

Bodinier, J.L., Menzies, M.A., Thirlwall, M.F., 1991. Continental to oceanic mantle transition: REE and Sr–Nd isotopic geochemistry of the Lanzo Lherzolite Massif. Journal of Petrology Special Volume 2, 191-210.

Boschi, C., Früh-Green, G.L., Delacour, A., Karson, J.A., Kelley, D.S., 2006a. Mass transfer and fluid flow during detachment faulting and development of an oceanic core complex, Atlantis Massif (MAR 30°N). Geochemistry, Geophysics Geosystems 7 (1), Q01004.

Boschi, C., Früh-Green, G.L., Escartin, J., 2006b. Occurrence and significance of serpentinite-hosted, talc-rich fault rocks in modern oceanic settings and ophiolite complexes. Ofioliti 31 (2), 123–134.

Boschi, C., Dini, A., Früh-Green, G.L., Kelley, D.S., 2008. Isotopic and element exchange during serpentinization and metasomatism at the Atlantis Massif (MAR 30°N): insights from B and Sr isotopes. Geochimica et Cosmochimica Acta 72 (7), 1801–1823.

Burkhard, D.J.M., 1993. Accessory chromian spinels: Their coexistence and alteration in serpentinites. Geochimica et Cosmochimica Acta 57, 1297-1306.

Cannat, M., 1993. Emplacement ofmantle rocks in the seafloor at mid-ocean ridges. Journal of Geophysical Research: Solid Earth 98 (B3), 4163-4172.

Cannat, M., Karson, J.A., Miller, D.J., Agar, S.M., Barling, J., Casey, J.F., Ceuleneer, G., Dilek, Y., Fletcher, J.M., Fujibayashi, N., Gaggero, L., Gee, J.S., Hurst, S.D., Kelley, D.S., Kempton, P.D., Lawrence, R.M., Marchig, V., Mutter, C., Niida, K., Rodway, K., Ross, D.K., Stephens, C.J., Werner, C.-D. and Whitechurch, H., 1995. Mid-Atlantic Ridge: Sites 920–924. Proc. ODP, Initial Reports, 153. Ocean Drilling Program, Texas A&M University, College Station, TX, United States.

Cann, J.R., Blackman, D.K., Smith, D.K., McAllister, E., Janssen, B., Mello, S., Avgerinos, E., Pascoe, A.R., Escartín, J., 1997. Corrugated slip surfaces formed at ridge-transform intersections on the Mid-Atlantic Ridge. Nature 385, 329-332.

Dare, S.A.S., Pearce, J.A., McDonald, I., Styles, M.T., 2009. Tectonic discrimination of peridotites using fO_2–Cr# and Ga–Ti–Fe^{III} systematics. Chemical Geology 261, 199-216.

Deschamps, F., Guillot, S., Godard, M., Chauvel, C., Andreani, M., Hattori, K., 2010. In situ characterization of serpentinites from forearc mantle wedges: Timing of serpentinization and behavior of fluid-mobile elements in subduction zones. Chemical Geology 269, 262-277. http://dx.doi.org/10.1016/j.chemgeo.2009.10.002.

Dick, H.J.B., Bullen, T., 1984. Chromian spinel as a petrogenetic indicator in abyssal and alpine-type peridotites and spatially associated lavas. Contributions to mineralogy and petrology 86, 54-76.

Dick, H.J.B., Natland, J.H., Alt, J.C., Bach,W., Bideau, D., Gee, J.S., Haggas, S., Hertogen, J.G.H., Hirth, G., Holm, P.M., Ildefonse, B., Iturrino, G., John, B.E., Kelley, D.S., Kikawa, E., Kingdon, A., LeRoux, P.J., Maeda, J., Meyer, P.S., Miller, D.J., Naslund, H.R., Niu, Y., Robinson, P.T., Snow, J.E., Stephen, R.A., Trimby, P.W.,Worm, H.-U., Yoshinobu, A., 2000. A long in situ section of the lower ocean crust: results of ODP Leg 176 drilling at the Southwest Indian Ridge. Earth and Planetary Science Letters 179, 31-51.

Dick, H.J.B., Tivey, M.A., Tucholke, B.E., 2008. Plutonic foundation of a slow-spreading ridge segment: Oceanic core complex at Kane Megamullion, 23° 30’N, 45 °20’W. Geochemistry, Geophysics, Geosystems 9, Q05014. doi:10.1029/2007GC001645.

Donnelly, K.E., Goldstein, S.L., Langmuir, C.H., Spiegelman, M., 2004. Origin of enriched ocean ridge basalts and implications for mantle dynamics. Earth and Planetary Science Letters, 226, 347-366.

Drouin, M., Godard, M., Ildefonse, B., Bruguier, O., Garrido, C.J., 2009. Geochemical and petrographic evidence for magmatic impregnation in the oceanic lithosphere at Atlantis Massif,Mid-Atlantic Ridge (IODP Hole U1309D, 30°N). Chemical Geology 264, 71-88.

Elderfield, H. and Greaves, M.J., 1982. The rare earth elements in seawater. Nature 296, 214-219.

Escartín, J., Mével, C., MacLeod, C.J., and McCaig, A.M., 2003, Constraints on deformation conditions and the origin of oceanic detachments: The Mid-Atlantic Ridge core complex at 15°45'N: Geochemistry, Geophysics, Geosystems, v. 4, no. 8, p. 1067, doi:10.1029/2001GC000278.

Escartin, J., Mével, C., Petersen, S., Bonnemains, D., Cannat, M., Andeani, M., Augustin, N., Bezos, A., Chavagnac, V., Choi, Y., Godard, M., Haaga, K., Hamelin, C., Ildefonsa, B., Jamieson, J., John, B., Leleu, T., MacLeod, C.J., Massot-Campos, M., Nomikou, P., Olive, J.A., Paquet, M., Rommevaux, C., Rothenbeck, M., Steinfuhrer, Tominaga, M., Triebe, L., Campos, R., Gracias, N., Garcia, R., 2017. Tectonic structure, evolution, and the nature of oceanic complexes and their detachment zones (13º20′N and 13º30′N, Mid Atlantic Ridge). Geochemistry, geophysics, geosystems. doi: 10.1002/2016GC006775.

Evans, B.W., Frost, B.R., 1975. Chrome-spinel in progressive metamorphism; a preliminary analysis. Geochimica et Cosmochimica Acta, 39, 959-972.

Evans, B.W., Trommsdorff, V., 1970. Regional metamorphism of ultramafic rocks in the Central Alps Paragenesis in the system CaO-MgO-SiO_2-H_2O. Schweiz.Min.Pen.Milt. 50, 481-492.

Ferrando, C., Godard, M., Ildefonse, B., Rampone, E., 2018. Melt transport and mantle assimilation at AtlantisMassif (IODP Site U1309): constraints from geochemical modeling. Lithos 323, 24-43.

Franz, L., Wirth, R., 2000. Spinel inclusions in olivine of peridotite xenoliths from TUBAF seamount (Bismark Archipelago/Papua New Guinea): evidence for the thermal and tectonic evolution of the oceanic lithosphere. Contributions to Mineralogy and Petrology 140, 283-295.

Frisby, C., Bizimis, M., Mallick, S., 2016a. Hf-Nd isotope decoupling in bulk abyssal peridotites due to serpentinization. Chemical Geology 440, 60-72. http://dx.doi.org/10.1016/j.chemgeo.2016.07.006.

Frisby, C., Bizimis, M., Mallick, S., 2016b. Seawater-derived rare earth element addition to abyssal peridotites during serpentinization. Lithos 248-251, 432-454.

Frost, B.R., Beard, J.S., McCaig, A., Condliffe, E., 2008. The formation of micro-rodingites from IODP Hole U1309D: Key in understanding the process of serpentinization. Journal of Petrology 49(9), 1579-1588. http://dx.doi.org/10.1093/petrology/egn038.

Früh-Green, G.L., Connolly, J.A.D., Plas, A., Kelley, D.S., Grobéty, B., 2004. Serpentinization of oceanic peridotites: implications for geochemical cycles and biological activity. In: Wilcock, W.S.D., DeLong, E.F., Kelley, D.S., Baross, J.A., Cary, C. (Eds.), The Subseafloor Biosphere at Mid-Ocean Ridges. Geophysical Monograph. 144, pp. 119-136.

Früh-Green, G.L., Orcutt, B.N., Green, S.L., et al., 2017. Expedition 357 summary. In: Früh- Green, G.L., Orcutt, B.N., Green, S.L., Cotterill, C. (Eds.), Expedition 357 Scientists. Proceedings of the International Ocean Discovery Program 357, College Station, TX. https://doi.org/10.14379/iodp.proc.357.101.2017.

Früh-Green, G.L., Orcutt, B.N., Green, S., Cotterill, C., and the Expedition 357 Scientists, 2016. Expedition 357 Preliminary Report: Atlantis Massif Serpentinization and Life. International Ocean Discovery Program. 10.14379/iodp.pr.357.2016

Früh-Green, G.L., Orcutt, B.N., Rouméjon, S., et al., 2018. Magmatism, serpentinization and life: insights through drilling the Atlantis Massif (IODP Expedition 357). Lithos 323, 137-155. https://doi.org/10.1016/j.lithos.2018.09.012.

Gargiulo, M.F., Bjerg, E.A., Mogessie, A., 2013. Spinel group minerals in metamorphosed ultramafic rocks from Río de Las Tunas belt, Central Andes, Argentina. Geologica Acta 11(2), 133-148. doi : 10.1344 / 105 .000001836.

Grimes, C.B., John, B.E., Cheadle, M.J., Wooden, J.L., 2008. Protracted construction of gabbroic crust at a slow spreading ridge: constraints from 206Pb/238U zircon ages from Atlantis Massif and IODP Hole U1309D (30°N, MAR). Geochemistry, Geophysics, Geosystems 9 Q08012.

Godard, M., Lagabrielle, Y., Alard, O., Harvey, J., 2008. Geochemistry of the highly depleted peridotites drilled at ODP Sites 1272 and 1274 (Fifteen–Twenty Fracture Zone, Mid-Atlantic Ridge): implications for mantle dynamics beneath a slow spreading ridge. Earth and Planetary Science Letters 267 (3-4), 410–425. doi:10.1016/j.epsl.2007.11.058.

Godard, M., Awaji, S., Hansen, H., et al., 2009. Geochemistry of a long in-situ section of intrusive slow-spread oceanic lithosphere: results fromIODP Site U1309 (Atlantis Massif, 30°N Mid-Atlantic-Ridge). Earth and Planetary Science Letters 279, 110-122.

González-Jiminéz, J.M., Kerestedjian, T., Proenza, J.A., Gervilla, F., 2009. Metamorphism on Chromite Ores from the Dobromirtsi Ultramafic Massif, Rhodope Mountains (SE Bulgaria). Geologica Acta 67, 7(4), 413-429. DOI: 10.1344/104.000001447.

Hart, S.R., Zindler, A., 1986. In search of a bulk-earth composition. Chemical Geology 57, 247-267.

Heinrich, K.F.J., 1987. Mass absorption coefficients for electron probe microanalysis. In: Brown, J. Packwood, R. (Eds.), Proceedings of the 11th International Congress on X-Ray Optics and Microanalysis, University of Western Ontario, London, Ontario, Canada 1986, pp. 67-119.

Hellebrand, E., Snow, J.E., Dick, H.J.B., Hofmann, A.W., 2001. Coupled major and trace elements as indicators of the extent of melting in mid-ocean-ridge peridotites. Nature 410, 677-681.

Ildefonse, B., Blackman, D.K., John, B.E., Ohara, Y., Miller, D.J., MacLeod, C.J., 2007. Oceanic core complexes and crustal accretion at slow-speading ridges. Geology 35, 623-626.

Irvine, T.N., 1967. Chromian spinel as a petrogenetic indicator Part 2, petrologic applications. Canadian Journal of Earth Sciences 4, 71-103.

Jagoutz, E., Palme, H., Baddenhausen, H., Blum, K., Cendales, M., Dreibus, G., Spettel, B., Lorenz, V., Vanke, H., 1979. The abundance of major, minor and trace elements in the earth's mantle as derived from primitive ultramafic nodules. Geochimica et Cosmochimica Acta 11 (2), 2031-2050.

Karson, J.A., 2002. Geologic structure of the uppermost oceanic crust created at fast- to intermediate-rate spreading centers. Annual Review of Earth and Planetary Sciences 30, 347–384.

Karson, J.A., Früh-Green, G.L., Kelley, D.S., Williams, E.A., Yoerger, D.R., Jakuba, M., 2006. Detachment shear zone of the Atlantis Massif core complex, Mid-Atlantic Ridge, 30°N. Geochemistry, Geophysics Geosystems 7 (6), Q06016.

Kelemen, P.B., 1990. Reaction between ultramafic rock and fractionating basaltic magma I. Phase relations, the origin of calc-alkaline magma series, and the formation of discordant dunite. Journal of Petrology 31, 51-98.

Kelemen, P.B., Hirth, G., Shimizu, N., Spiegelman, M., Dick, H., 1997. A review of melt migration processes in the adiabatically upwelling mantle beneath oceanic spreading ridges. Philosophical Transactions of the Royal Society of London. Series A355, 283-318.

Kelemen, P., Kikawa, E., Miller, J., Abe, N., Bach,W., Carlson, R.L., Casey, J.F., Chambers, L.M., Cheadle, M., Cipriani, A., Dick, H.J.B., Faul, U., Garces, M., Garrido, C., Gee, J.S., Godard, M., Griffin, D.W., Harvey, J., Ildefonse, B., Iturrino, G.J., Josef, J., Meurer,W.P., Paulick, H., Rosner, M., Schroeder, T., Seyler, M., Takazawa, E. and Mrozewski, S., 2004. Drilling Mantle Peridotite along the Mid-Atlantic Ridge from 14° to 16°N: Sites 1268-1275. Proc. ODP, Initial Reports, 209. Ocean Drilling Program, Texas A&M University, College Station TX 77845-9547, USA. doi:10.2973/odp.proc.ir.209.2004 pp.

Kelemen, P.B., Kikawa, E., Miller, D.J., Shipboard Scientific Party, 2007. Leg 209 summary: processes in a 20-km-thick conductive boundary layer beneath the Mid-Atlantic Ridge, 14°–16°N. In: Kelemen, P.B., Kikawa, E., Miller, D.J. (Eds.), Proceedings of the Ocean Drilling Program, Scientific Results, 209: College Station, TX. Ocean Drilling Program, pp. 1-33.

Kelemen, P.B., Shimizu, N., Salters, V.J.M., 1995. Extraction of mid-ocean-ridge basalt from the upwelling mantle by focused flow of melt in dunite channels. Nature 375, 747-753.

Kelley, D.S., Karson, J.A., Blackman, D.K., Fruh-Green, G.L., Butterfield, D.A., Lilley, M.D., Olson, E.J., Shrenk, M.O., Roe, K.K., Lebon, G.T., Rivizzigno, P., 2001. An off-axis hydrothermal vent field discovered near the Mid-Atlantic Ridge at 30°N. Nature 412, 145-149.

Khalil, K.I., El-Makky, A.M., 2009. Alteration Mechanisms of Chromian-Spinel during Serpentinization at Wadi Sifein Area, Eastern Desert, Egypt. Resource Geology 59(2), 194-211. doi: 10.1111/j.1751-3928.2009.00090.x.

Kimball, K.L. (1990) Effects of hydrothermal alteration on the compositions of chromian spinels. Contributions to Mineralogy and Petrology, 105, 337-346.

Leybourne, M.I., Peter, J.M., Layton-Mathews, D., Volesky, J., Boyle, D.R., 2006. Mobility and fractionation of rare earth elements during supergene weathering and gossan formation and chemical modification of massive sulphide gossan. Geochimica et Cosmochimica Acta 70(5), 1097-1112. https://doi.org/10.1016/j.gca.2005.11.003

Lenoir, X., Garrido, C.J., Bodinier, J.-L., Dautria, J.-M., Gervilla, F., 2001. The recrystallization front of the Ronda peridotite: evidence for melting and thermal erosion of subcontinental lithospheric mantle beneath the Alboran Basin. Journal of Petrology 42, 141-158.

Liebmann, J., Schwarzenbach, E.M., Früh- Green, G.L., Boschi, C., Rouméjon, S., Strauss, H., Wiechert, U., John, T., 2018. Tracking Water- Rock Interaction at the Atlantis Massif (MAR, 30°N) using sulfur geochemistry. Geochemistry, geophysics, geosystems, 19(11), 4561-4583. doi:10.1029/2018GC007813.

Lyubetskaya, T., Korenaga, J., 2007. Chemical composition of Earth's primitive mantle and its variance: 1. Method and resultsJournal of Geophysical Research 12, B03211. doi:10.1029/2005JB004223.

Macdonald, K.C., 1982. Mid-ocean ridges: fine scale tectonic, volcanic and hydrothermal processes within the plate boundary zone. Annual Review of Earth and Planetary Sciences 10, 155-190.

McCaig, A.M., Cliff, R.A., Escartin, J., Fallick, A.E., MacLeod, C.J., 2007. Oceanic detachment faults focus very large volumes of black smoker fluids. Geology 35 (10), 935-938.

McCaig, A.M., Delacour, A., Fallick, A.E., Castelain, T., Früh-Green, G.L., 2010. Fluid circulation and isotopic alteration in and beneath oceanic detachment faults in the Central Atlantic: Implications for the geometry and evolution of high-temperature hydrothermal circulation cells at slow-spreading ridges, In: Diversity of Hydrothermal Systems on Slow Spreading Ocean Ridges. In: Rona, P.A., Devey, C.W., Dyment, J.,Murton, B.J. (Eds.), AGU Geophy. Mono. Series. 188, pp. 207–239.

McDonough, W.F. and Rudnick, R.L., 1998. Mineralogy and composition of the upper mantle. In: Hemley, R.J. (Ed.), Ultrahigh pressure mineralogy: Reviews in Mineralogy, V. 37, Mineralogical Society of America, DeGruyter, pp. 139-164. https://doi.org/10.1515/9781501509179.

McDonough, W.F., Sun, S.S., 1995. The composition of the Earth. Chemical Geology 120, 223-253.

Merlini, A., Grieco, G., Diella, V., 2009. Ferritchromite and chromian-chlorite formation in mélange-hosted Kalkan chromitite (Southern Urals, Russia). American Mineralogist 94, 1459-1467.

Müntener, O., Pettke, T., Desmurs, L., Meier, M., Schaltegger, U., 2004. Refertilization of mantle peridotite in embryonic ocean basins: trace element and Nd isotopic evidence and implications for crust–mantle relationships. Earth and Planetary Science Letters 221, 293-308. doi:10.1016/S0012-821X(04)00073-1.

Niida, K., 1997. Mineralogy of MARK peridotites: replacement through magma channeling examined from 920D, MARK area. In: Karson, J.A., Cannat, M., Miller, D.J., Elthon, D. (Eds.), Proceedings of the Ocean Drilling Program: Scientific Results,153. Ocean Drilling Program, College Station, TX, pp. 265-275.

Niu, Y., 1997. Mantle melting and melt extraction processes beneath ocean ridges: evidence from abyssal peridotites. Journal of Petrology 38, 1047-1074.

Niu, Y., 2004. Bulk rock major and trace element compositions of abyssal peridotites: implications for mantle melting, melt extraction and post-melting processes beneath mid-ocean ridges. Journal of Petrology 45, 2423-2458.

Obata M., Banno, S., Mori, T., 1974. The iron-magnesium partitioning between naturally occurring coexisting olivine and Ca-rich clinopyroxene: an application of the simple mixture model to olivine solid solution. Bull. Soc. Jr. Miner. Crystallogr., 97, 101-107.

O'Hanley, D.S., 1996. Serpentinites Records of Tectonic and Petrological History. Oxford, Oxford University Press, 290 pp.

Palme, H., O'Neill, H.S.C., 2003. Cosmochemical estimates of mantle composition, In: Treatise on Geochemistry, vol. 2, Holland, H., Turekian, K.K., (Eds.), pp. 1-38, Elsevier, New York.

Parnell-Turner, R., Escartín, J., Olive, J.-A., Smith, D.K., and Petersen, S., 2018, Genesis of corrugated fault surfaces by strain localization recorded at oceanic detachments: Earth and Planetary Science Letters, v. 498, p. 116–128, doi: 10.1016/j.epsl.2018.06.034.

Parkinson, I.J., Pearce, J.A., 1998. Peridotites from the Izu–Bonin–Mariana Forearc (ODP Leg 125), evidence for mantle melting and melt–mantle interaction in a suprasubduction zone setting. Journal of Petrology 39, 1577-1618.

Paulick, H., Bach,W., Godard, M., De Hoog, J.C.M., Suhr, G., Harvey, J., 2006. Geochemistry of abyssal peridotites (Mid-Atlantic Ridge, 15°20′N, ODP Leg 209): implications for fluid/rock interaction in slow spreading environments. Chemical Geology 234, 179-210.

Picazo, S., Cannat, M., Delacour, A., Escartin, J., Rouméjon, S., Silantyev, 2012. Deformation associated with the denudation of mantle-derived rocks at the Mid-Atlantic Ridge 13°-15°N: The role of magmatic injections and hydrothermal alteration. Geochemistry, geophysics, geosystems 13(9). https://doi.org/10.1029/2012GC004121

Pouchou, J.-L., Pichoir, F., 1991. Quantitative analysis of homogeneous or stratified microvolumes applying the model "PAP". In: Heinrich, K.F.J., Newbury, D.E. (Eds.), Electron Probe Quantitation Plenum Publishing Corporation, New York, New York, pp. 31-75.

Purvis, A.C., Nesbitt, R.W., Hallberg, J.A., 1972. The geology of the part of the Carr Boyd rocks complex and it's associated nickel mineralization, Western Australia. Economic Geology 67, 1093-1113.

Quick, J.E., 1981. The origin and significance of large, tabular dunite bodies in the Trinity peridotite, northern California. Contributions to Mineralogy and Petrology 78, 413-422.

Rampone, E., Piccardo, G.B.,Vannucci, R., Bottazzi, P., 1997. Chemistry and origin of trapped melts in ophiolitic peridotites. Geochimica et Cosmochimica Acta 61, 4557-4569.

Rampone, E., Piccardo, G.B., Vannucci, R., Bottazzi, P., Zanetti, A., 1994. Melt impregnation in ophiolitic peridotite: an ion microprobe study of clinopyroxene and plagioclase. Mineralogical Magazine 58A, 756-757.

Reed, S.J.B., 1990), Fluorescence effects in quantitative microprobe analysis. In: Williams, D.B., Ingram, P., Michael, J.R. (Eds.), Microbeam Analysis-1990 San Francisco Press, San Francisco, pp. 109-114.

Rouméjon, S., Cannat, M., Agrinier, P., Godard, M., Andreani, M., 2015. Serpentinization and Fluid Pathways in Tectonically Exhumed Peridotites from the Southwest Indian Ridge (62-65 E). Journal of Petrology 56, 703-734.

Rouméjon, S., Früh-Green, G.L., Orcutt, B.N., the IODP Expedition 357 Science Party, 2018a. Alteration heterogeneities in peridotites exhumed on the southern wall of the Atlantis Massif (IODP Expedition 357). Journal of Petrology, 1–29 https://doi.org/10.1093/petrology/egy065.

Rouméjon, S.,Williams, M.J., Früh-Green, G.L., 2018b. In situ oxygen isotope analyses in serpentine minerals: constraints on serpentinization during tectonic exhumation at slow- and ultraslow-spreading ridges. Lithos 323, 156-173. https://doi.org/10.1016/j.lithos.2018.09.021.

Sack R.O., Ghiorso M.S., 1991. Chromian spinels as petrogenetic indicators: thermodynamic and petrological applications. American Mineralogist 76, 827-847.

Säntii, J., Kontinen, A., Sorjonen-Ward, P., Johanson, B., Pakkanen, L., 2006. Metamorphism and Chromite in Serpentinized and Carbonate-Silica-Altered Peridotites of the Paleoproterozoic Outokumpu-Jormua Ophiolite Belt, eastern Finland. International Geology Review 48, 494-546. https://doi.org/10.2747/0020-6814.48.6.494.

Saumur, B.M., Hattori, K. 2013. Zoned Cr-spinel and ferritchromite alteration in forearc mantle serpentinites of the Rio San Juan Complex, Dominican Republic. Mineralogical Magazine 77(1), 117-136. DOI: 10.1180/minmag.2013.077.1.11.

Schroeder, T., John, B.E., 2004. Strain localization on an oceanic detachment fault system, Atlantis Massif, 30° N, Mid-Atlantic Ridge. Geochemistry, Geophysics, Geosystems 5.

Schroeder, T., John, B.E., and Frost, B.R., 2002, Geologic implications of seawater circulation through peridotite exposed at slow-spreading mid-ocean ridges, Geology, v. 40, p. 367-370.

Shibata T., Thompson, G. 1986. Peridotites from the mid-Atlantic ridge at 43 °N and their petrogenetic relation to abyssal tholeiites. Contribution to Mineralogy and Petrology 93, 144-159.

Snow, J.E., Dick, H.J.B., 1995. Pervasive magnesium loss by marine weathering of peridotite. Geochimica et Cosmochimica Acta 59 (20), 4219-4235.

Spangenberg, K., 1943. Die Chromitlagerstatte von Tampadel am Zobten. Zeitschrift fur Praktische Geologie 51, 13-35.

Springer, G., 1971. Fluorescence by the X-ray continuum in multi-element targets: Falconbridge Nickel Mines Limited, Thornhill, Ontario, Canada, Report FRL-138, 14 p.

Starr, P., 2017. Sub-Greenschist to Lower Amphibolite Facies Metamorphism of Basalts: Examples from Flin Flon, Manitoba and Rossland, British Columbia. Ph.D. thesis, University of Calgary, 495 pp.

Stevens, R.E., 1944. Composition of some chromites of the Western hemisphere. American Mineralogist 29, 1-34.

Stewart, M.A., Karson, J.A., Klein, E.M., 2005. Four-dimensional upper crustal construction at fast-spreading mid-ocean ridges: a perspective from an upper crustal cross-section at the Hess Deep Rift. Journal of Volcanology and Geothermal Research 144, 287-309.

Su, Y., 2003. Global MORB chemistry compilation at the segment scale. Ph.D. Thesis. New York, Columbia University.

Suita, M.T., Streider, A.J., 1996. Cr-Spinels from Brazilian mafic - ultramafic complexes: metamorphic modifications. International Geology Review 38, 245-267.

Suhr, G., Hellebrand, E., Johnson, K., Brunelli, D., 2008. Stacked gabbro units and intervening mantle: a detailed look at a section of IODP Leg 305, Hole U1309D. Geochemistry, Geophysics, Geosystems 9. https://doi.org/10.1029/2008GC002012.

Suhr, G., Hellebrand, E., Snow, J.E., Seck, H.A., Hofmann, A.W., 2003. Significance of large, refractory dunite bodies in the upper mantle of the Bay of Islands Ophiolite. Geochemistry, Geophysics, Geosystems 4, 8605. doi:10.1029/2001GC000277.

Takazawa, E., Frey, F.A., Shimuzu, N., Obata, M., Bodinier, J.L., 1992. Geochemical evidence for melt migration and reaction in the upper mantle. Nature 359, 55-58.

Tucholke, B.E., Lin, J., Kleinrock, M.C., 1998. Megamullions and mullion structure defining oceanic metamorphic core complexes on the Mid-Atlantic Ridge. Journal of Geophysical Research 103, 9857-9866.

Van der Wal, D., Bodinier, J.-L., 1996. Origin of the recrystallisation front in the Ronda peridotite by km-scale pervasive porous melt flow. Contributions to Mineralogy and Petrology 122, 387-405.

Verlaguet, A., Bonnemains, D., Mével, C., Escartín, J., Andreani, M., Bourdelle, F., Boiron, M. - C., Chavagnac, V., 2021. Fluid circulation along an oceanic detachment fault: Insights from fluid inclusions in silicified brecciated fault rocks (Mid- Atlantic Ridge at 13°20′N). Geochemistry, geophysics, geosystems 22(1), 1–32. doi: 10.1029/2020GC009235.

Whattam, S.A., Cho, M., Smith, I.E.M., 2011. Magmatic peridotites and pyroxenites, Andong Ultramafic Complex, Korea: Geochemical evidence for supra-subduction zone formation and extensive melt–rock interaction. Lithos 127, 599-618.

Workman, R.K., Hart, S.R., 2005. Major and trace element composition of the depleted MORB mantle (DMM), Earth and Planetary Science Letters 231, 53–-72.

Zervas, C.E., Sempéré, J.-C., Lin, J., 1995. Morphology and crustal structure of a small transform fault along theMid-Atlantic Ridge: the Atlantis Fracture Zone. Marine Geophysical Researches 17, 275-300. https://doi.org/10.1007/BF01203466.

Geochemistry of serpentinized and multiphase altered Atlantis Massif peridotites (IODP Expedition 357): Petrogenesis and discrimination of melt-rock vs. fluid-rock processes

Scott A. Whattam[a*], Gretchen L. Früh-Green[b], Mathilde Cannat[c], Jan C. M. De Hoog[d], Esther M. Schwarzenbach[e], Javier Escartin[f], Barbara E. John[g], Mathew I. Leybourne[h], Morgan J. Williams[i], Stéphane Rouméjon[b], Norikatsu Akizawa[j], Chiara Boschi[k], Michelle Harris[l], Kirsten Wenzel[m], Andrew McCaig[n], Dominique Weis[o], Laura Bilenker[p]

[a]*Department of Geosciences, King Fahd University of Petroleum and Minerals, Dhahran, 31261, Saudi Arabia*

[b]*Institute of Geochemistry and Petrology, ETH Zurich, Clausiusstrasse 25, 8092 Zürich, Switzerland*

[c]*Institut de Physique du Globe de Paris, CNRS, 1 rue Jussieu, 75238 Paris, Cedex 05, France*

[d]*School of Geosciences, Grant Institute, The University of Edinburgh, James Hutton Road, EH9 3FE, United Kingdom*

[e]*Institute of Geological Sciences, Freie Universität Berlin, Malteserstrasse 74-100, 12249 Berlin, Germany*

[f]*Laboratoire de Géologie – CNRS, UMR 8538, École Normale Supérieure, PSL University, Paris, France*

[g]*Department of Geology and Geophysics, University of Wyoming, Laramie, WY 82071*

[h]*Queen's Facility for Isotope Research, Department of Geological Sciences and Geological Engineering, and Arthur B. McDonald Canadian Astroparticle Physics Research Institute, Department of Physics, Engineering Physics & Astronomy, Queen's University, Kingston, ON, Canada, K7L 3N6*

[i]*CSIRO Mineral Resources, 26 Dick Perry Avenue, Kensington WA 6151, Australia*

[j]*Kanazawa University, Department of Earth Sciences, Kakuma Kanazawa, Ishikawa 920-1192, Japan*

[k]*Institute of Geosciences and Earth Resources – CNR, Via Moruzzi 1, 56124 Pisa, Italy*

[l]*School of Geography, Earth and Environmental Sciences, 109 Fitzroy Building, Plymouth University, Plymouth PL4 8AA, United Kingdom.*

[m]*GeoZentrum Nordbayern, Friedrich-Alexander-University Erlangen-Nuremberg, Schlossgarten 5a, 91054 Erlangen, Germany*

[n]*School of Earth and Environment, Leeds University, Woodhouse, Leeds LS2 9JT, United Kingdom*

[o]*Pacific Centre for Isotopic and Geochemical Research, Earth, Ocean and Atmospheric Sciences, University of British Columbia, Earth, Ocean and Atmospheric Sciences, 2020-2207 Main Mall, Vancouver BC V6T-1Z4, Canada*
[p]*Deparment of Geosciences, Auburn University, Auburn, AL 36849*

[*]Corresponding author: Scott A. Whattam
E-mail address: sawhatta@gmail.com

Abstract

International Ocean Discovery Program (IODP) Expedition 357 drilled 17 shallow sites distributed ~ 10 km in the spreading direction (from west to east) across the Atlantis Massif oceanic core complex (Mid-Atlantic Ridge, 30 ºN). Mantle exposed in the footwall of the Atlantis Massif oceanic core complex is predominantly nearly wholly serpentinized harzburgite with subordinate dunite. Altered peridotites are subdivided into three types: (I) serpentinites, (II) melt-impregnated serpentinites, and (III) metasomatic serpentinites. Type I serpentinites show no evidence of melt-impregnation or metasomatism apart from serpentinization and local oxidation. Type II serpentinites have been intruded by gabbroic melts and are distinguishable in some cases on the basis of macroscopic and microscopic observations, e.g., mm-cm scale mafic-melt veinlets, rare plagioclase (<0.5 modal % in one sample) or by the local presence of secondary (replacive) olivine after orthopyroxene; in other cases, 'cryptic' melt-impregnation is inferred on the basis of incompatible element enrichments. Type III serpentinites are characterized by silica metasomatism manifested by alteration of orthopyroxene to talc and amphibole, and by anomalously high anhydrous SiO_2 concentrations (59-61 wt.%) and low MgO/SiO_2 values (0.48-0.52). Although many chondrite-normalized rare earth element (REE) and primitive mantle-normalized incompatible trace element anomalies, e.g., negative Ce-anomalies, are attributable to serpentinization, other compositional heterogeneities are due to melt-impregnation. On the basis of whole rock incompatible trace elements, a dominant mechanism of melt-impregnation is distinguished in the central and eastern serpentinites from fluid-rock alteration (mostly serpentinization) in the western serpentinites, with increasing melt-impregnation manifest as a west to east increase in enrichment in high-field strength elements and light REE. High degrees of melt extraction are evident in low whole-rock Al_2O_3/SiO_2 values and low concentrations of Al_2O_3, CaO and incompatible elements. Estimates of the degree of melt extraction based on whole rock REE patterns suggest a maximum of ~ 20 % non-modal fractional melting, with little variation between sites. As some serpentinite samples are *ex situ* rubble, the magmatic histories observed at each site are consistent with a local source (from the fault zone) rather than rafted rubble that would be expected to show more heterogeneity and no spatial pattern. In this case, the studied sites may provide a record of enhanced melt-rock interactions with time, consistent with proposed geological models. Alternatively, sites may signify heterogeneities in these processes at spatial scales of a few km.

Keywords: IODP Expedition 357; Atlantis Massif; mantle peridotite; fluid-rock interaction; melt-rock interaction

1. Introduction

Spreading rate exerts a profound influence on the geometry and architecture of the oceanic crust. Slow-spreading ridges (≤ 5 cm/year), as exemplified by the Mid-Atlantic ridge (MAR), are characterized by wide (up to 30 km) and deep (1–2 km) axial valleys bounded by uplifted shoulders and transient magma reserves. In contrast, fast-spreading ridges (≥ 9 cm/year), as characterized by the East Pacific Rise, exhibit much narrower to absent axial troughs (a few hundred meters wide) and a more continuous magma supply (e.g., Macdonald, 1982; Karson, 2002; Stewart et al., 2005). Analogous with ‘metamorphic core complexes’ found in extended continental regions (e.g., John, 1987), ‘oceanic core complexes’ (OCCs), such as the Atlantis Massif (30 °N, Fig. 1a) along the MAR, represent segments of a slow spreading ridge comprised of elevated seafloor massifs that display flat or gently curved upper surfaces with prominent corrugations or ‘megamullions’ (Escartin et al., 2017; Tucholke et al., 1998). OCCs comprise segments of lower crustal and upper mantle rocks exposed at the seafloor (Cann et al., 1997; Blackman et al., 1998; Tucholke et al., 1998) and represent uplifted footwalls of large-offset low-angle normal faults, commonly referred to as detachment faults. Mantle rocks of OCCs characteristically comprise olivine-rich peridotite (i.e., harzburgite, dunite) that interacted with seawater to produce serpentinite over a range of temperatures (Andreani et al., 2007; Blackman et al., 1998; Boschi et al., 2006a; Boschi et al., 2006b; Cann et al., 1997; Cannat, 1993; Früh-Green et al., 2004; Karson et al., 2006; Kelemen et al., 2007; Rouméjon et al., 2015; Rouméjon et al., 2018a; Schroeder et al, 2002).

Four OCCs have been drilled by the Ocean Drilling Program (ODP), the Integrated Ocean Drilling Program (IODP) and the International Ocean Discovery Program (IODP). The Atlantis Massif is one of the best studied and well-known OCC as it hosts the off-axis, peridotite-hosted Lost City hydrothermal field (Kelley et al., 2001) on its southern wall (Fig. 1b). Other drilled OCCs include the Atlantis Bank, SW Indian Ridge (ODP Hole 735B, Dick et al., 2000), the MARK (Mid-Atlantic Ridge Kane fracture zone) at 23°32′ N (ODP Leg 153, Sites 921–924, Cannat et al., 1995), and an OCC on the MAR at 15°44′ N (ODP Leg 209, Site 1275, Kelemen et al., 2004). The Atlantis Massif (30 °N, Fig. 1a) was drilled during IODP Expeditions 304/305 (Blackman et al., 2006), at Site U1309 and Expedition 357 (Früh-Green et al., 2017, 2018; Roumejon et al., 2018a, 2018b; Akizawa et al., 2020).

Research on detachment faulting at OCCs implies that oceanic spreading is closely linked to the development of hydrothermal circulation patterns and encompasses a wide variety of fluid flow and hydrothermal regimes (McCaig et al., 2007; Escartin et al., 2008). High-temperature fluid circulation both within the footwall and along the fault zone is well documented on the basis of mineralogy and geochemistry (Schroeder and John, 2004; Boschi et al., 2006a; McCaig et al., 2010, Picazo et al., 2012, Verlaguet et al., 2021). Importantly, uplift along detachment faults appears to promote circulation and alteration within the footwall. Several studies propose a temporal evolution in the style of hydrothermal circulation associated with OCC formation. High-temperature systems are hosted in the basaltic hanging wall within the rift valley, whereas high-temperature ultramafic-hosted systems occur within the OCC footwall. Ultimately, hydrothermal circulation transitions to off-axis ultramafic-hosted systems within the footwall (Andreani et al., 2007; McCaig et al., 2007; Fouquet et al., 2010). In ultramafic and mafic systems, metasomatic assemblages of talc-tremolite-chlorite or quartz form at > 350 °C (Boschi et al., 2006a, 2008; McCaig et al., 2010; Verlaguet et al., 2021), typical of black smoker discharge zones, whereas serpentine-prehnite-hydrogarnet assemblages form at lower temperatures (Frost et al., 2008; Bach and Klein, 2009).

Cores recovered during IODP Expedition 357 have highly heterogeneous rock types, and are variably altered and deformed. Ultramafic rocks are dominated by serpentinized harzburgite with intervals of serpentinized dunite and minor pyroxenite veins; gabbroic layers occur as melt impregnations and veins. Dolerite dikes and basalts are the latest phase of magmatism. Overall, the peridotites show a high degree of serpentinization (> 80 %) and are locally oxidized. In cores with gabbroic intrusions, hydrothermal alteration of mixed peridotite and gabbroic lithologies forms serpentine-talc-amphibole-chlorite assemblages (Boschi et al., 2006b; Picazo et al., 2012).

The petrogenesis of mantle-derived peridotites recovered during IODP Expedition 357 is the subject of this communication. In this paper we use whole rock major, trace and rare earth element (REE) chemistry of Expedition 357 peridotites to discriminate dominant melt-impregnation vs. fluid-dominated processes (i.e., serpentinization, Si metasomatism) and constrain the degrees of partial melting recorded in the peridotites. The altered peridotites are subdivided into Type I serpentinites, Type II melt-impregnated serpentinites and Type III metasomatic serpentinites. Type I serpentinites show no evidence of melt-impregnation or metasomatism apart from serpentinization and local oxidation. Type II serpentinites are distinguishable in some cases on the basis of macroscopic or microscopic evidence and in other cases, are inferred on the basis of incompatible element enrichment in the case of ‘cryptically’ melt-impregnated serpentinites. Type III serpentinites are characterized by silica metasomatism and the formation of talc-rich alteration assemblages and anomalously high anhydrous SiO_2 concentrations and low MgO/SiO_2 values. In so doing, we geochemically characterize the evolution of mantle lithosphere at a slow-spreading ridge associated with OCC formation, and document spatial compositional variations.

2. Geological setting

The dome-shaped Atlantis Massif OCC is located at 30 °N on the western edge of the MAR axial valley where it intersects the Atlantis Fracture Zone (Fig. 1b). The OCC stretches 15-20 km N–S parallel to the ridge and is 8-12 km wide. Exhumation occurred via low-angle detachment faulting (Cann et al., 1997; Blackman et al., 2002; Schroeder and John, 2004; Karson et al., 2006; Ildefonse et al., 2007). On the basis of its distance from the spreading axis and a calculated spreading half-rate of 12 mm/yr (Zervas et al., 1995), the lithosphere of the massif is considered to be 2.0 to 0.5 Ma (Blackman et al., 2006), a span which encompasses eighteen SHRIMP U/Pb zircon ages of oxide gabbro and felsic dike melt intrusions recovered from Hole U1309D, which range from 1.28 ± 0.05 to 1.08 ± 0.07 Ma (Grimes et al., 2008). Dredging and submersible dives at the massif revealed the dominance of serpentinized peridotite (Blackman et al., 2002; Boschi et al., 2006a; Karson et al., 2006) concentrated primarily along the southern and most elevated portion of the detachment. Samples recovered during IODP Expeditions 304/305, with a drill hole reaching ~ 1500 m depth, consisted almost entirely of olivine-rich mafic intrusive rocks of gabbro and troctolite (Drouin et al., 2009; Ferrando et al., 2018; Godard et al., 2009; Suhr et al., 2008). These geological observations suggest a compositional change of the footwall, with peridotites decreasing in abundance from the segment end towards the north, and also reflecting variations in time of the emplacement of magma in the footwall (Ildefonse et al., 2007).

IODP Expedition 357 cored seventeen shallow holes at nine sites (Fig. 1b) along the detachment fault surface of the Atlantis Massif (Früh-Green et al., 2016). The two eastern sites (M0075, M0068) and one western site (M0071) recovered fault scarp deposits whereas the central sites yielded *in situ* sequences. Most of the sites are aligned along the southern edge of the detachment fault by the Atlantis Fracture Zone wall, with the northernmost hole (M0074) located ~ 6 km north of the detachment's southern edge, and ~ 1 km to the southwest of U1309D. In terms of igneous lithologies and their metamorphosed equivalents, IODP Expedition 357 recovered primarily serpentinized peridotite comprising harzburgite with subordinate dunite (Fig. 1c) and wehrlite with lesser amounts of variably altered mafic inclusions of basalt, gabbro and dolerite (Früh-Green et al., 2018; Rouméjon et al., 2018a; Akizawa et al., 2020). Core lengths range from approximately 1.3 to 16.5 m. Recovery was ~ 75 %.

3. Samples and petrography

Except for one talc schist, the protolith of which was mafic, all rocks chosen for study are serpentinized peridotites, and from holes immediately adjacent to the transform fault scarp and drilled at the southern edge of the detachment fault surface (Figs. 1b, c). All peridotites were subjected to high degrees of serpentinization on the order of > 80 %. On the basis of collective macroscopic, microscopic and whole rock chemistry evidence, the studied samples are divided into three types: Type I are serpentinites, Type II are melt-impregnated serpentinites, and Type III are metasomatic serpentinites. Type I serpentinites are ones primarily subjected to serpentinization only, and Types II and III serpentinites have been subjected to mm- to cm-scale mafic melt intrusions and subsequent silica metasomatism, respectively. In the case of melt-impregnation, this is evident in Type II serpentinites by the presence of small veinlets of dolerite (as reported in Expedition 357 petrology logs), and in one case by the presence of rare plagioclase and in another case, by the presence of recrystallized olivine along the peripheries of partially dissolved orthopyroxene (see Fig. 2). Further details regarding evidence for classification of Types II and III are provided in Table 1.

All samples were studied by polarization microscopy. Representative thin section images are given in Figure 2. Sample numbers are taken directly from Früh-Green et al. (2017, Supplementary material). Below, we describe the petrography of each sample type. The mineralogy and mode of the serpentinites are summarized in Table 2.

3.1. Type I serpentinites

Type I serpentinites (Fig. 2a-d) consist of dominant harzburgite (14 of 20 samples) and lesser dunite. Outlines of olivine are generally clear under plane-polarized light (PPL) as serpentinization is most intense around grain boundaries and fractures cutting olivine (e.g., Fig. 2a). Classic mesh-textures are commonly observed. In the harzburgite, orthopyroxene is always altered to bastite, but is nonetheless recognizable under crossed polars by remnant and deformed (curved) cleavage and parallel extinction. Orthopyroxene is typically < 2 mm and olivine is 2-4 mm. Reddish-orange to brown spinel is easily identifiable under PPL and is typically less than 0.5 mm but in some cases up to 4 mm. Spinel occurs both as isolated, angular grains and as subangular and rounded grains commonly arranged in masses or trails of multiple grains. Clinopyroxene was not observed in any samples, reflecting the high degrees of partial melting and melt extraction that many of these peridotites have undergone (see Fig. 3). Modal percentages of the volumetrically dominant harzburgite lie in the range of 75-90 % for olivine and 10-25 % for orthopyroxene; spinel ranges from 0-3 % (Table 2). In the dunite, orthopyroxene is absent and spinel is less common (0 to <1 %) than in the harzburgite.

Four Type I serpentinites exhibit anomalously high CaO contents ranging from 6-13 wt.% (see Table 3). Microscopic inspection reveals that the Ca-rich peridotites exhibit an extensive and densely concentrated, anastomosing network of ~ 0.1 mm thick carbonate veinlets (Fig. 2d).

3.2. Type II Melt-impregnated serpentinites

Melt-impregnated serpentinites consist of harzburgite only and comprise six of the 29 studied samples (Table 1). Type II serpentinites in most cases are observed to have mm to cm-scale mafic veins at the scale of drill core (Table 2) although these are not obvious in thin section. Orthopyroxene ranges from ~ 1-5 mm. Modal percentages of olivine and orthopyroxene are 70-90 % and 10-30 %, respectively, with spinel typically absent but reaching 2-3 % in one sample (Table 2).

In some Type II serpentinites, other petrographic evidence is present to confirm melt-impregnation. For example, one central harzburgite (76B-7R1-81-83) is the only one in which rare 0.5-0.7 mm plagioclase (< 0.5 % of the mode) is present (Fig. 2e). Plagioclase is highly altered (epidote, sericite) but preserves relict twinning. In another harzburgite from eastern Site M0068B, fresh, 0.5-1 mm olivine constitutes ~ 5 % of the mode, and is observed mantling orthopyroxene (Fig. 2f), which we interpret as replacive following dissolution of orthopyroxene accompanying melt injection.

3.3. Type III Metasomatic serpentinites

Type III serpentinites from this study include two harzburgites that are restricted to the eastern sites (Fig. 1c), and are distinguishable on the basis of talc-amphibole alteration of orthopyroxene (Fig. 2e) and whole rock chemistry (see Section 5.1). Orthopyroxene ranges from 1-6 mm. Brown spinel ranges from 0.5-2 mm and are always embedded in orthopyroxene. Modal percentages of olivine and orthopyroxene are ~ 70 % and 30 % respectively, with spinel occupying around 2 % (Table 2).

4. Analytical methods and data compilation

4.1. Whole rock geochemistry

Major and trace element contents of the serpentinites were determined by inductively coupled plasma mass spectrometry (ICP-MS) and atomic emission spectroscopy (ICP-AES) at ALS Geochemistry, North Vancouver, Canada. Prior to shipping to ALS, samples for whole-rock analysis were trimmed to remove weathered surfaces. Samples sent to ALS were crushed to > 70 % passing through a 2 mm mesh, and a 250-g split was pulverized to > 85 % of the material being < 75 µm in diameter. Powders were then analyzed for whole rock major and trace element determinations. For major element oxides, 100 mg of powered sample was added to lithium metaborate/lithium tetraborate flux, mixed well and fused in a furnace at 1000 °C. The resulting melt was dissolved in 100 mL of 4 % HNO_3/2 % HCl. This solution was then analyzed by ICP-AES (ALS Geochemistry method ME-ICP06) and the results were corrected for spectral inter-element interferences. Major element detection limits are 0.01% for all oxides except Cr_2O_3, which is 0.002 % (Supplementary Table S1). For loss on ignition (LOI), 1 g of sample powder was heated at 1000° C for one hour, cooled and then reweighed, with percent LOI calculated by the difference in weight.

For trace and rare earth elements, the ME-MS61L Super Trace and MS61L-REE methods (https://www.alsglobal.com/) were employed, which combines a four-acid digestion with ICP-MS instrumentation utilizing collision/reaction cell technologies to provide the lowest detection limits available. In the first method, analyzed elements include Ba, Cd, Ce, Co, Cr, Cs, Cu, Ga, Hf, La, Li, Mo, Nb, Ni, Pb, Rb, Sc, Sn, Sr, Ta, Te, Th, U, V, W, Zn and Zr; in the second method, analyzed elements include Dy, Er, Eu, Gd, Ho, Lu, Nd, Pr, Sm, Tb, Tm and Yb. This trace method has been optimized for long-term robust ICP-MS signal stability, in particular for samples with high Ca content. The prepared samples (nominal weight 0.25 g) were digested with 1.5 mL concentrated HNO_3

and $HClO_4$, followed by concentrated HF. Subsequently, the mixture was heated at 185 °C until incipient dryness, leached with 50 % HCl and diluted with weak HCl. The final solution was then analyzed by ICP-MS with results corrected for spectral inter-element interferences. Apart from Ba, Cr, Sn, V, W and Zr with detection limits that range from 0.3-5 µg/g, detection limits of the remaining trace elements ranged from 0.001-0.2 µg/g (Supplementary Table S1).

Results of duplicate analyses and analytical standards used are provided in Supplementary Table S2. Reproducibility of these reference samples is generally better than 5 % for concentrations more than 10 x above the detection limit, and typically 5-20 % closer to the detection limit.

4.2. Data compilation

The stratigraphic location of samples analyzed for whole rock chemistry in this study are shown in Fig. 1c. The new whole rock geochemical data of 29 whole rock ICP-MS and ICP-AES geochemical analyses from this study (Table 3) are compared with the ten Expedition 357 peridotite samples of Früh-Green et al. (2018) and the four Atlantis Massif peridotite samples of Godard et al. (2009) from Site 1309 in Figs. 3-10. We also compare these data with whole rock geochemical data compiled from global abyssal peridotites of Niu (2004), Paulick et al. (2006), and Godard et al. (2008).

5. Results

5.1. Whole rock chemistry major elements and Ni and Cr abundances

In MgO/SiO_2 vs. Al_2O_3/SiO_2 space (Fig. 3) the 'terrestrial array' represents the successive magmatic depletion (or melt extraction) trend of primitive mantle. Highly depleted compositions are characterized by low Al_2O_3/SiO_2 of < 0.01 (Jagoutz et al., 1979; Hart and Zindler, 1986). Verification of this melt extraction trend is reflected by a global data set of MOR peridotites (compilation of Niu, 2004; Paulick et al., 2006; Godard et al., 2008). Atlantis Massif serpentinized harzburgites record Al_2O_3/SiO_2 that range from ~ 0.01-0.04 indicating moderate to high degrees of magmatic depletion. Two Type I serpentinized dunites from the central sites (M0076B-3R1-78-82, M0076B-5R1-59-61, Table 1), and one dunite (1309D-31R-25-28) from Site U1309 reported by Godard et al. (2009) exhibit Al_2O_3/SiO_2 < 0.01. Very low Al_2O_3/SiO_2 values can alternatively be caused by replacive melt-rock interaction. Vertical deviations from the terrestrial array are indicative of Mg-Si mass transfer; peridotites that exhibit MgO/SiO_2 below the terrestrial array may reflect magnesium loss or silica addition during serpentinization or magnesium loss during seafloor weathering (Snow and Dick, 1995; Niu, 2004). A trend defined by increasing Al_2O_3/SiO_2 with most samples offset to moderately low MgO/SiO_2, as seen in the Atlantis Massif serpentinites (Fig. 3), can also be partially attributed to melt-impregnation processes (Niu, 2004). Half of the eight Type II melt-impregnated serpentinites of the eastern and central sites from this study and the study of Früh-Green et al. (2018) exhibit MgO/SiO_2 of < 0.9, consistent with this process; nonetheless, all melt-impregnated serpentinites plot within the range of the Type I serpentinites. Two central serpentinites yield MgO/SiO_2 values of ~ 0.76-0.86, within the lower range of the melt-impregnated serpentinites, which suggests that these two samples may also have been subjected to processes associated with melt-impregnation. Silica-metasomatism is characterized by low MgO/SiO_2 (< 0.55) and low Al_2O_3/SiO_2 (< 0.025). One exception is the talc schist, which exhibits low MgO/SiO_2 (~ 0.4) but high Al_2O_3/SiO_2 of 0.11, which suggests the addition of silicic melt (Paulick et al., 2006).

In Fig. 4 we plot MgO vs. selected major element oxides and loss on ignition (LOI) to illustrate the effects of serpentinization and multiphase alteration processes on major element chemistry. In terms of MgO and other major element oxides, the Type I serpentinites generally plot similarly to global MOR peridotites. Apart from two serpentinized harzburgites, which exhibit anomalously high Al_2O_3 and CaO, the remaining serpentinites have MgO contents that ranges from 41.25 to 46.06 wt.% and Mg# ($Mg/Mg+Fe^{2+}$) of 87.6-91.8 (Table 3). In SiO_2 vs. MgO space (Fig. 4a) the serpentinites and melt-impregnated serpentinites fall almost completely within the range of global abyssal peridotite and plot similarly to, but with slightly lower SiO_2 contents than the bulk composition of serpentine. In contrast, the Type III talc-altered serpentinites and talc schists plot near the bulk composition of talc and ODP Leg 209 talc-altered peridotites, but with slightly lower SiO_2 and MgO. The Ca-rich Type I serpentinites (6.66-13.30 wt.% CaO) plot off the linear array of the serpentinites and melt-impregnated peridotites in SiO_2 vs. MgO space with significantly lower SiO_2 at similar MgO. Fe_2O_3, Al_2O_3 and CaO contents (Figs. 4b-d) of the talc-altered serpentinites and talc schists generally fall within the range of the Type I and II serpentinites. Apart from two Type II melt-impregnated serpentinized harzburgites, which exhibit slightly higher Al_2O_3 contents than the remaining serpentinites, other major element oxide concentrations of the melt-impregnated serpentinites are similar to those of the serpentinites. CaO contents in the western site Type I serpentinites (Fig. 4d) record lower concentrations (0.05-0.30 wt.%) than those of the central and eastern sites. Similar to the SiO_2 vs. MgO plot, significant differences exist in LOI values between the Ca-rich serpentinites and all other serpentinites (Fig. 4e). Whereas the bulk of the peridotites exhibit LOI of ~ 12-14 wt.%, similar to those of global MOR peridotites and the talc-altered harzburgites and schists have low LOI contents that range from ~ 4-6 wt.%, similar to ODP Leg 209 talc-altered peridotites, the Ca-rich serpentinites have high LOI of ~ 16-20 wt.%. The Type II melt-impregnated serpentinites have LOI values that are up to ~ 9 wt.%, intermediate between those of the Type I and serpentinites and Type III serpentinites and schists.

The majority of the Expedition 357 serpentinites have Ni and Cr concentrations of ~ 1000-3000 µg/g (Table 3), similar to that of primitive mantle (PM), and fall within the range of global MOR peridotites (Supplementary Fig. S1). Exceptions are two central and two western serpentinite samples from Früh-Green et al. (2018), which range to Ni > 10000 µg/g and Cr > 30000 µg/g, and two central serpentinized dunites and two eastern melt-impregnated harzburgites from our study, which exhibit low Cr (< 400 µg/g).

5.2. Whole rock trace element concentrations

Significant differences in the relative degree of depletion, pattern morphology, and the existence of prominent element anomalies, e.g., conspicuous positive or Ce-anomalies depending on serpentinite type, are apparent on the basis of chondrite-normalized REE and PM-normalized incompatible trace element patterns (Fig. 5). Patterns range from those similar to and significantly more depleted than depleted MORB mantle (DMM) and mean abyssal peridotite in western Site M0071, central Sites M0069 and M0076, and Atlantis Massif IODP Site U1309 (Godard et al., 2009) to patterns enriched relative to DMM and mean abyssal peridotite as shown by central Site M0072 and most of eastern Site M0068. The serpentinites from eastern Site M0068 are atypical to other Expedition 357 serpentinites in that they exhibit LREE enrichments but HREE concentrations intermediate to that of DMM and mean abyssal peridotite. Central Site M0072 and eastern Site M0068 serpentinites typically exhibit REE concentrations that are more enriched than DMM and range from ~ 1-10 x chondrite; two M0068 talc schists are exhibit high REE concentrations of ~ 20 x chondrite.

Type I serpentinites sampled at western Site M0071, and central Sites M0069 and M0076 exhibit low Yb as well as low abundances of other incompatible elements, for example the high-field strength elements (HFSE) Nb and Zr (Table 3). Apart from one central Site M0072 serpentinized dunite with similarly low Yb, Nb and Zr, the remaining central Site M0072 and eastern site serpentinites, many of which are Type II melt-impregnated or Type III metasomatic serpentinites, exhibit comparatively higher concentrations of these incompatible elements (Table 1). As we show in Section 6.2.3, the melt-impregnated serpentinites, in particular in central Site M0072 and eastern Site M0068, show high concentrations of most incompatible elements relative to other sites.

Although the highly depleted Type I serpentinites from the western and central sites exhibit mostly concave upwards REE patterns with a steady decrease in REE abundances from the HREE to LREE, central Site M0072 Type I and Type II serpentinites exhibit flatter patterns; the eastern Types I, II and III serpentinites are atypical relative to the serpentinites to the west (i.e., at the central and western sites) in that they exhibit LREE enrichment. Excluding the lone, Ca-rich (12.46 wt.% CaO) serpentinized dunite with La/Sm_{CN} (CN denotes chondrite-normalized) of 4.70 and La/Yb_{CN} of 2.39, the western Type I serpentinites from Site M0071 exhibit mostly moderate but variable LREE/MREE fractionation (La/Sm_{CN} of 0.40-3.03) with La/Yb_{CN} ranging from 0.11-0.68. In contrast, the two eastern Type I serpentinites exhibit relatively minor LREE enrichment with La/Sm_{CN} and La/Yb_{CN} ranging from 1.08-1.17 and 1.13-1.30, respectively; the eastern Type II melt-impregnated serpentinites have higher LREE enrichments with La/Sm_{CN} = 1.72-2.15 and La/Yb_{CN} = 1.43-1.68 and the Type III metasomatic serpentinites have $LaSm_{CN}$ = 0.41-1.41 and La/Yb_{CN} = 0.48-1.36.

6. Discussion

On the basis of trace and rare earth element chemistry, we address differences in the compositions of the different serpentinite types to discriminate dominant fluid-rock interaction processes associated with serpentinization, from processes associated with mafic melt-rock interaction. We then provide estimates of degrees of partial melting (melt extraction) recorded in serpentinites sampled across the Atlantis Massif (IODP Exp. 357), before linking the geochemistry to processes associated with oceanic core complex formation.

6.1. Evidence of fluid-dominated serpentinization processes

Significant observations from the chondrite-normalized REE and PM-normalized patterns are: (1) prominent negative Ce-anomalies (i.e., Ce/Ce* where $Ce^* = \sqrt{(La_{CN} * Pr_{CN})}$ and $Ce = Ce_{CN}$) in the western Type I serpentinites and two central Type I serpentinites, and positive Ce-anomalies in almost all eastern serpentinites (the vast majority of other central serpentinites show Ce/Ce* ~ 1); (2) extreme U-enrichment in many serpentinites with values that range to nearly 300 x PM; and (3) extreme Sr-anomalies with enrichments of up 100 x PM in most Ca-rich Type I serpentinites and depletion to below 0.1 x PM in the serpentinites of Sites M0072 and M0068.

With respect to the negative Ce-anomalies exhibited mostly by the western Type I serpentinites (site M0071), such anomalies in peridotites have been attributed to seawater-peridotite interaction (e.g., Frisby et al., 2016a, b) and indeed, (oxygenated) seawater itself exhibits a negative Ce-anomaly (e.g., Elderfield and Greaves, 1982).

The western site Type I serpentinites range to the highest U concentrations (5.05 µg/g), whereas the Type II melt-impregnated serpentinites of central site M0072 and eastern site M0068 range to the lowest U concentrations (0.01 µg/g) (Fig. 6a, Table 3), which suggests that U enrichment is associated with serpentinization and oxidation, and not melt-impregnation. Uranium enrichment in serpentinites is common as U is hosted by serpentine phases (e.g., Deschamps et al., 2010). Frisby et al. (2016a, b) have shown that U enrichments correlate with Ce anomalies and the amount of Nd derived from seawater, which is a proxy for water/rock values. Thus, U enrichments have been shown explicitly to reflect fluid-rock interaction in abyssal peridotites.

In the case of Sr enrichment (Fig. 6b), evidence is not as clear. However, we note that the Type II melt-impregnated central site M0072 and eastern site M0068 serpentinites range to the lowest Sr concentrations, with the former exhibiting the lowest concentrations of Sr (1.02-4.01 µg/g) of all sites, whereas the other sites locally show distinct Sr enrichments. This suggests that Sr enrichment is not associated with melt-impregnation.

6.2. Evidence for melt-impregnation processes: Enrichment in incompatible elements, LREE, LREE fractionations and ΣREE

As explained above, we infer melt-impregnation in central site M0072 serpentinites on the basis of compositional similarities with melt-impregnated serpentinites constrained on the basis of macroscopic and microscopic evidence, even though site M0072 serpentinites lack observable evidence of melt-impregnation at the scale of core and thin section. Hence, due to the absence of such mineralogical evidence, we term these M0072 serpentinites 'cryptically melt-impregnated'.

The HFSE, e.g., Th, Hf, Zr (Figs. 7a-c), Nb, and Ti are highest in Type II melt-impregnated serpentinites at central Site M0072 and eastern Site M0068 and lowest in western sites Type I serpentinites. In addition, Figures 7d and 7e show an increase in LREE and ΣREE, and possibly LREE fractionation from Type I serpentinites to Types II and III serpentinites, and from west to central to east. For example, apart from a lone Ca-rich Type I serpentinized dunite, which exhibits anomalously high La and anomalously low Ce and La/Yb_{CN} of 2.39, the remaining western Type I serpentinites yield La/Yb_{CN} of 0.11-0.47 and mean ΣREE of 0.39 µg/g (including the Ca-rich dunite). The central Type I and II serpentinites yield a range of La/Yb_{CN} of 0.15-1.31 and mean ΣREE of 2.40 µg/g, and the eastern Types I, II and III serpentinites yield a range of La/Yb_{CN} of 0.61-1.68 and mean ΣREE of 12.66 µg/g. Thus, overall, melt impregnation produces less LREE fractionation and more elevated ΣREE compared to processes dominated by fluid-rock interaction.

6.3. Evidence of silica metasomatism

Talc- and amphibole-rich fault rocks form as the result of silica metasomatism and have been recovered from detachment fault surfaces along slow and ultra-slow spreading mid-ocean ridges including oceanic core complexes (e.g., Escartín et al., 2003; Schroeder and John, 2004; Boschi et al., 2006b; McCaig et al., 2007; Picazo et al., 2021). These rocks record heterogeneous deformation under greenschist-facies conditions and are commonly restricted to localized shear zones (< 200 m), which are associated with intense talc-amphibole metasomatism (Escartín et al., 2003; Boschi et al., 2006b). Talc is mechanically weak and thus may be critical to the development of such fault zones and may enhance unroofing of upper mantle peridotites and lower crustal gabbroic rocks during seafloor spreading. In the case of the Atlantis Massif, talc metasomatism is associated with serpentinite dehydration (Boschi et al., 2008). Strontium isotope compositions of talc-rich fault rocks indicate that talc metasomatism along detachment faults occurs at low water/rock values (0.2–0.7) and reflect interaction with Si-rich, evolved fluids with a mafic component derived from interaction with gabbro lenses within a peridotite-dominated ridge segment (Boschi et al., 2008).

In our study, silica metasomatism is reflected by plots of MgO/SiO_2 vs. Al_2O_3/SiO_2 (Fig. 3) and MgO vs. SiO_2 (Fig. 4a). These figures demonstrate the distinct whole rock geochemistry of the talc-altered Type III metasomatic serpentinites and talc schists from the eastern site M0068. In MgO vs. SiO_2 space (Fig. 4a), the talc-bearing serpentinites and talc schists are clearly distinct from all other Exp. 357 serpentinites by much lower MgO and much higher SiO_2 contents. These low MgO/SiO_2 and Al_2O_3/SiO_2 values of < 0.02 are indicative of silica metasomatism and are close to compositions of talc-bearing harzburgites recovered during ODP Leg 209 (Paulick et al., 2006).

6.4. Discrimination of fluid-rock vs. melt-dominated processes

6.4.1. Comparison with global abyssal peridotites

Figure 8a highlights trace element variations of mean global abyssal peridotites with compositions dominated by melt-rock interaction vs. those dominated by fluid-rock interaction associated with serpentinization (as interpreted by Paulick et al., 2006). We note that (in Fig. 8) we are comparing patterns, as absolute concentrations are subject to other processes (e.g., melt addition). Serpentinites subjected to mafic melt-impregnation exhibit enrichments in incompatible elements relative to those that have not been affected by melt-impregnation (Fig. 8a). In Figure 8b, we plot the mean serpentinite composition of each Expedition 357 location (i.e., west, central, east) vs. the mean compositions of melt-dominated and fluid-dominated global abyssal peridotites as shown in Fig. 8a. In Fig. 8c, we parse the mean peridotite compositions according to borehole of the central sites. There are clear differences in incompatible element concentrations between Exp. 357 Type II melt-impregnated serpentinites and Type III metasomatic serpentinites relative to Type I serpentinites, with Types II and III exhibiting greater abundances of all incompatible elements (Fig. 8b). In particular, the Type I serpentinites from the western site have PM-normalized incompatible element abundances that are most similar to fluid-dominated peridotites, whereas central sites serpentinites exhibit concentrations most similar to melt-dominated peridotites; eastern site serpentinites have incompatible abundances more enriched than melt-rock dominated peridotites (Fig. 8b). Apart from U and Sr, the Exp. 357 serpentinites show a clear enrichment in all other incompatible elements from the western to central to eastern sites (Fig. 8b).

6.4.2. HFSE vs. LREE

On the basis of selected HFSE vs. LREE and HFSE vs. MREE/HREE variations, Paulick et al. (2006) showed that the global abyssal peridotite dataset of Niu (2004) exhibit relatively steep positive trends, which was interpreted as indicative of dominant melt-rock interaction processes. The reason for this trend is related to differences in the behavior of LREE and HFSE; LREE are more hydrophilic than HFSE, and so are more readily transported in solution. Although melt-rock reaction mobilizes both LREE and HFSE, fluid-dominated reactions preferentially mobilize LREE, resulting in distinctly different patterns (Niu, 2004). A trend defined by only minor increase in HFSE concentrations (i.e., a sub-horizontal as opposed to steep positive trend) on the other hand, is indicative of dominantly hydrothermal alteration processes (i.e., fluid-rock interaction), which affect the more immobile HFSE to a lesser extent than the REE (Paulick et al., 2006). In the dataset of ODP Leg 209 peridotites, Paulick et al. (2006) showed that those at Sites 1270 and 1271 exhibit steep trends similar to the dataset of Niu (2004), whereas those of Sites 1268, 1272 and 1274 show less steep, subhorizontal trends, which they interpreted as more consistent with fluid-rock interaction.

Fig. 9 shows Expedition 357 serpentinites vs. the trends of global abyssal peridotites, with compositions dominated by (i) melt-rock interaction, and (ii) fluid-rock interaction in Nb vs. La and Ti vs. Dy space. These plots produce two distinct linear trends, which mimic the two described above, in agreement with the observations presented in Fig. 8. The serpentinites of the central and eastern sites, which show ample evidence of melt-impregnation, exhibit steep trends indicative of compositions dominantly controlled by melt-rock interaction similar to those of the global MOR peridotite dataset of Niu (2004) and ODP Leg 209 Sites 1270 and 1271 of Paulick et al. (2006). In contrast, Type I serpentinites from the western site, which show minimal evidence of melt-impregnation, instead show flatter, subhorizontal trends suggestive of compositions mostly controlled by fluid-rock reactions, similar to trends of peridotites of ODP Leg 209 Sites 1268, 1272 and 1274. We note also that similar relations and trends occur on other plots of HFSE vs. LREE and MREE (e.g., Th vs. Ce, Ti v. Ce, Hf vs. Pr, Nb vs. $[Gd/Lu]_{CN}$ and Ti vs. $[Gd/Lu]_{CN}$, Supplementary Fig. S2). In the case of Expedition 357 serpentinites, in all instances, the slope of the trends of the central and eastern site serpentinites are steeper than the slope of the trend of the western site serpentinites, consistent with compositions of the former being the result of dominant melt-rock reaction and compositions of the latter being the result of dominantly fluid-rock interaction. When the central location is parsed into discrete sites, compositions of serpentinites from central Site M0069 are consistent with being dominated by fluid-rock interaction, whereas those of central Sites M0072 and M0076 are consistent with being dominated by melt-rock interaction.

6.5. Petrogenesis: Estimates of degrees of melt extraction

Chondrite-normalized REE and PM-normalized patterns (Fig. 5) are used to explain differences in the relative depletion of peridotites of each site investigated and provide evidence of fluid-dominated processes and melt-impregnation processes

(Sections 6.1.-6.4.), based on the compositional variation of Expedition 357 serpentinites. Below, we model estimates of partial melting undergone by the peridotites based on trace and REE chemistry.

Various highly incompatible and immobile trace elements (Yb, Nb, Zr) in serpentinites from western Site M0071 and central Sites M0069 and M0076 exhibit extreme depletion relative to DMM, in contrast to the central Site M0072 serpentinites that exhibit enriched chondrite-normalized patterns relative to DMM apart from a lone moderately depleted Type I serpentinized dunite. The eastern Site M0068 serpentinites exhibit LREE concentrations more enriched than DMM but HREE slightly to moderately more depleted than DMM. Evidence in support of high degrees of melt depletion includes the high depletion in Al_2O_3 and CaO (Fig. 4), and the aforementioned other incompatible trace elements (Fig. 7, Table 3). Below, we provide estimates of the maximum degrees of melt extraction based on modelling of whole rock REE concentrations and note that REE patterns of many samples are strongly affected by refertilization, which thus needs to be taken into account to derive accurate estimates of melt depletion.

The REE patterns of the most melt-depleted sample for each of the five sites are shown in Fig. 10 and compared with curves predicted by modeling of melt depletion followed by subsequent metasomatism. As LREE are most strongly depleted during partial melting, and therefore sensitive to refertilization, this part of the REE pattern is essentially that of the metasomatizing agent. As a result, different amounts of metasomatism will shift the LREE pattern up or down, but the slope of the LREE pattern (La/Sm) is barely affected. This slope is strongly variable in our dataset, ranging from LREE-depleted ($[La/Sm]_{CN}$ = 0.3-0.9) to strongly enriched ($[La/Sm]_{CN}$ = 2-5). The REE patterns in Figs. 5a-e show at least two distinct melts that have infiltrated the peridotites, an enriched (*E*) and a depleted type (*D*), of which the most REE-rich examples are from eastern Site M0068 (samples 68A-1R1-34-35 and 68A-1R1-1-6). In these samples, the original peridotite REE patterns have been completely overprinted by the infiltrating melts. Therefore, we chose these peridotites to estimate the composition of the two endmember contaminants during modeling (*E* and *D*, respectively). Both types can be observed at each site, although central Sites M0072 and M0076 are dominated by a *D*-type contaminant. Some serpentinites show evidence of infiltration by an even more enriched contaminant (*SE*), the composition of which is more difficult to estimate. As this contaminant is strongly LREE-enriched and therefore relatively HREE poor, its exact composition will have little effect on our melt fraction estimates, which are based on the HREE part of the patterns.

The calculated volume of fractional non-modal melt extraction (see Fig. 10 caption for model parameters) of the most depleted sample from each site ranges from 19 to 21 % (Fig. 10), which indicates little difference in the maximum amount of melt extraction between the sites. The difference in the REE patterns between the sites are primarily due to small but variable amounts of infiltrating melts (<1 % for each of the five most depleted samples, Fig. 10).

These modeling results show little difference in the maximum amount of melt extraction between the different sites across the footwall. Unfortunately, significant melt infiltration experienced by many of the serpentinites makes it difficult to evaluate the average amount of melt extraction experienced by serpentinites of the different sites. For example, nearly all whole rock compositions of eastern Site M0068 and central Site M0072 are more enriched than DMM, which could be interpreted as very limited melt extraction, but refertilization of these samples will have obliterated any previous melt extraction history. Our modeling results suggest that differences in REE patterns observed between sites are probably due to differences in refertilization, not partial melting.

6.6. Spatial variations in geochemical processes and peridotite composition

It was noted by Früh-Green et al. (2018) that there exists a weakly defined enrichment in peridotites from west to east. This pattern is actually strongly defined in terms of enrichment in LREE, LREE fractionation, ΣREE, and HFSE (Figs. 7-9 and Supplementary Fig. S2). For example, Fig. 8 shows a distinct increase in all incompatible elements except U, Pb, and Sr in the mean serpentinite compositions moving from west to central to east. Specifically, the western Type I serpentinites exhibit the lowest concentrations of HFSE of Nb, Zr, and Th whereas the eastern serpentinites exhibit the highest concentrations of these elements (Figs. 7a-c); the central serpentinites have concentrations intermediate to the western and eastern serpentinites. However, as we have also noted, there are distinctions in the central location when parsed into individual sites with central Site M0069 being depleted to the same degree as the western serpentinites and with the two other central sites (M0072 and M0076) being comparatively more enriched.

Moreover, this pattern of west to east enrichment is complementary to the relative volume of melt-impregnation and silica metasomatism recorded in sampled peridotite at each site. The eastern site comprises the largest percentage of melt-impregnated and silica-metasomatized peridotites (70%), relative to the central sites (35%), and the western site (a single sample out of nine, or 11%, is melt-impregnated, with no Type III silica-metasomatized serpentinites). However, the calculation for the central sites is underestimated as we do not include here the four cryptically melt-impregnated serpentinites of central Site M0072 from our dataset, which show no macroscopic or microscopic evidence of melt-impregnation. If we recalculate with the inclusion of these four M0072 serpentinites, the percentage of melt-impregnated and silica-metasomatized peridotites from the central sites increases to 52 %.

6.7. Links to OCC processes

The observed spatial variations in serpentinite composition needs to be interpreted in the context of both the limitations of our observations and taking into account the complex history of detachment fault formation and exhumation. We have shown that the western site Type I serpentinites record compositions consistent with dominantly fluid-rock interaction processes, whereas the central site serpentinites, considered collectively, and those from the eastern site record compositions consistent with having undergone dominant melt-rock interaction. Furthermore, there is a clear progression in the volume of melt-impregnations from west to central and east and a corresponding increase in incompatible element enrichment, a record of these increasing volumes of melt-enrichment.

Serpentinites from the western sites originated from shallower borehole depths of ~ 0-10 m relative to those of the central sites (a maximum of ~ 16 m in the cases of central Sites M00069A and M0076A, Fig. 1c). The present-day position of these samples cannot be directly related to that of the history of each sample, from lithospheric emplacement, subsequent interaction with melt, alteration, and exhumation. First, the detachment fault zone is likely a complex, anastomosing structure, with a thickness of ~100 m to ~ a few 100s of m (e.g., Karson et al., 2006; Escartín et al., 2017; Parnell-Turner et al., 2018), where fault blocks are transposed in the across-axis direction. In this case, variations in composition vs. borehole depth may not correspond to actual structural depths relative to the fault surface exposed at the seafloor, and now adjacent materials may have originated from different positions in the deformed fault zone. Second, the boreholes also include talus material that is therefore not *in situ*. The present-day location of these samples cannot be directly interpreted as an indicator of spatial and temporal relationships with samples *in situ*, and therefore have an ambiguous structural position. If these debris fields correspond to local mass-wasting deposits, visible at small scales over the detachment fault, the present-day position may be close to the original *in situ* position. Oceanic detachments also display a cover of rubble and sediment that is sourced from the hanging wall, and rafted during extension (e.g., Dick et al., 2008; Escartín et al., 2017). Thus, if the talus material corresponds to rubble cover, its source may be the hanging wall rather than the fault zone or footwall instead, and its present-day location does not necessarily reflect its position at the time of formation, emplacement, impregnation, or alteration.

The consistent grouping of samples with a similar melt-impregnation (or lack thereof) and alteration history at the eastern, central, and western sites may suggest that *in situ* samples have not witnessed significant (km-scale), lateral transposition along the fault zone, or at least at spatial scales that are smaller than any local spatial variation associated with melt-rock interactions. Similarly, the samples that are not *in situ*, with similar melt impregnation and alteration histories, suggest a local source; sampling of hanging wall rubble would likely result in an extremely heterogeneous and variable set of ultramafic samples, as observed from the rubble cover from other oceanic detachments (e.g., Escartín et al., 2007). The homogeneity is therefore consistent with a local origin, with material sourced from the mass-wasted fault zone, eventually mixed with basaltic rubble that is present in the boreholes (e.g., Früh-Green et al., 2018).

If the samples were either *in situ*, or sourced locally where *ex situ*, and if the lateral transposition of material within an anastomosing fault zone occurs at a smaller scale (< 1 km parallel to extension) than the distance between sites (3-5 km), then spatial patterns observed may be interpreted in the context of the internal structure and evolution of the

OCC and its detachment fault. Ildefonse et al. (2007) suggested a temporal variation in melt supply to the ridge axis, with an initial phase of accretion that has limited melt supply, and a late phase of accretion with increased melt supply and the emplacement of gabbros in the footwall. This interpretation is consistent with early peridotites just showing melt extraction (western sites), and melt-rock reactions in more recent time associated with this recent magmatic phase (eastern sites).

Alternatively, the sites may simply record an inherently heterogeneous system, where melt percolation, and hence melt-rock reactions, are inherently inhomogeneous. If this is the case, the east-west patterns may not reflect a temporal evolution but instead indicate that these heterogeneities occur over distances of a few km, corresponding to the separation among the different sites. This interpretation is consistent with geological observations and drilling that document a change in footwall composition along-axis, with peridotites near the transform fault wall, and gabbros ~ 10 km to the north, hence at spatial scales similar to those shown by the western, central, and eastern sites.

7. Conclusions

Peridotites sampled during IODP Expedition 357 comprise predominantly Type I serpentinites, with lesser Type II melt-impregnated and Type III metasomatic serpentinites. A principal variation in the nature and composition of Expedition 357 serpentinites is an increase in the volume of melt-impregnation products and a concomitant increase in HFSE and LREE enrichments from the western to central to eastern sites. Whole rock chemical compositions of western site Type I serpentinites are consistent with dominantly fluid-rock interaction associated with serpentinization and oxidation, whereas compositions of eastern site Type II melt-impregnated and Type III metasomatic serpentinites are dominated by melt-rock interaction processes. High to moderate degrees of melt extraction in the peridotites are evident in low concentrations of Al_2O_3, CaO and incompatible elements. Degrees of melt extraction based on whole rock REE suggest a high range of 19-21 % with no apparent variation between sites. Some serpentinite samples are rubble and therefore *ex situ*. Thus, the coherent magmatic history observed at each site may be consistent with a local source originating in the fault zone rather than rafted rubble that would be expected to show more heterogeneity and no spatial pattern. If this is accurate, our sites may provide a time-record of enhanced melt-rock interaction with time, consistent with proposed geological models. Otherwise, the magmatic history may represent heterogeneities in these processes at spatial scales of a few km.

Acknowledgments

This research used samples and data provided by the International Ocean Discovery Program (IODP). This project would not have been possible without the support of the entire IODP Expedition 357 scientific party and support staff from the ECORD Science Operator. In particular, we thank co-Chief Scientist Beth Orcutt, Expedition Project Managers Carol Cotterill and Sophie Green, Offshore Operations Manager David Smith, the ESO Laboratory and Curation Manager Ursula Roehl, and the entire team of the Bremen Core Repository at MARUM. Funding for Expedition 357 was provided by the European Consortium for Ocean Research Drilling (ECORD). SAW acknowledges financial support from the Korea International Ocean Discovery Program (K-IODP) funded by the Ministry of Oceans and Fisheries, Korea and internal funds provided by KFUPM Dept. of Geosciences. GFG acknowledges funding by the Swiss National Science Foundation (SNF) project No. 200021_163187 and Swiss IODP. MIL acknowledges that this research was undertaken thanks in part to funding from the Canada First Research

Excellence Fund through the Arthur B. McDonald Canadian Astroparticle Physics Research Institute.

Figure captions

Figure 1. (a) Location of the Atlantis Massif at 30°N within the context of the greater MAR spreading system (modified from Kelley et al., 2001). (b) Bathymetric map centered on the southern wall of the Atlantis Massif (modified after Rouméjon et al., 2018a). Inset shows the location of the Atlantis Massif on the western flank of the Mid-Atlantic Ridge axial valley, bordered to the south by the Atlantis Fracture Zone. Circles with numbers in italics and beginning with M00 represent shallow drill hole locations from IODP Exp. 357 (Früh-Green et al., 2017, 2018). White circles indicate drill holes with no recovered peridotite; blue, red and yellow circles represent western (M0071), central (M0069, M0072, M0076) and eastern (M0068) sites, with recovered peridotite samples investigated in this study. White squares represent sites (U1309, U1310, U1311) drilled during Exp. 304/305 (Blackman et al., 2006); white star shows the location of the Lost City Hydrothermal Field (LCHF) (Kelley et al., 2001). (c) Simplified downhole plots showing dominant rock types recovered in the seven drill holes hosting serpentinized peridotites (modified from Roumejon et al., 2018a; see Fruh-Green et al., 2018 for complete expedition drill hole vertical sections). The sections are arranged from right to left according to longitude (see Fig. 1b), and from hole top to bottom. The central holes embody *in situ* segments of the detachment footwall, whereas the western and eastern site holes which yield rubbly intervals and sedimentary structures are interpreted as artefacts of mass wasting and local faulting. Symbols: circles, harzburgite; squares, dunite; triangles, Ca-rich harzburgite; triangles with slash, Ca-rich dunite; crosses, melt-impregnated harzburgite; x's, plagioclase-impregnated harzburgite; diamonds, talc-

amphibole altered harzburgite; diamonds with slash; talc-amphibole-chlorite schist. Blue, red and yellow symbols represent samples of western, central and eastern serpentinized harzburgites and dunites, respectively, analyzed for whole rock chemical analysis. Note 'metamafic' includes metabasalt, metadolerite and metagabbro composition samples.

Figure 2. Representative thin section images of Expedition 357 Type I serpentinites (a-d), Type II (mafic) melt-impregnated (mm-i) serpentinite (e, f) and Type III metasomatic serpentinites (msp) (g, h). 'Typical' completely serpentinized peridotite samples from (a, b) 71A-1R2-85-89, harzburgite and (c) 71C-5R1-6-8, harzburgite. (d) Ca-rich serpentinized harzburgite 69A-9R2-8-12 showing extensive network of carbonate veinlets. (e, f) Mafic melt-impregnated (mm-i) harzburgites 76B-7R1-81-83 and 68B-4R1-23-29 with (e) the presence of rare plagioclase feldspar (f) and secondary (replacive) olivine mantling partially dissolved orthopyroxene porphyroclast. (e) Talc-amphibole altered (t-aa) harzburgite 68B-1R1-10-13, showing replacement of orthopyroxene by talc (Tlc) and tremolite (Tr), and (f) talc-schist 68B-1R1-1-6. Image (a) is under plane polarized light; images in (b-h) are under cross-nicols.

Figure 3. Plot of MgO/SiO_2 vs. Al_2O_3/SiO_2 for all studied serpentinites (top panel, Type I serpentinites, bottom panel, Type II melt-impregnated and Type III metasomatic serpentinites). The lighter shaded samples (light yellow, light blue and pink) of the same shape here and in all other figures are Expedition 357 Atlantis Massif peridotites from Früh-Green et al. (2016); light orange circles and squares harzburgites and dunites, respectively, from IODP Site U1309 Atlantis Massif peridotites (Godard et al., 2009). Global abyssal peridotite data from Niu (2004), Paulick et al. (2006) and Godard et al. (2008), unless stated otherwise. Fields of serpentinized peridotite and talc-altered

peridotite are from Paulick et al. (2006) and melt-impregnated peridotites (MIP) are from Paulick et al. (2006), Godard et al. (2008) and as referenced in Whattam et al. (2011). DMM (depleted MORB mantle) and PM (primitive mantle) from Workman and Hart (2005) and Palme and O'Neill (1983) respectively. The terrestrial array is from Jagoutz (1979).

Figure 4. Variation diagrams of MgO vs. (a) SiO_2, (b) Fe_2O_3, (c) Al_2O_3, (d) CaO and (e) LOI of Atlantic Massif serpentinites from this study, and peridotites of Godard et al. (2009) and Früh-Green et al. (2018) compared with global MOR peridotite and bulk compositions of serpentine and talc (Blanco-Quintero et al. 2011, mean of ten and eight serpentine and talc analyzes). Symbols as in Fig. 3.

Figure 5. (a-e) Chondrite-normalized REE and (f-j) primitive mantle-normalized incompatible element plots of Atlantis Massif serpentinites from this study and peridotites of the study of Früh-Green et al. (2018). Chondrite and primitive mantle values are from McDonough and Sun (1995). Shown for comparison is mean abyssal peridotite composition determined on the compilations of Niu (2004) and Bodinier and Godard (2003) by Godard et al. (2008), and depleted MORB mantle (DMM) (Workman and Hart, 2005).

Figure 6. IODP Expedition 357 serpentinite samples from this study, and peridotites of the study of Früh-Green et al. (2018) on plots of (a) U and (b) Sr vs. site. Note that three of the four high-CaO Type I serpentinites (with 5.59-10.50 wt.% CaO) also exhibit the highest concentrations of Sr (> 1000 µg/g). Symbols as in Fig. 3.

Figure 7. Expedition 357 Atlantis Massif serpentinites from this study and peridotites of the study of Früh-Green et al. (2018) in plots of (a) Th, (b) Hf, (c) Zr, (d) Ce/Yb and (e) total REE vs. site. Plotted for comparison are the ranges of fluid-rock dominated and melt-rock dominated global abyssal peridotite (GAP, references as in the caption for Fig. 5). Depleted mantle (DM) and primitive mantle (PM) compositions are from Workman and Hart (2005) and Lyubetskaya and Korenaga (2007), respectively. Symbols as in Fig. 3.

Figure 8. Primitive mantle-normalized plots of the mean compositions of (a) global abyssal peridotites interpreted as being dominated by fluid-rock and melt-rock reactions, (b) Atlantis Massif serpentinites from this study and (c) central serpentinites parsed into site. The fluid-rock dominated peridotite is from Paulick et al. (2006) and represent peridotites collected during ODP Leg 209, Sites 1268, 1772, 1274. The melt-rock dominated peridotite is from Niu (2004) and Paulick et al. (2006) and in the case of Paulick et al. (2006), represent peridotites collected from ODP Leg 209, Sites, 1270, 1271. Symbols as in Fig. 3

Figure 9. Expedition 357 Atlantis Massif serpentinites from this study and peridotites of the studies of Godard et al. (2009) and Früh-Green et al. (2018) in plots of (a, b) Nb vs. La, and (c, d) Ti vs. Dy. Element abundances listed as ‘0’ were assumed to be below detection limit and not used in calculation of the regression. Colors of the regressed lines and text for the Expedition 357 serpentinites include: blue, western; red, central; and black, eastern. In (b) and (d), the light blue, pink and light grey regressed lines represent mean of the western, central and eastern sites (i.e., the blue, red and black lines in (a) and (c)). R^2 values shown for Exp. 357 serpentinites represent ones which include the peridotite samples of Früh-Green et al. (2018) in addition to the serpentinites from this

study and the numbers in italics in brackets beside R^2 values represent number of samples used in regression calculation. The orange line represents the dataset of Atlantis Massif peridotites from Site U1309 (Godard et al., 2009). Linearly regressed vectors (grey) labelled *A*, *B*, and *C* in (a) and (c) represent data from global abyssal peridotite (GAP) and for visual clarity, samples are omitted from the plot. The *A* trend represents the dataset of Niu (2004) which was interpreted by Paulick et al. (2006) as being representative of dominant melt-rock interaction (i.e., melt-impregnation); *B* and *C* are from Paulick et al. (2006) and represent peridotites interpreted as having compositions dominantly associated with melt-rock reaction (*B*, ODP Leg 209, MAR, Sites, 1270, 1271) and fluid-rock reaction (*C*, Sites 1268, 1772, 1274). Depleted mantle (DM) and primitive mantle (PM) compositions from Workman and Hart (2005) and Lyubetskaya and Korenaga (2007), respectively. Symbols as in Fig. 3.

Figure 10. (a) REE compositions of the most melt-depleted sample from each site compared with model estimates of 10, 15, and 20 % partial melting of DMM as well as three 'best fit' models of melting and subsequent refertilization to estimate the extent of melting experienced by these samples. Modeling is of non-modal fractional melting (dashed curves encompassing light green shade) of partial melting in % (10, 15, 20) of a four phase DMM spinel lherzolite source comprising ol: opx: cpx: sp in modal proportions of 0.53: 0.27: 0.17: 0.03 and a melt mode of -0.06: 0.28: 0.67: 0.11 (Hellebrand et al. 2002). Initial source composition, DMM from Workman and Hart (2005). Partition coefficients from Suhr et al.,1998; missing REE interpolated. Also indicated are compositions of rocks after 20 % non-modal fractional melting and subsequent 1 % or 10 % addition of a mafic melt (mm, uppermost grey shaded area) with a REE composition of the most enriched sample (eastern site M0068A-1R1-34-35 talc-

schist, Früh-Green et al., 2018, see Fig. 4e) as a proxy for a slightly LREE-enriched melt (darker green shade). Symbols as in Fig. 3.

Table captions

Table 1 Evidence and means for classification of Expedition 357 serpentinites subjected to melt-impregnation and (silica) metasomatism.

Table 2 Mineralogy and modalogy of Expedition 357 serpentinites.

Table 3 Whole rock ICP-AES and ICP-MS analyses of Expedition 357 Atlantis Massif serpentinites from this study.

Supplementary material

See Supplementary Document

References

Absalov, M.Z., 1998. Chrome-spinels in gabbro-wehrlite intrusions of the Pechenga area, Kola Peninsula, Russia: emphasis on alteration features. Lithos 43, 109-134.

Andreani, M., Mével, C., Boullier, A.-M., Escartin, J., 2007. Dynamic control on serpentine crystallization in veins: constraints on hydration processes in oceanic peridotites. Geochemistry, Geophysics, Geosystems 8 (2), Q02012.

Akizawa, N., Früh-Green, G.L., Tamura, A., Tamura, C., Morishita, T., 2020. Compositional heterogeneity and melt transport in mantle beneath Mid-Atlantic Ridge constrained by peridotite, dunite, and wehrlite from Atlantis Massif. Lithos 354-355, 105364. https://doi.org/10.1016/j.lithos.2019.105364.

Andreani, M., Mevel, C., Boullier, A.-M., Escartin, J., 2007. Dynamic control on serpentine crystallization in veins: constraints on hydration processes in oceanic peridotites. Geochemistry, Geophysics, Geosystems 8.

Arai, S., Abe, N., Hirai, H., 1998. Petrological characteristics of the sub-arc mantle: An overview on petrology of peridotite xenoliths from the Japan Arcs. Trends in Mineralogy 2, 39-55.

Arai, S., Matsukage, K., 1996. Petrology of gabbro-troctolite–peridotite complex from Hess Deep, equatorial Pacific: implications for mantle–melt interaction within the oceanic lithosphere. In: Mével, C., Gillis, K.M., Allan, J.F., Meyer, P.S. (Eds.), Proceedings of the Ocean Drilling Program: Scientific Results, 147, pp. 135-155.

Arai, S., Shimizu, Y., Ismail, S.A., Ahmed, A.H., 2006. Low-T formation of high-Cr spinel with apparently primary chemical characteristics within podiform chromitite from Rayat, northeastern Iraq. Mineralogical magazine 70(5), 499-508.

Aswad, K.J.A., Aziz, N.R.H., Koyi, H.A., 2011. Cr-spinel compositions in serpentinites and their implications for the petrotectonic history of the Zagros Suture Zone, Kurdistan Region, Iraq. Geological Magazine 148(5-6), 802-818. doi:10.1017/S0016756811000422.

Bach, W., Klein, F. 2009. The petrology of seafloor rodingites:: Insights from geochemical reaction path modelin. Lithos 112(1-2), 103-117. http://dx.doi.org/10.1016/j.lithos.2008.10.022.

Ballhaus, C., Berry, R.F., Green, D.H., 1991. High pressure experimental calibration of the olivine-orthopyroxene-spinel oxygen barometer, implications for the oxidation of the mantle. Contributions to Mineralogy and Petrology 107, 27-40.

Barnes, S.J., 2000. Chromite in komatiites II. Modification during greenschist to mid-amphibolite facies metamorphism. Journal of Petrology, 41, 387-409.

Barnes, S.J., Roeder, P.L., 2001. The range of spinel compositions in terrestrial mafic and ultramafic rocks. Journal of Petrology 42(12), 2279-2302.

Barra, F., Gervilla, F., Hernández, E., Reich, M., Padrón-Navarta, J.A., González-Jiménez, J.M., 2014. Alteration patterns of chromian spinels from La Cabaña peridotite, south-central Chile. Mineralogy and Petrology 108, 819-836. DOI 10.1007/s00710-014-0335-5.

Bedini, R.M., Bodinier, J.-L., 1999. Distribution of incompatible trace elements between the constituents of spinel peridotite xenoliths: ICP-MS data from the East African Rift. Geochimica et Cosmochimica Acta, 63(22), 3883-3900.

Bhat, I.M., Ahmad, T., Subba Rao, D.V., 2019. Alteration of primary Cr-spinel mineral composition from the Suru Valley ophiolitic peridotites, Ladakh Himalaya: Their low-temperature metamorphic implications. Journal of Earth System Science 128:188. https://doi.org/10.1007/s12040-019-1222-6.

Blackman, D.K., Cann, J.R., Janssen, B., Smith, D.K., 1998. Origin of extensional core complexes: evidence from the Mid-Atlantic Ridge at Atlantis Fracture Zone. Journal of Geophysical Research: Solid Earth 103, 21315-21333.

Blackman, D.K., Karson, J.A., Kelley, D.S., Cann, J.R., Früh- Green, G.L., Gee, J.S., Hurst, S.D., John, B.E., Morgan, J., Nooner, S.L., Ross, D.K., Schroeder, T.J., Williams, E.A., 2002. Geology of the Atlantis Massif (Mid-Atlantic Ridge, 30° N): implications for the evolution of an ultramafic oceanic core complex. Marine Geophysical Researches 23, 443-469.

Blackman, D.K., Ildefonse, B., John, B.E., Ohara, Y., Miller, D.J., MacLeod, C.J., 2006. Proceedings of the IODP, 304/305. College Station TX. doi:10.2204/iodp.proc.304305.2006. (Integrated Ocean Drilling Program Management International, Inc.).

Blanco-Quintero, I.F., Proenza, J.A., García-Casco, A., Tauler, E., Galí, S., 2011. Serpentinites and serpentinites within a fossil subduction channel: La Corea mélange, eastern Cuba. Geologica Acta 9 (3-4), 389-405. DOI :10.1344/105.000001662.

Bodinier, J.L., Godard, M., 2003. Orogenic, ophiolitic, and abyssal peridotites. Treatise on Geochemistry, vol. 2. Elsevier, Amsterdam, pp. 103-170.

Bodinier, J.L., Menzies, M.A., Thirlwall, M.F., 1991. Continental to oceanic mantle transition: REE and Sr–Nd isotopic geochemistry of the Lanzo Lherzolite Massif. Journal of Petrology Special Volume 2, 191-210.

Boschi, C., Früh-Green, G.L., Delacour, A., Karson, J.A., Kelley, D.S., 2006a. Mass transfer and fluid flow during detachment faulting and development of an oceanic core complex, Atlantis Massif (MAR 30°N). Geochemistry, Geophysics Geosystems 7 (1), Q01004.

Boschi, C., Früh-Green, G.L., Escartin, J., 2006b. Occurrence and significance of serpentinite-hosted, talc-rich fault rocks in modern oceanic settings and ophiolite complexes. Ofioliti 31 (2), 123–134.

Boschi, C., Dini, A., Früh-Green, G.L., Kelley, D.S., 2008. Isotopic and element exchange during serpentinization and metasomatism at the Atlantis Massif (MAR 30°N): insights from B and Sr isotopes. Geochimica et Cosmochimica Acta 72 (7), 1801–1823.

Burkhard, D.J.M., 1993. Accessory chromian spinels: Their coexistence and alteration in serpentinites. Geochimica et Cosmochimica Acta 57, 1297-1306.

Cannat, M., 1993. Emplacement ofmantle rocks in the seafloor at mid-ocean ridges. Journal of Geophysical Research: Solid Earth 98 (B3), 4163-4172.

Cannat, M., Karson, J.A., Miller, D.J., Agar, S.M., Barling, J., Casey, J.F., Ceuleneer, G., Dilek, Y., Fletcher, J.M., Fujibayashi, N., Gaggero, L., Gee, J.S., Hurst, S.D., Kelley, D.S., Kempton, P.D., Lawrence, R.M., Marchig, V., Mutter, C., Niida, K., Rodway, K., Ross, D.K., Stephens, C.J., Werner, C.-D. and Whitechurch, H., 1995. Mid-Atlantic Ridge: Sites 920–924. Proc. ODP, Initial Reports, 153. Ocean Drilling Program, Texas A&M University, College Station, TX, United States.

Cann, J.R., Blackman, D.K., Smith, D.K., McAllister, E., Janssen, B., Mello, S., Avgerinos, E., Pascoe, A.R., Escartín, J., 1997. Corrugated slip surfaces formed at ridge-transform intersections on the Mid-Atlantic Ridge. Nature 385, 329-332.

Dare, S.A.S., Pearce, J.A., McDonald, I., Styles, M.T., 2009. Tectonic discrimination of peridotites using fO_2–Cr# and Ga–Ti–Fe^{III} systematics. Chemical Geology 261, 199-216.

Deschamps, F., Guillot, S., Godard, M., Chauvel, C., Andreani, M., Hattori, K., 2010. In situ characterization of serpentinites from forearc mantle wedges: Timing of serpentinization and behavior of fluid-mobile elements in subduction zones. Chemical Geology 269, 262-277. http://dx.doi.org/10.1016/j.chemgeo.2009.10.002.

Dick, H.J.B., Bullen, T., 1984. Chromian spinel as a petrogenetic indicator in abyssal and alpine-type peridotites and spatially associated lavas. Contributions to mineralogy and petrology 86, 54-76.

Dick, H.J.B., Natland, J.H., Alt, J.C., Bach,W., Bideau, D., Gee, J.S., Haggas, S., Hertogen, J.G.H., Hirth, G., Holm, P.M., Ildefonse, B., Iturrino, G., John, B.E., Kelley, D.S., Kikawa, E., Kingdon, A., LeRoux, P.J., Maeda, J., Meyer, P.S., Miller, D.J., Naslund, H.R., Niu, Y., Robinson, P.T., Snow, J.E., Stephen, R.A., Trimby, P.W.,Worm, H.-U., Yoshinobu, A., 2000. A long in situ section of the lower ocean crust: results of ODP Leg 176 drilling at the Southwest Indian Ridge. Earth and Planetary Science Letters 179, 31-51.

Dick, H.J.B., Tivey, M.A., Tucholke, B.E., 2008. Plutonic foundation of a slow-spreading ridge segment: Oceanic core complex at Kane Megamullion, 23° 30’N, 45 °20’W. Geochemistry, Geophysics, Geosystems 9, Q05014. doi:10.1029/2007GC001645.

Donnelly, K.E., Goldstein, S.L., Langmuir, C.H., Spiegelman, M., 2004. Origin of enriched ocean ridge basalts and implications for mantle dynamics. Earth and Planetary Science Letters, 226, 347-366.

Drouin, M., Godard, M., Ildefonse, B., Bruguier, O., Garrido, C.J., 2009. Geochemical and petrographic evidence for magmatic impregnation in the oceanic lithosphere at Atlantis Massif,Mid-Atlantic Ridge (IODP Hole U1309D, 30°N). Chemical Geology 264, 71-88.

Elderfield, H. and Greaves, M.J., 1982. The rare earth elements in seawater. Nature 296, 214-219.

Escartín, J., Mével, C., MacLeod, C.J., and McCaig, A.M., 2003, Constraints on deformation conditions and the origin of oceanic detachments: The Mid-Atlantic Ridge core complex at 15°45'N: Geochemistry, Geophysics, Geosystems, v. 4, no. 8, p. 1067, doi:10.1029/2001GC000278.

Escartin, J., Mével, C., Petersen, S., Bonnemains, D., Cannat, M., Andeani, M., Augustin, N., Bezos, A., Chavagnac, V., Choi, Y., Godard, M., Haaga, K., Hamelin, C., Ildefonsa, B., Jamieson, J., John, B., Leleu, T., MacLeod, C.J., Massot-Campos, M., Nomikou, P., Olive, J.A., Paquet, M., Rommevaux, C., Rothenbeck, M., Steinfuhrer, Tominaga, M., Triebe, L., Campos, R., Gracias, N., Garcia, R., 2017. Tectonic structure, evolution, and the nature of oceanic complexes and their detachment zones (13º20$^{/}$N and 13º30$^{/}$N, Mid Atlantic Ridge). Geochemistry, geophysics, geosystems. doi: 10.1002/2016GC006775.

Evans, B.W., Frost, B.R., 1975. Chrome-spinel in progressive metamorphism; a preliminary analysis. Geochimica et Cosmochimica Acta, 39, 959-972.

Evans, B.W., Trommsdorff, V., 1970. Regional metamorphism of ultramafic rocks in the Central Alps Paragenesis in the system CaO-MgO-SiO_2-H_2O. Schweiz.Min.Pen.Milt. 50, 481-492.

Ferrando, C., Godard, M., Ildefonse, B., Rampone, E., 2018. Melt transport and mantle assimilation at AtlantisMassif (IODP Site U1309): constraints from geochemical modeling. Lithos 323, 24-43.

Franz, L., Wirth, R., 2000. Spinel inclusions in olivine of peridotite xenoliths from TUBAF seamount (Bismark Archipelago/Papua New Guinea): evidence for the thermal and tectonic evolution of the oceanic lithosphere. Contributions to Mineralogy and Petrology 140, 283-295.

Frisby, C., Bizimis, M., Mallick, S., 2016a. Hf-Nd isotope decoupling in bulk abyssal peridotites due to serpentinization. Chemical Geology 440, 60-72. http://dx.doi.org/10.1016/j.chemgeo.2016.07.006.

Frisby, C., Bizimis, M., Mallick, S., 2016b. Seawater-derived rare earth element addition to abyssal peridotites during serpentinization. Lithos 248-251, 432-454.

Frost, B.R., Beard, J.S., McCaig, A., Condliffe, E., 2008. The formation of micro-rodingites from IODP Hole U1309D: Key in understanding the process of serpentinization. Journal of Petrology 49(9), 1579-1588. http://dx.doi.org/10.1093/petrology/egn038.

Früh-Green, G.L., Connolly, J.A.D., Plas, A., Kelley, D.S., Grobéty, B., 2004. Serpentinization of oceanic peridotites: implications for geochemical cycles and biological activity. In: Wilcock, W.S.D., DeLong, E.F., Kelley, D.S., Baross, J.A., Cary, C. (Eds.), The Subseafloor Biosphere at Mid-Ocean Ridges. Geophysical Monograph. 144, pp. 119-136.

Früh-Green, G.L., Orcutt, B.N., Green, S.L., et al., 2017. Expedition 357 summary. In: Früh- Green, G.L., Orcutt, B.N., Green, S.L., Cotterill, C. (Eds.), Expedition 357 Scientists. Proceedings of the International Ocean Discovery Program 357, College Station, TX. https://doi.org/10.14379/iodp.proc.357.101.2017.

Früh-Green, G.L., Orcutt, B.N., Green, S., Cotterill, C., and the Expedition 357 Scientists, 2016. Expedition 357 Preliminary Report: Atlantis Massif Serpentinization and Life. International Ocean Discovery Program. 10.14379/iodp.pr.357.2016

Früh-Green, G.L., Orcutt, B.N., Rouméjon, S., et al., 2018. Magmatism, serpentinization and life: insights through drilling the Atlantis Massif (IODP Expedition 357). Lithos 323, 137-155. https://doi.org/10.1016/j.lithos.2018.09.012.

Gargiulo, M.F., Bjerg, E.A., Mogessie, A., 2013. Spinel group minerals in metamorphosed ultramafic rocks from Río de Las Tunas belt, Central Andes, Argentina. Geologica Acta 11(2), 133-148. doi : 10.1344 / 105 .000001836.

Grimes, C.B., John, B.E., Cheadle, M.J., Wooden, J.L., 2008. Protracted construction of gabbroic crust at a slow spreading ridge: constraints from 206Pb/238U zircon ages from Atlantis Massif and IODP Hole U1309D (30°N, MAR). Geochemistry, Geophysics, Geosystems 9 Q08012.

Godard, M., Lagabrielle, Y., Alard, O., Harvey, J., 2008. Geochemistry of the highly depleted peridotites drilled at ODP Sites 1272 and 1274 (Fifteen–Twenty Fracture Zone, Mid-Atlantic Ridge): implications for mantle dynamics beneath a slow spreading ridge. Earth and Planetary Science Letters 267 (3-4), 410–425. doi:10.1016/j.epsl.2007.11.058.

Godard, M., Awaji, S., Hansen, H., et al., 2009. Geochemistry of a long in-situ section of intrusive slow-spread oceanic lithosphere: results fromIODP Site U1309 (Atlantis Massif, 30°N Mid-Atlantic-Ridge). Earth and Planetary Science Letters 279, 110-122.

González-Jiminéz, J.M., Kerestedjian, T., Proenza, J.A., Gervilla, F., 2009. Metamorphism on Chromite Ores from the Dobromirtsi Ultramafic Massif, Rhodope Mountains (SE Bulgaria). Geologica Acta 67, 7(4), 413-429. DOI: 10.1344/104.000001447.

Hart, S.R., Zindler, A., 1986. In search of a bulk-earth composition. Chemical Geology 57, 247-267.

Heinrich, K.F.J., 1987. Mass absorption coefficients for electron probe microanalysis. In: Brown, J. Packwood, R. (Eds.), Proceedings of the 11th International Congress on X-Ray Optics and Microanalysis, University of Western Ontario, London, Ontario, Canada 1986, pp. 67-119.

Hellebrand, E., Snow, J.E., Dick, H.J.B., Hofmann, A.W., 2001. Coupled major and trace elements as indicators of the extent of melting in mid-ocean-ridge peridotites. Nature 410, 677-681.

Ildefonse, B., Blackman, D.K., John, B.E., Ohara, Y., Miller, D.J., MacLeod, C.J., 2007. Oceanic core complexes and crustal accretion at slow-speading ridges. Geology 35, 623-626.

Irvine, T.N., 1967. Chromian spinel as a petrogenetic indicator Part 2, petrologic applications. Canadian Journal of Earth Sciences 4, 71-103.

Jagoutz, E., Palme, H., Baddenhausen, H., Blum, K., Cendales, M., Dreibus, G., Spettel, B., Lorenz, V., Vanke, H., 1979. The abundance of major, minor and trace elements in the earth's mantle as derived from primitive ultramafic nodules. Geochimica et Cosmochimica Acta 11 (2), 2031-2050.

Karson, J.A., 2002. Geologic structure of the uppermost oceanic crust created at fast- to intermediate-rate spreading centers. Annual Review of Earth and Planetary Sciences 30, 347–384.

Karson, J.A., Früh-Green, G.L., Kelley, D.S., Williams, E.A., Yoerger, D.R., Jakuba, M., 2006. Detachment shear zone of the Atlantis Massif core complex, Mid-Atlantic Ridge, 30°N. Geochemistry, Geophysics Geosystems 7 (6), Q06016.

Kelemen, P.B., 1990. Reaction between ultramafic rock and fractionating basaltic magma I. Phase relations, the origin of calc-alkaline magma series, and the formation of discordant dunite. Journal of Petrology 31, 51-98.

Kelemen, P.B., Hirth, G., Shimizu, N., Spiegelman, M., Dick, H., 1997. A review of melt migration processes in the adiabatically upwelling mantle beneath oceanic spreading ridges. Philosophical Transactions of the Royal Society of London. Series A355, 283-318.

Kelemen, P., Kikawa, E., Miller, J., Abe, N., Bach,W., Carlson, R.L., Casey, J.F., Chambers, L.M., Cheadle, M., Cipriani, A., Dick, H.J.B., Faul, U., Garces, M., Garrido, C., Gee, J.S., Godard, M., Griffin, D.W., Harvey, J., Ildefonse, B., Iturrino, G.J., Josef, J., Meurer,W.P., Paulick, H., Rosner, M., Schroeder, T., Seyler, M., Takazawa, E. and Mrozewski, S., 2004. Drilling Mantle Peridotite along the Mid-Atlantic Ridge from 14° to 16°N: Sites 1268-1275. Proc. ODP, Initial Reports, 209. Ocean Drilling Program, Texas A&M University, College Station TX 77845-9547, USA. doi:10.2973/odp.proc.ir.209.2004 pp.

Kelemen, P.B., Kikawa, E., Miller, D.J., Shipboard Scientific Party, 2007. Leg 209 summary: processes in a 20-km-thick conductive boundary layer beneath the Mid-Atlantic Ridge, 14°–16°N. In: Kelemen, P.B., Kikawa, E., Miller, D.J. (Eds.), Proceedings of the Ocean Drilling Program, Scientific Results, 209: College Station, TX. Ocean Drilling Program, pp. 1-33.

Kelemen, P.B., Shimizu, N., Salters, V.J.M., 1995. Extraction of mid-ocean-ridge basalt from the upwelling mantle by focused flow of melt in dunite channels. Nature 375, 747-753.

Kelley, D.S., Karson, J.A., Blackman, D.K., Fruh-Green, G.L., Butterfield, D.A., Lilley, M.D., Olson, E.J., Shrenk, M.O., Roe, K.K., Lebon, G.T., Rivizzigno, P., 2001. An off-axis hydrothermal vent field discovered near the Mid-Atlantic Ridge at 30°N. Nature 412, 145-149.

Khalil, K.I., El-Makky, A.M., 2009. Alteration Mechanisms of Chromian-Spinel during Serpentinization at Wadi Sifein Area, Eastern Desert, Egypt. Resource Geology 59(2), 194-211. doi: 10.1111/j.1751-3928.2009.00090.x.

Kimball, K.L. (1990) Effects of hydrothermal alteration on the compositions of chromian spinels. Contributions to Mineralogy and Petrology, 105, 337-346.

Leybourne, M.I., Peter, J.M., Layton-Mathews, D., Volesky, J., Boyle, D.R., 2006. Mobility and fractionation of rare earth elements during supergene weathering and gossan formation and chemical modification of massive sulphide gossan. Geochimica et Cosmochimica Acta 70(5), 1097-1112. https://doi.org/10.1016/j.gca.2005.11.003

Lenoir, X., Garrido, C.J., Bodinier, J.-L., Dautria, J.-M., Gervilla, F., 2001. The recrystallization front of the Ronda peridotite: evidence for melting and thermal erosion of subcontinental lithospheric mantle beneath the Alboran Basin. Journal of Petrology 42, 141-158.

Liebmann, J., Schwarzenbach, E.M., Früh- Green, G.L., Boschi, C., Rouméjon, S., Strauss, H., Wiechert, U., John, T., 2018. Tracking Water- Rock Interaction at the Atlantis Massif (MAR, 30°N) using sulfur geochemistry. Geochemistry, geophysics, geosystems, 19(11), 4561-4583. doi:10.1029/2018GC007813.

Lyubetskaya, T., Korenaga, J., 2007. Chemical composition of Earth's primitive mantle and its variance: 1. Method and resultsJournal of Geophysical Research 12, B03211. doi:10.1029/2005JB004223.

Macdonald, K.C., 1982. Mid-ocean ridges: fine scale tectonic, volcanic and hydrothermal processes within the plate boundary zone. Annual Review of Earth and Planetary Sciences 10, 155-190.

McCaig, A.M., Cliff, R.A., Escartin, J., Fallick, A.E., MacLeod, C.J., 2007. Oceanic detachment faults focus very large volumes of black smoker fluids. Geology 35 (10), 935-938.

McCaig, A.M., Delacour, A., Fallick, A.E., Castelain, T., Früh-Green, G.L., 2010. Fluid circulation and isotopic alteration in and beneath oceanic detachment faults in the Central Atlantic: Implications for the geometry and evolution of high-temperature hydrothermal circulation cells at slow-spreading ridges, In: Diversity of Hydrothermal Systems on Slow Spreading Ocean Ridges. In: Rona, P.A., Devey, C.W., Dyment, J.,Murton, B.J. (Eds.), AGU Geophy. Mono. Series. 188, pp. 207–239.

McDonough, W.F. and Rudnick, R.L., 1998. Mineralogy and composition of the upper mantle. In: Hemley, R.J. (Ed.), Ultrahigh pressure mineralogy: Reviews in Mineralogy, V. 37, Mineralogical Society of America, DeGruyter, pp. 139-164. https://doi.org/10.1515/9781501509179.

McDonough, W.F., Sun, S.S., 1995. The composition of the Earth. Chemical Geology 120, 223-253.

Merlini, A., Grieco, G., Diella, V., 2009. Ferritchromite and chromian-chlorite formation in mélange-hosted Kalkan chromitite (Southern Urals, Russia). American Mineralogist 94, 1459-1467.

Müntener, O., Pettke, T., Desmurs, L., Meier, M., Schaltegger, U., 2004. Refertilization of mantle peridotite in embryonic ocean basins: trace element and Nd isotopic evidence and implications for crust–mantle relationships. Earth and Planetary Science Letters 221, 293-308. doi:10.1016/S0012-821X(04)00073-1.

Niida, K., 1997. Mineralogy of MARK peridotites: replacement through magma channeling examined from 920D, MARK area. In: Karson, J.A., Cannat, M., Miller, D.J., Elthon, D. (Eds.), Proceedings of the Ocean Drilling Program: Scientific Results,153. Ocean Drilling Program, College Station, TX, pp. 265-275.

Niu, Y., 1997. Mantle melting and melt extraction processes beneath ocean ridges: evidence from abyssal peridotites. Journal of Petrology 38, 1047-1074.

Niu, Y., 2004. Bulk rock major and trace element compositions of abyssal peridotites: implications for mantle melting, melt extraction and post-melting processes beneath mid-ocean ridges. Journal of Petrology 45, 2423-2458.

Obata M., Banno, S., Mori, T., 1974. The iron-magnesium partitioning between naturally occurring coexisting olivine and Ca-rich clinopyroxene: an application of the simple mixture model to olivine solid solution. Bull. Soc. Jr. Miner. Crystallogr., 97, 101-107.

O'Hanley, D.S., 1996. Serpentinites Records of Tectonic and Petrological History. Oxford, Oxford University Press, 290 pp.

Palme, H., O'Neill, H.S.C., 2003. Cosmochemical estimates of mantle composition, In: Treatise on Geochemistry, vol. 2, Holland, H., Turekian, K.K., (Eds.), pp. 1-38, Elsevier, New York.

Parnell-Turner, R., Escartín, J., Olive, J.-A., Smith, D.K., and Petersen, S., 2018, Genesis of corrugated fault surfaces by strain localization recorded at oceanic detachments: Earth and Planetary Science Letters, v. 498, p. 116–128, doi: 10.1016/j.epsl.2018.06.034.

Parkinson, I.J., Pearce, J.A., 1998. Peridotites from the Izu–Bonin–Mariana Forearc (ODP Leg 125), evidence for mantle melting and melt–mantle interaction in a suprasubduction zone setting. Journal of Petrology 39, 1577-1618.

Paulick, H., Bach,W., Godard, M., De Hoog, J.C.M., Suhr, G., Harvey, J., 2006. Geochemistry of abyssal peridotites (Mid-Atlantic Ridge, 15°20′N, ODP Leg 209): implications for fluid/rock interaction in slow spreading environments. Chemical Geology 234, 179-210.

Picazo, S., Cannat, M., Delacour, A., Escartin, J., Rouméjon, S., Silantyev, 2012. Deformation associated with the denudation of mantle-derived rocks at the Mid-Atlantic Ridge 13°-15°N: The role of magmatic injections and hydrothermal alteration. Geochemistry, geophysics, geosystems 13(9). https://doi.org/10.1029/2012GC004121

Pouchou, J.-L., Pichoir, F., 1991. Quantitative analysis of homogeneous or stratified microvolumes applying the model "PAP". In: Heinrich, K.F.J., Newbury, D.E. (Eds.), Electron Probe Quantitation Plenum Publishing Corporation, New York, New York, pp. 31-75.

Purvis, A.C., Nesbitt, R.W., Hallberg, J.A., 1972. The geology of the part of the Carr Boyd rocks complex and it's associated nickel mineralization, Western Australia. Economic Geology 67, 1093-1113.

Quick, J.E., 1981. The origin and significance of large, tabular dunite bodies in the Trinity peridotite, northern California. Contributions to Mineralogy and Petrology 78, 413-422.

Rampone, E., Piccardo, G.B.,Vannucci, R., Bottazzi, P., 1997. Chemistry and origin of trapped melts in ophiolitic peridotites. Geochimica et Cosmochimica Acta 61, 4557-4569.

Rampone, E., Piccardo, G.B., Vannucci, R., Bottazzi, P., Zanetti, A., 1994. Melt impregnation in ophiolitic peridotite: an ion microprobe study of clinopyroxene and plagioclase. Mineralogical Magazine 58A, 756-757.

Reed, S.J.B., 1990), Fluorescence effects in quantitative microprobe analysis. In: Williams, D.B., Ingram, P., Michael, J.R. (Eds.), Microbeam Analysis-1990 San Francisco Press, San Francisco, pp. 109-114.

Rouméjon, S., Cannat, M., Agrinier, P., Godard, M., Andreani, M., 2015. Serpentinization and Fluid Pathways in Tectonically Exhumed Peridotites from the Southwest Indian Ridge (62-65 E). Journal of Petrology 56, 703-734.

Rouméjon, S., Früh-Green, G.L., Orcutt, B.N., the IODP Expedition 357 Science Party, 2018a. Alteration heterogeneities in peridotites exhumed on the southern wall of the Atlantis Massif (IODP Expedition 357). Journal of Petrology, 1–29 https://doi.org/10.1093/petrology/egy065.

Rouméjon, S.,Williams, M.J., Früh-Green, G.L., 2018b. In situ oxygen isotope analyses in serpentine minerals: constraints on serpentinization during tectonic exhumation at slow- and ultraslow-spreading ridges. Lithos 323, 156-173. https://doi.org/10.1016/j.lithos.2018.09.021.

Sack R.O., Ghiorso M.S., 1991. Chromian spinels as petrogenetic indicators: thermodynamic and petrological applications. American Mineralogist 76, 827-847.

Säntii, J., Kontinen, A., Sorjonen-Ward, P., Johanson, B., Pakkanen, L., 2006. Metamorphism and Chromite in Serpentinized and Carbonate-Silica-Altered Peridotites of the Paleoproterozoic Outokumpu-Jormua Ophiolite Belt, eastern Finland. International Geology Review 48, 494-546. https://doi.org/10.2747/0020-6814.48.6.494.

Saumur, B.M., Hattori, K. 2013. Zoned Cr-spinel and ferritchromite alteration in forearc mantle serpentinites of the Rio San Juan Complex, Dominican Republic. Mineralogical Magazine 77(1), 117-136. DOI: 10.1180/minmag.2013.077.1.11.

Schroeder, T., John, B.E., 2004. Strain localization on an oceanic detachment fault system, Atlantis Massif, 30° N, Mid-Atlantic Ridge. Geochemistry, Geophysics, Geosystems 5.

Schroeder, T., John, B.E., and Frost, B.R., 2002, Geologic implications of seawater circulation through peridotite exposed at slow-spreading mid-ocean ridges, Geology, v. 40, p. 367-370.

Shibata T., Thompson, G. 1986. Peridotites from the mid-Atlantic ridge at 43 °N and their petrogenetic relation to abyssal tholeiites. Contribution to Mineralogy and Petrology 93, 144-159.

Snow, J.E., Dick, H.J.B., 1995. Pervasive magnesium loss by marine weathering of peridotite. Geochimica et Cosmochimica Acta 59 (20), 4219-4235.

Spangenberg, K., 1943. Die Chromitlagerstatte von Tampadel am Zobten. Zeitschrift fur Praktische Geologie 51, 13-35.

Springer, G., 1971. Fluorescence by the X-ray continuum in multi-element targets: Falconbridge Nickel Mines Limited, Thornhill, Ontario, Canada, Report FRL-138, 14 p.

Starr, P., 2017. Sub-Greenschist to Lower Amphibolite Facies Metamorphism of Basalts: Examples from Flin Flon, Manitoba and Rossland, British Columbia. Ph.D. thesis, University of Calgary, 495 pp.

Stevens, R.E., 1944. Composition of some chromites of the Western hemisphere. American Mineralogist 29, 1-34.

Stewart, M.A., Karson, J.A., Klein, E.M., 2005. Four-dimensional upper crustal construction at fast-spreading mid-ocean ridges: a perspective from an upper crustal cross-section at the Hess Deep Rift. Journal of Volcanology and Geothermal Research 144, 287-309.

Su, Y., 2003. Global MORB chemistry compilation at the segment scale. Ph.D. Thesis. New York, Columbia University.

Suita, M.T., Streider, A.J., 1996. Cr-Spinels from Brazilian mafic - ultramafic complexes: metamorphic modifications. International Geology Review 38, 245-267.

Suhr, G., Hellebrand, E., Johnson, K., Brunelli, D., 2008. Stacked gabbro units and intervening mantle: a detailed look at a section of IODP Leg 305, Hole U1309D. Geochemistry, Geophysics, Geosystems 9. https://doi.org/10.1029/2008GC002012.

Suhr, G., Hellebrand, E., Snow, J.E., Seck, H.A., Hofmann, A.W., 2003. Significance of large, refractory dunite bodies in the upper mantle of the Bay of Islands Ophiolite. Geochemistry, Geophysics, Geosystems 4, 8605. doi:10.1029/2001GC000277.

Takazawa, E., Frey, F.A., Shimuzu, N., Obata, M., Bodinier, J.L., 1992. Geochemical evidence for melt migration and reaction in the upper mantle. Nature 359, 55-58.

Tucholke, B.E., Lin, J., Kleinrock, M.C., 1998. Megamullions and mullion structure defining oceanic metamorphic core complexes on the Mid-Atlantic Ridge. Journal of Geophysical Research 103, 9857-9866.

Van der Wal, D., Bodinier, J.-L., 1996. Origin of the recrystallisation front in the Ronda peridotite by km-scale pervasive porous melt flow. Contributions to Mineralogy and Petrology 122, 387-405.

Verlaguet, A., Bonnemains, D., Mével, C., Escartín, J., Andreani, M., Bourdelle, F., Boiron, M. - C., Chavagnac, V., 2021. Fluid circulation along an oceanic detachment fault: Insights from fluid inclusions in silicified brecciated fault rocks (Mid- Atlantic Ridge at 13°20′N). Geochemistry, geophysics, geosystems 22(1), 1–32. doi: 10.1029/2020GC009235.

Whattam, S.A., Cho, M., Smith, I.E.M., 2011. Magmatic peridotites and pyroxenites, Andong Ultramafic Complex, Korea: Geochemical evidence for supra-subduction zone formation and extensive melt–rock interaction. Lithos 127, 599-618.

Workman, R.K., Hart, S.R., 2005. Major and trace element composition of the depleted MORB mantle (DMM), Earth and Planetary Science Letters 231, 53–-72.

Zervas, C.E., Sempéré, J.-C., Lin, J., 1995. Morphology and crustal structure of a small transform fault along theMid-Atlantic Ridge: the Atlantis Fracture Zone. Marine Geophysical Researches 17, 275-300. https://doi.org/10.1007/BF01203466.

Figure 1 Click here to access/download;Figure;Fig. 1 PR2.pdf

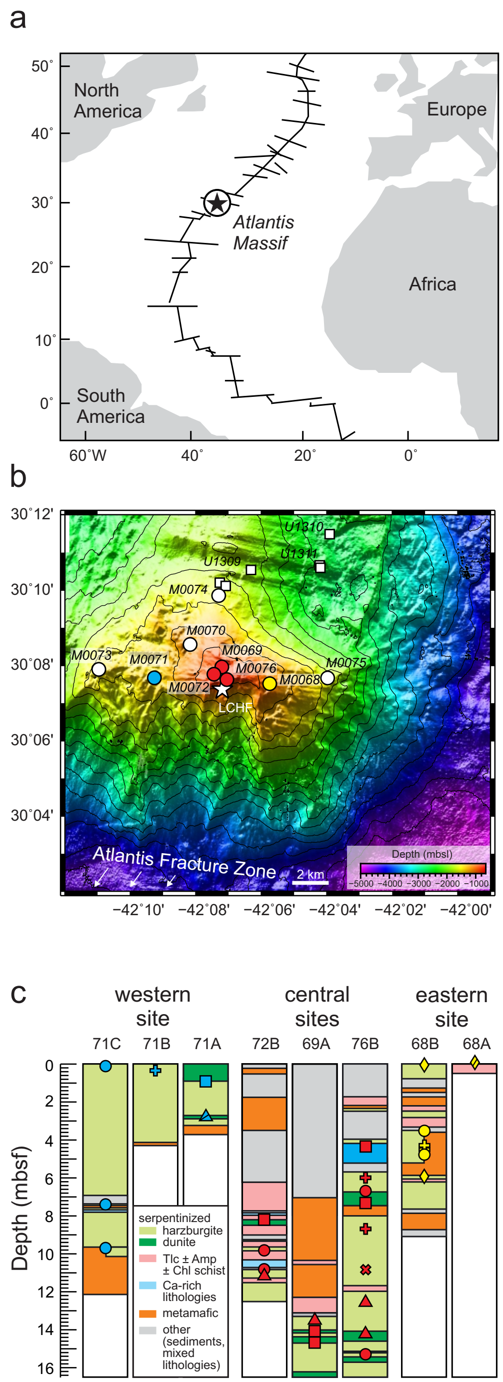

Figure 1 PR1 Whattam et al. (2021)

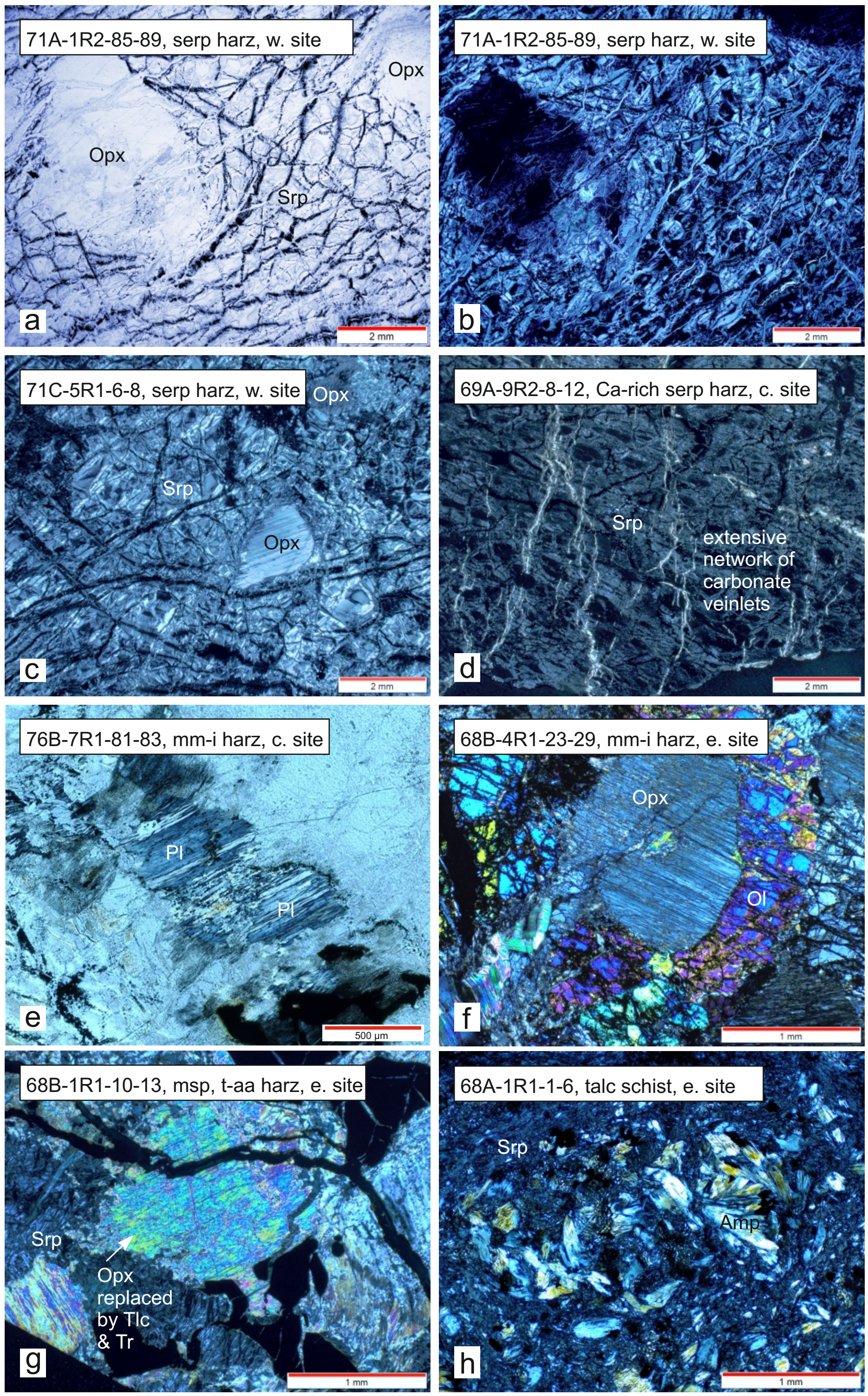

Figure 2 P-S 1A Whattam et al. (2021)

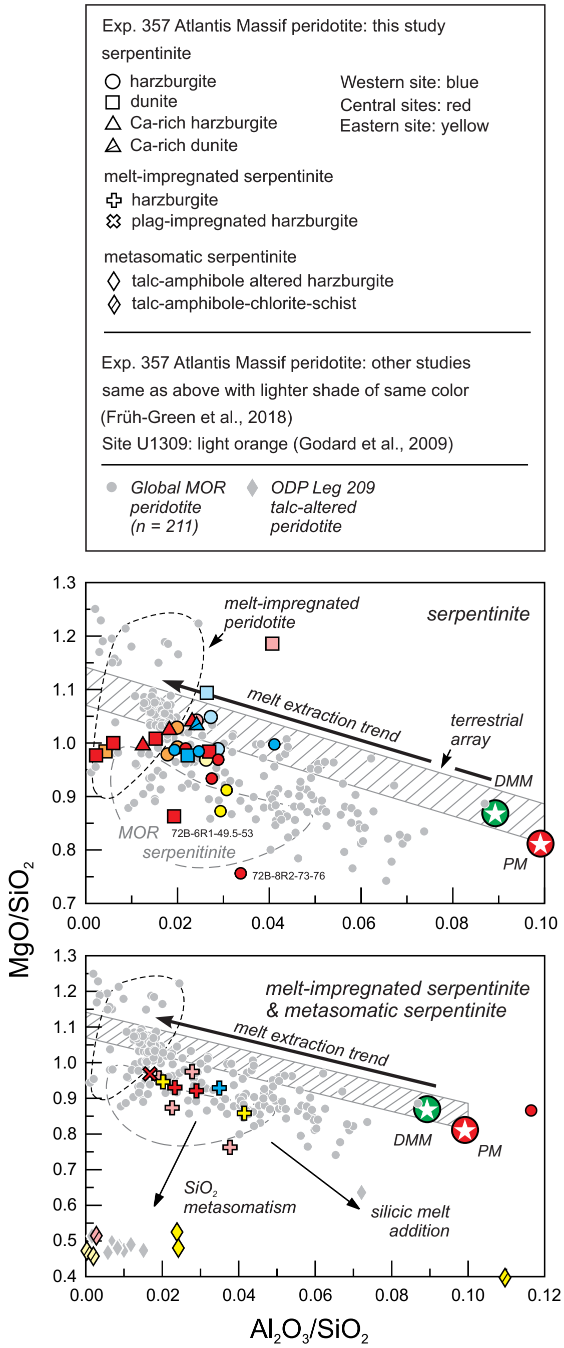

Figure 3 PR1 Whattam et al. (2021)

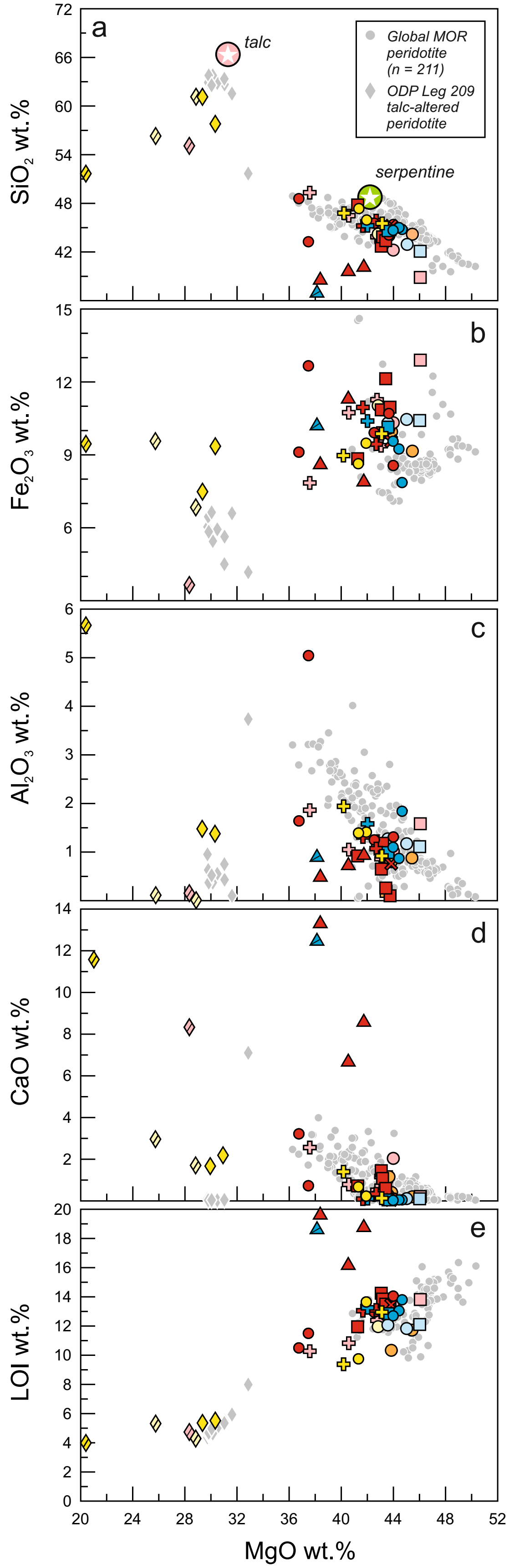

Figure 4 P-S 1A Whattam et al. (2021)

Figure 5

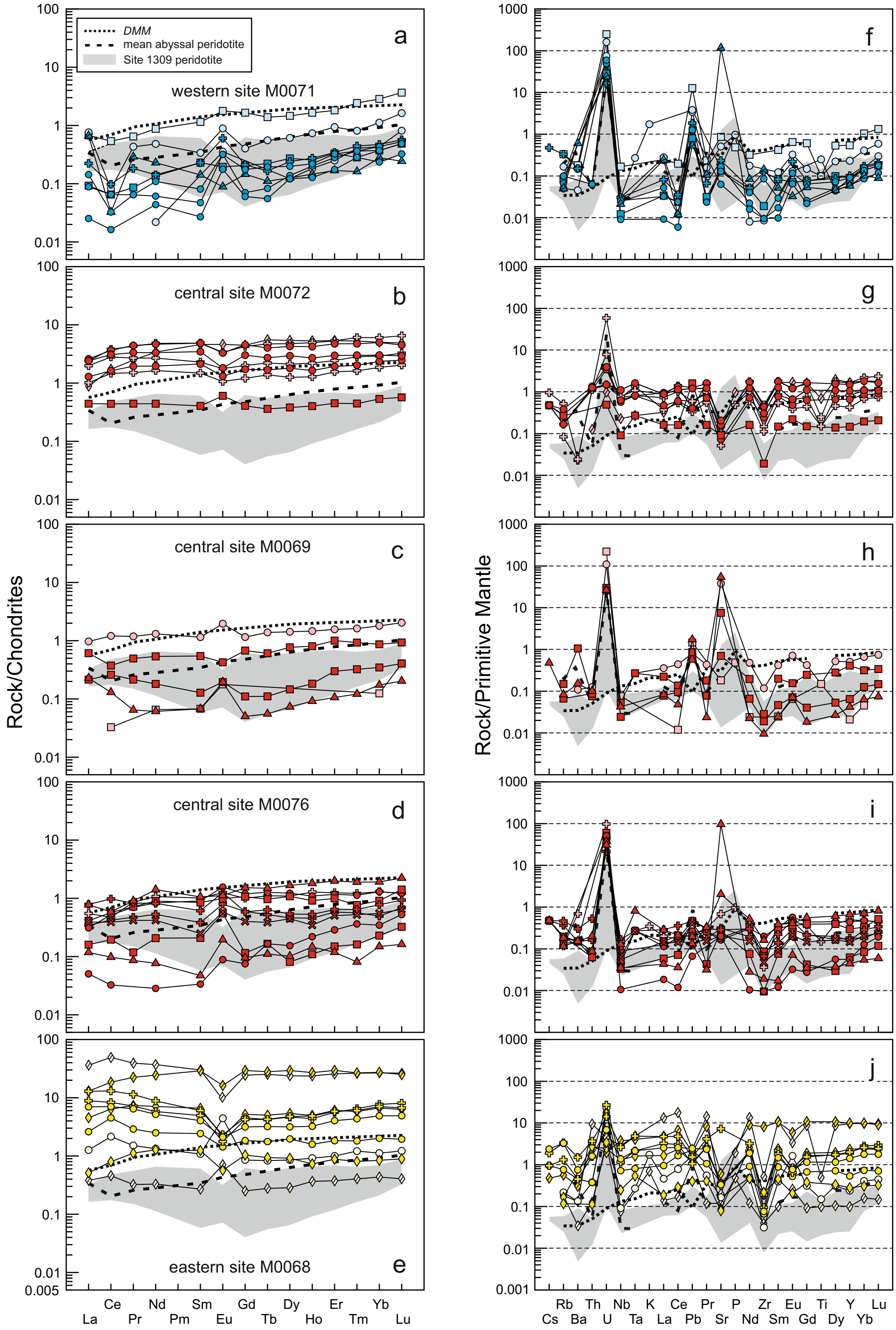

Figure 5 PR1 Whattam et al. (2021)

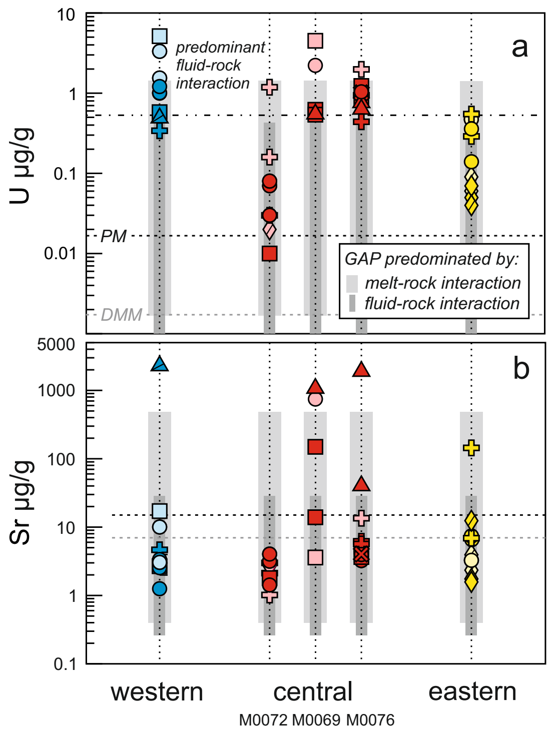

Figure 6 PR1 Whattam et al. (2021)

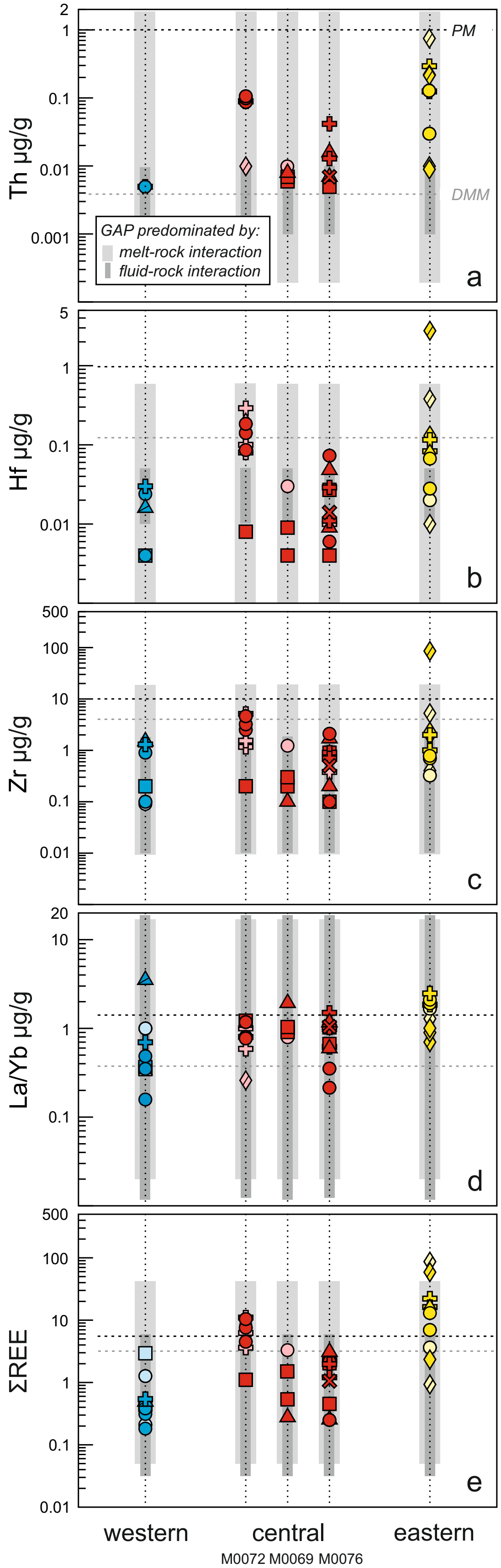

Figure 7 PR1 Whattam et al. (2021)

Figure 8 Click here to access/download;Figure;Fig. 8 PR2.pdf

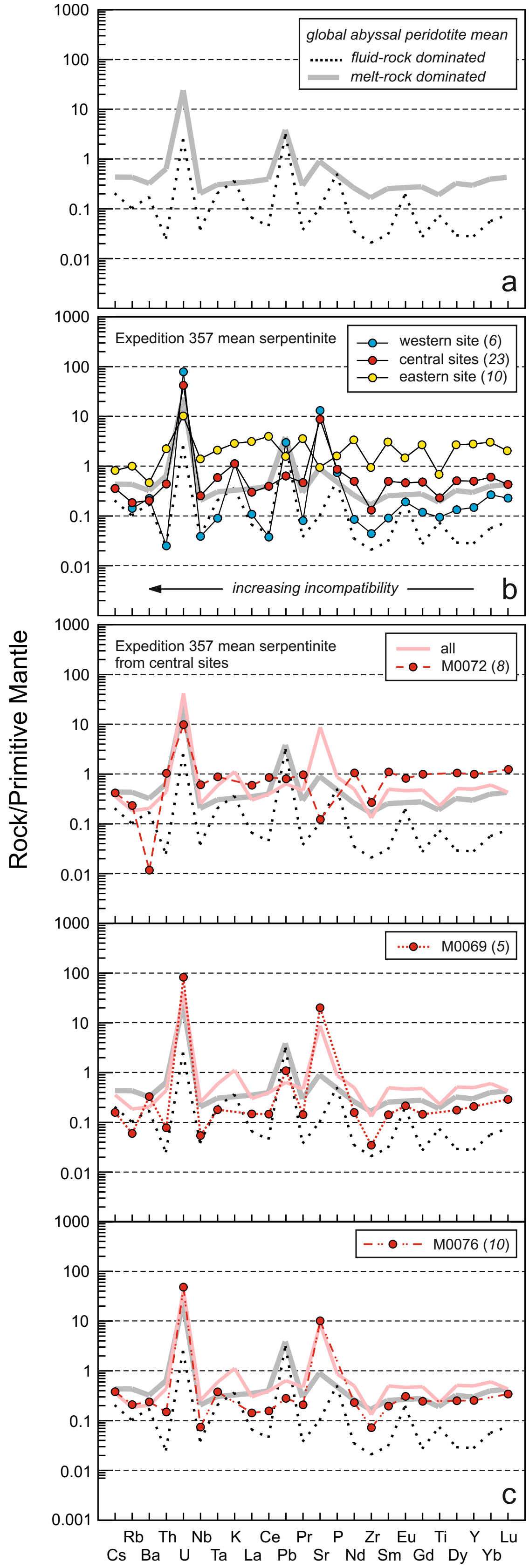

Figure 8 PR1 Whattam et al. (2021)

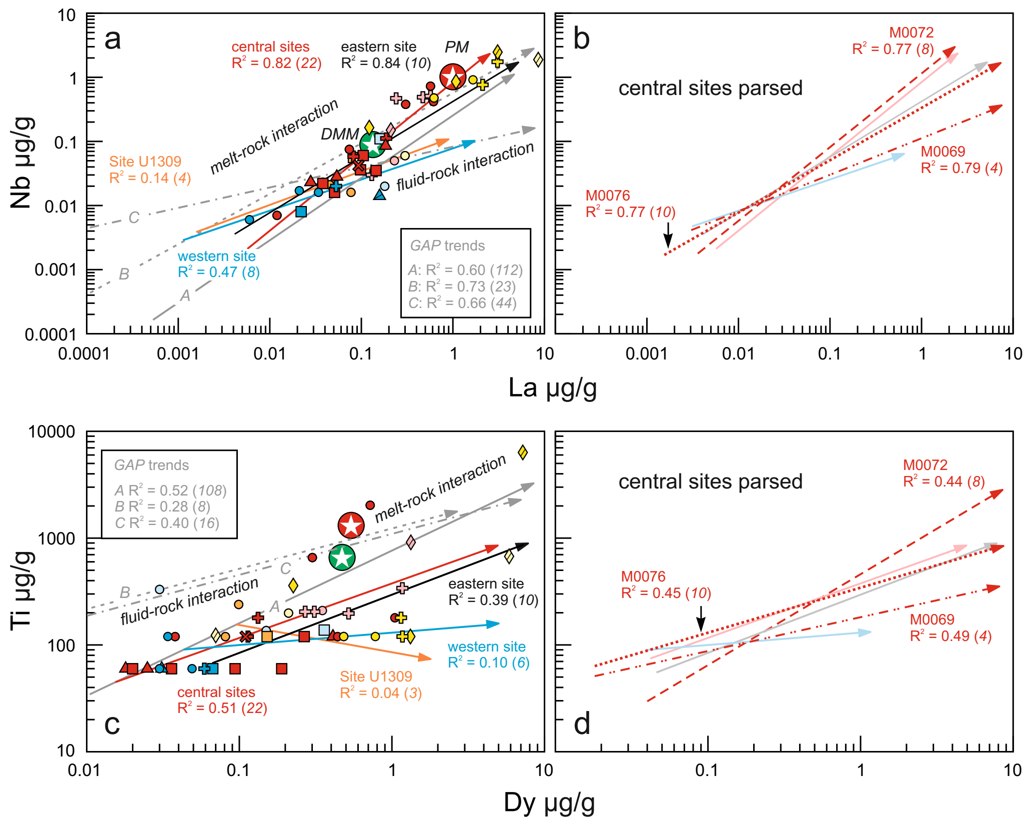

Figure 9 PR1 Whattam et al. (2021)

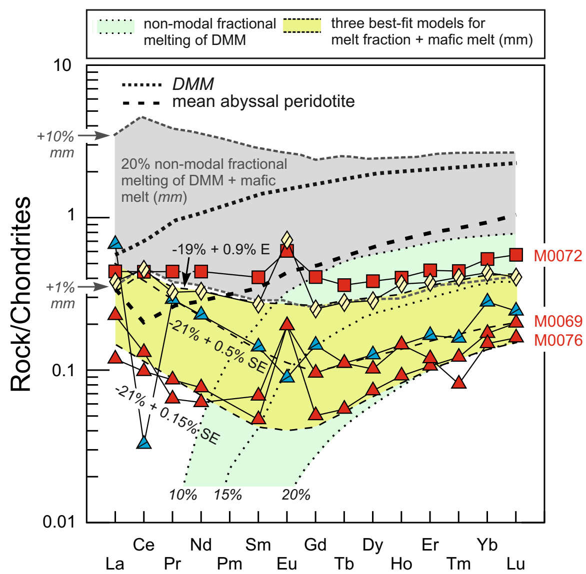

Figure 10 PR1 Whattam et al. (2021)

Table 1 Evidence and means for classification of Expedition 357 Atlantis Massif serpentinites subjected to melt-impregnation and (silica) metasomatism.

Site	Hole	Sample	Petrologic Type	Lithology	Evidence
western	M0071B	71B-1RCC-1-3	II	mm-i harzburgite	**macroscopic: presence of gabbro veins
central	M0072B	72B-7R1-76.5-79.5	II	*cryptically mm-i harzburgite	whole rock chemistry: incompatible element enrichment
		72B-8R2-23-26	II	cryptically mm-i harzburgite	whole rock chemistry: incompatible element enrichment
		72B-8R2-73-76	II	cryptically mm-i harzburgite	whole rock chemistry: incompatible element enrichment
	M0076B	76B-4R1-73-78	II	mm-i harzburgite	macroscopic: locally cut by mafic veins
		76B-6R1-65-68	II	mm-i harzburgite	macroscopic: presence of mafic melt intrusions
		76B-7R1-81-83	II	plagioclase-impregnated	petrographic: presence of rare plagioclase feldspar
eastern	M0068A	68A-1R1-1-6	III	talc-schist	petrographic: prevalence of secondary talc-amphibole whole rock chemistry: high SiO_2 (51.7 wt.%) , low MgO/SiO_2 (0.39), high Al_2O_3/SiO_2 (0.11)
	M0068B	68B-1R1-10-13	III	t-aa harzburgite	petrographic: talc-amphibole replacement of orthopyroxene whole rock chemistry: high SiO_2 (57.8 wt.%) , low MgO/SiO_2 (0.52)
		68B-4R1-23-29	II	mm-i harzburgite	petrographic: fresh olivine mantling orthopyroxene; olivine interpreted as recrystallized from mafic melt
		68B-4R1-45-49	II	mm-i harzburgite	macroscopic: presence of gabbro intrusions
		68B-6R1-8-10	III	t-aa harzburgite	petrographic: talc-amphibole replacement of orthopyroxene whole rock chemistry: high SiO_2 (61.1 wt.%) , low MgO/SiO_2 (0.48)

Notes:

Type I serpentinites (n = 20 of 29 total samples, see Table 3) are not listed as the only evidence for their classification is lack of melt-impregnation products and metasomatism. Type I includes the Ca-rich serpentinites (n = 4).

Abbreviations: mm-i, mafic melt-impregnated; t-aa, talc-amphibole altered.

Type II mm-i peridotite include plagioclase-impregnated peridotite.

*cryptically melt-impregnated refers to those peridotite which bear no evidence of impregnation at the scale of core or thin section (see text for further details).

**macroscopic evidence of mafic melt-impregnation determined by Expedition 357 Scientific Party at Onshore Scientific Party, University of Bremen, 2016 (see also Früh-Green et al., 2017, 2018).

Table 2

Table 2 Mineralogy and modalogy of Expedition 357 serpentinites.

Informal sample no.	Hole	Core	Interval (cm)	Top depth (m)	Bottom depth (m)	Unit	Site	Petrologic Type*	Rock type	Modal proportions (%)***			Notes
										Ol	Opx	Spl****	
19-QU	M0071C	1R1	6-10	0	2.68	1	W	I	serpentinized harzburgite	85	15	1-2	Spl ranges up to 4 mm
5-GT	M0071C	5R1	6-8	7.38	9.63	1	W	I	serpentinized harzburgite	80	20	2-3	Spl usually embedded in Opx
10-GT	M0072B	8R2	23-26	10.71	12.43	1	C	I	serpentinized harzburgite	75	25	3	Spl embedded in Opx
7-GT	M0069A	9R2	8-12	13.04	14.72	1	C	I	Ca-rich harzburgite	90	10	0	secondary carbonate veinlets (sub-mm) comprises ~5% by volume
2-QU	M0069A	9R2	103-106	13.04	14.72	4	C	I	serpentinized dunite	100	0	0	
8-QU	M0076B	3R1	78-82	3.44	5.16	3	C	I	serpentinized dunite	100	0	<1	
13-QU	M0076B	5R1	59-61	6.73	7.98	1	C	I	serpentinized dunite	100	0	0	
15-QU	M0076B	6R1	65-68	7.98	9.72	1	C	II	mm-i harzburgite	70	30	0	
11-GT	M0076B	7R1	81-83	9.72	11.15	1	C	II	plag-impreg. harzburgite	85	15	0	Pl present only as two ~500 µm discrete grains
14-GT	M0076B	9R1	96-100	12.87	14.59	1	C	III	Ca-rich harzburgite	85	15	3	secondary carbonate veinlets (sub-mm) comprises ~10% by volume
6-GT	M0068B	1R1	10-13	0	1.72	1	E	III	t-aa harzburgite	70	30	2	Spl embedded in Opx
19-GT	M0068B	4R1	23-29	4	5.72	2	E	II	mm-i harzburgite	75	25	2-3	secondary (replacive) Ol comprises ~5% by volume
12-QU	M0068B	4R1	45-49	4	5.72	3	E	II	mm-i harzburgite	90	10	0	
18-GT	M0068A	1R1	1-6	0	1.97	1	E	III	talc schist**	-	-	0	

Notes:

Abbreviations: mm-i, mafic melt-impregnated; t-aa, talc-amphibole altered; GT-GemTek; QU, Queen's University.

*Petrologic Types: I, serpentinites; II, melt-impregnated serpentinites; III, metasomatic serpentinites.

Type I includes Ca-rich serpentinites; Type II includes plagioclase-impregnated (plag-impreg.) serpentinites.

**The high abundances of HFSE (e.g., Ti, Nb, Zr, see Table 3) suggests the protolith of the talc schist was mafic.

***Modal proportions of the protolith are visually estimated.

****Spl is usually sub-mm.

Table 3 Whole rock chemical compositions of Expedition 357 serpentinites.

Hole	M0071C	M0071C	M0071C	M0071B	M0071A	M0071A	M0072B	M0072B	M0072B	M0072B	M0069A	M0069A	M0069A	M0076B	M0076B	M0076B	M0076B	M0076B	M0076B	M0076B	M0076B	M0076B	M0068B	M0068B	M0068B	M0068B	M0068B	M0068B	M0068A
Core	1R1	5R1	9R1	1RCC	1R1	1R2	6R1	7R1	8R2	8R2	9R2	9R2	10R2	3R1	4R1	4RCC	5R1	6R1	7R1	8R1	9R1	10R1	1R1	3R1	4R1	4R1	4R1	6R1	1R1
Interval (cm)	6-10	6-8	34-38	1-3	85-89	9-12	49.5-53	76.5-79.5	23-26	73-76	8-12	103-106	30-35	78-82	73-78	3-8	59-61	65-68	81-83	107.5-112.5	96-100	32.5-34.5	10-13	41-44	23-29	45-49	75-79	8-10	1-6
Top depth (m)	0	7.38	9.67	0	0	0	7.71	8.99	10.71	10.71	13.04	13.04	14.72	3.44	5.16	5.16	6.73	7.98	9.72	11.15	12.87	14.59	0	3.30	4	4	4	5.85	0
Bottom depth (m)	2.68	9.63	12.15	1.72	2.72	2.72	8.99	10.71	12.43	12.43	14.72	14.72	16.44	5.16	6.73	6.73	7.98	9.72	11.15	12.87	14.59	16.31	1.72	4	5.72	5.72	5.72	7.57	1.97
Unit	1	1	2	CC	2	MBIO	4	4	1	1	1	4	2	3	2	1	1	1	1	3	1	2	1	2	2	3	4	1	1
Site	W	W	W	W	W	W	C	C	C	C	C	C	C	C	C	C	C	C	C	C	C	C	E	E	E	E	E	E	E
Petrologic Type	I	I	I	II	I	I	I	I	I	I	I	I	I	I	II	I	I	II	II	I	I	I	III	I	II	II	I	III	III
Rock type (protolith)	serpentinized harzburgite	serpentinized harzburgite	serpentinized harzburgite	mm-i harzburgite	serpentinized dunite	Ca-rich dunite	serpentinized dunite	serpentinized harzburgite	serpentinized harzburgite	serpentinized harzburgite	Ca-rich harzburgite	serpentinized dunite	serpentinized dunite	serpentinized dunite	mm-i harzburgite	serpentinized harzburgite	serpentinized dunite	mm-i harzburgite	plag-impreg. harzburgite	Ca-rich harzburgite	Ca-rich harzburgite	serpentinized harzburgite	t-aa harzburgite	serpentinized harzburgite	mm-i harzburgite	mm-i harzburgite	serpentinized harzburgite	t-aa harzburgite	*talc schist
Major oxides wt.%																													
SiO_2	38.7	39.4	38.9	39.5	38.7	29.9	42.3	38.1	39.1	42.7	33.2	36.9	37.9	39.3	40.3	38.6	38.1	39.3	38.6	32.2	30.4	38.7	54.7	39.8	42.4	39.3	42.3	57.9	49.4
TiO_2	0.02	0.01	0.01	0.01	0.01	0.01	0.01	0.3	0.02	0.03	0.01	0.01	0.01	0.01	0.02	0.1	0.02	0.03	0.02	0.02	0.01	0.02	0.02	0.02	0.03	0.02	0.02	0.06	1.01
Al_2O_3	1.59	0.76	0.96	1.38	0.86	0.72	0.81	4.44	1.07	1.44	0.6	0.56	1.02	0.09	0.94	0.84	0.23	1.14	0.65	0.75	0.38	1.12	1.31	1.22	1.76	0.79	1.24	1.4	5.42
Fe_2O_3	6.79	8.09	8.33	9.08	8.8	8.26	7.82	11.15	8.51	8.01	9.47	9.37	8.56	9.62	8.3	9.37	10.65	9.52	8.16	6.33	6.78	7.3	8.85	8.21	8.13	8.52	7.71	7.08	9.04
CaO	0.04	0.04	0.03	0.1	0.04	10.1	0.64	0.64	0.19	2.83	5.59	1.25	0.93	0.07	0.3	0.07	0.53	0.08	0.04	6.88	10.5	0.12	0.57	0.2	1.27	0.11	0.6	0.08	9.56
MgO	38.6	38.9	38.3	36.7	37.8	30.9	36.5	33	36.5	32.3	34	37.2	37.3	38.4	37.5	38.2	38.1	36.2	37.4	33.5	30.3	37.5	28.7	36.3	36.4	37.2	36.9	27.8	19.5
Na_2O	0.15	0.06	0.07	0.18	0.13	0.15	0.06	0.08	0.04	0.19	0.19	0.2	0.16	0.11	0.09	0.12	0.02	0.12	0.04	0.06	0.12	0.07	0.16	0.24	0.23	0.08	0.13	0.13	1.08
K_2O	0.03			0.04	0.03	0.02					0.02	0.02	0.03					0.05					0.03	0.05	0.15	0.08	0.12	0.03	0.08
Cr_2O_3	0.44	0.23	0.43	0.28	0.3	0.58	0.27	0.26	0.34	0.31	0.63	0.31	0.39	0.07	0.32	0.18	0.04	0.39	0.34	0.22	0.18	0.36	0.23	0.36	0.1	0.12	0.2	0.16	0.14
MnO	0.08	0.07	0.07	0.07	0.07	0.14	0.08	0.08	0.08	0.09	0.06	0.56	0.09	0.13	0.11	0.06	0.1	0.09	0.08	0.32	0.05	0.07	0.05	0.19	0.12	0.08	0.11	0.05	0.18
P_2O_5				0.01	0.01	0.01		0.03			0.01	0.02	0.01						0.01	0.02	0.02	0.01	0.01	0.03	0.01	0.01		0.02	0.12
LOI	13.8	13.05	12.7	13.25	12.85	18.6	11.95	11.5	12.95	10.5	16.15	14.25	13.85	13.35	13.1	13.55	13.5	13.05	13.45	18.75	19.6	14.05	5.51	13.65	9.38	12.95	9.75	5.35	3.98
Total %	100.24	100.61	99.8	100.6	99.6	99.64	100.44	99.58	98.8	98.4	100.05	100.65	100.27	101.15	100.98	101.09	101.29	99.97	98.79	99.05	98.55	99.32	100.14	100.27	100	99.26	99.08	100.06	99.51
Mg#	*91.8*	*90.5*	*90.1*	*88.9*	*89.5*	*88.1*	*90.2*	*85.4*	*89.5*	*88.9*	*87.7*	*88.7*	*89.6*	*88.8*	*89.9*	*89*	*87.6*	*88.3*	*90.1*	*91.3*	*89.8*	*91.1*	*86.5*	*89.8*	*89.9*	*89.6*	*90.5*	*88.6*	*81.0*
MgO/SiO_2	*1.00*	*0.99*	*0.98*	*0.93*	*0.98*	*1.03*	*0.86*	*0.87*	*0.93*	*0.76*	*1.02*	*1.01*	*0.98*	*0.98*	*0.93*	*0.99*	*1.00*	*0.92*	*0.97*	*1.04*	*1.00*	*0.97*	*0.52*	*0.91*	*0.86*	*0.95*	*0.87*	*0.48*	*0.39*
Al_2O_3/SiO_2	*0.04*	*0.02*	*0.02*	*0.03*	*0.02*	*0.02*	*0.02*	*0.12*	*0.03*	*0.03*	*0.02*	*0.02*	*0.03*	*0.00*	*0.02*	*0.02*	*0.01*	*0.03*	*0.02*	*0.02*	*0.01*	*0.03*	*0.02*	*0.03*	*0.04*	*0.02*	*0.03*	*0.02*	*0.11*
Trace elements (μg/g)																													
Sc	14.55	9.67	8.69	10.65	9.54	3.63	8.31	14.85	9.16	10.25	3.9	6.56	10.15	2.9	6.66	6.37	2.67	9.84	5.47	7.11	4.99	11.35	8.53	9.32	4.66	4.52	9.84	6.72	31.2
V	74.3	36.2	37.3	52.4	39.4	45.1	24.5	85.1	32.2	38.1	28.7	28.2	33.5	20.9	37	36.8	18.1	53.9	36.5	32.5	14.5	39.2	29.6	44.8	12.9	11.3	33.9	29.1	174.5
Cr	1900	1015	1670	1325	1145	2620	1250	1395	1715	1650	2840	1295	1640	292	1385	793	168.5	1635	1755	849	738	1500	1085	1325	398	409	1060	757	706
Ni	1290	1700	2630	1210	1720	1030	2130	1915	2080	2010	2210	2270	1925	2000	1995	1705	1820	1910	2210	1590	1930	2270	1250	1510	2200	2050	2180	1275	698
Li	1.6	5.2	1.4	10.8	2.9	0.4	1.6	6.5	1.3	1.1	0.8	2.8	5.2	5.5	6.7	2.2	1.4	6.4	4.7	2.3	1.2	3.5	3.5	18.1	7.7	5.5	7.3	8	19.6
Co	68	63.8	110.5	81.1	84.1	96.1	93.3	112.5	100.5	91.4	114	107.5	84.7	90.8	87.1	49.2	70.8	104	113.5	67	78.9	102	64.4	99.3	116.5	97	106	75.9	51.3
Cu	14.4	18.85	44.4	28.9	9.95	8.84	0.54	3.04	0.69	0.75	5.24	2.05	1.97	2.18	1.83	54	1.73	1.13	2.12	2.25	2.76	2.71	33.1	28.4	8.36	7.06	9.2	0.4	109
Zn	54.7	42.1	54.1	50.8	40.3	195.5	12.2	18.1	15.6	12	49.4	34.1	39	29.1	25.9	23.3	21.9	25.4	29.3	17.4	29.5	35.3	36.7	102.5	49	46	46.1	51.2	69.4
Ga	1.48	0.72	0.94	2.18	1.12	1.02	1.61	5.77	1.96	2.61	1.6	1.14	1.16	0.36	1.66	1.97	0.52	1.64	1.29	0.96	0.47	1.06	2.65	1.89	3.19	1.77	2.12	2	11
Rb	0.04	0.06	0.06	0.2	0.05	0.03	0.16	0.1	0.17	0.23	0.05	0.09	0.04	0.11	0.22	0.12	0.08	0.28	0.12	0.11	0.07	0.08	0.1	0.46	2.01	0.79	1.98	0.07	0.34
Sr	3.37	2.56	1.26	4.68	2.69	2320	1.82	4.1	1.44	3.22	1080	14	150.5	5.31	6.24	3.26	3.67	5.71	4.06	40.6	1925	4	1.75	7.42	145	6.91	6.64	1.58	12.45
Y	0.31	0.39	0.26	0.44	0.39	0.25	0.63	4.53	2.86	6.44	0.18	1.77	0.28	0.27	0.78	1.9	1.28	0.68	0.63	2.84	0.19	0.24	10.15	2.32	8.23	8.66	6.13	1.21	42.7
Zr	0.1	0.9	0.1	1.3	0.2	1.5	0.2	3.2	2.5	4.6	0.1	0.3	0.2	0.1	0.9	2.1	0.9	0.7	0.5	1.7	0.2	0.1	2	0.7	1	2	0.8	2.3	85.6
Nb	0.016	0.017	0.006	0.02	0.008	0.014	0.06	0.726	0.378	0.417	0.028	0.035	0.016	0.022	0.058	0.075	0.036	0.111	0.042	0.085	0.023	0.007	0.855	0.476	1.75	0.763	0.914	0.164	2.47
Mo	0.36	0.09	0.21	0.31	0.17	1.68	0.04	0.12	0.11	0.07	0.3	1.37	0.42	0.98	0.52	0.31	0.49	0.19	0.41	0.62	0.12	0.07	0.09	0.84	0.2	0.16	0.17	0.03	0.22
Cd	0.032	0.021	0.005	0.024	0.028	0.015	<0.005	0.007	<0.005	0.007	0.008	0.019	0.011	0.03	0.056	0.024	0.032	0.03	0.027	0.193	0.013	0.025	<0.005	0.036	0.045	0.041	0.03	0.011	<0.005
Sn	0.14	0.06	0.07	0.24	0.05	0.1	0.06	0.27	0.14	0.3	0.24	0.07	0.12	0.06	0.07	0.12	0.08	0.1	0.08	0.1	0.11	0.13	0.8	0.69	1.31	0.98	1.48	0.12	3.46
Sb	0.37	0.14	0.04	0.46	0.2	1.04	0.05	0.06	0.04	0.03	0.04	0.08	0.09	0.27	0.08	0.19	0.07	0.03	<0.02	0.08	0.08	0.1	0.06	0.4	0.13	0.08	0.08	0.03	0.07
Cs	<0.01	<0.01	<0.01	0.01	<0.01	<0.01	0.01	0.01	0.01	0.01	0.01	<0.01	<0.01	<0.01	0.01	<0.01	<0.01	0.01	0.01	0.01	<0.01	<0.01	<0.01	0.02	0.04	0.02	0.05	<0.01	0.01
Ba	<1	<1	<1	1	<1	4	<1	<1	<1	<1	1	7	<1	1	1	<1	1	2	1	1	1	<1	<1	3	10	3	5	<1	2
La	0.034	0.021	0.006	0.053	0.022	0.158	0.105	0.57	0.305	0.615	0.054	0.145	0.051	0.038	0.082	0.074	0.098	0.187	0.093	0.184	0.028	0.012	1.08	0.621	3.07	2.11	1.66	0.122	3.08
Ce	0.02	0.04	0.01	0.06	0.04	0.02	0.27	1.89	1	2.24	0.08	0.23	0.16	0.12	0.26	0.32	0.35	0.6	0.24	0.36	0.06	0.02	3.93	2.77	8.04	5.12	4.33	0.49	11.35
Pr	0.006	0.006	bdl	0.017	0.008	0.027	0.041	0.309	0.181	0.411	0.006	0.046	0.02	0.011	0.044	0.065	0.067	0.077	0.039	0.084	0.008	bdl	0.686	0.27	1.06	0.669	0.6	0.104	2.08
Nd	0.028	0.05	0.02	0.065	0.062	0.105	0.202	1.52	0.895	2.13	0.028	0.246	0.083	0.095	0.243	0.383	0.412	0.376	0.192	0.647	0.035	0.013	3.25	1.145	4.04	2.66	2.38	0.585	11.2
Sm	0.007	0.012	0.004	0.034	0.034	0.021	0.06	0.512	0.315	0.718	0.01	0.081	0.019	0.031	0.057	0.134	0.126	0.091	0.037	0.157	0.007	0.005	0.982	0.36	0.893	0.733	0.601	0.184	4.29
Eu	0.018	0.018	0.01	0.034	0.011	0.005	0.034	0.102	0.074	0.186	0.011	0.024	0.011	0.031	0.045	0.088	0.056	0.071	0.033	0.063	0.011	0.005	0.122	0.081	0.131	0.1	0.119	0.032	0.912
Gd	0.014	0.035	0.012	0.042	0.041	0.029	0.081	0.599	0.343	0.903	0.01	0.135	0.022	0.023	0.119	0.239	0.213	0.117	0.08	0.304	0.019	0.015	1.035	0.367	0.905	0.843	0.63	0.207	5.86
Tb	0.003	0.007	0.002	0.006	0.008	0.004	0.013	0.098	0.061	0.145	0.002	0.022	0.004	0.006	0.019	0.046	0.035	0.023	0.014	0.054	0.004	0.006	0.182	0.064	0.153	0.154	0.116	0.034	1.01
Dy	0.034	0.049	0.03	0.059	0.067	0.031	0.094	0.723	0.442	1.05	0.018	0.19	0.036	0.02	0.114	0.302	0.267	0.133	0.11	0.412	0.025	0.038	1.325	0.484	1.15	1.175	0.78	0.226	7.23
Ho	0.011	0.012	0.007	0.015	0.014	0.008	0.022	0.147	0.09	0.231	0.005	0.044	0.01	0.006	0.025	0.06	0.05	0.029	0.019	0.099	0.008	0.012	0.272	0.087	0.24	0.266	0.177	0.04	1.475
Er	0.045	0.052	0.028	0.055	0.053	0.027	0.072	0.477	0.309	0.756	0.017	0.161	0.048	0.024	0.093	0.188	0.16	0.103	0.081	0.319	0.019	0.046	0.975	0.294	0.902	0.938	0.649	0.141	4.72
Tm	0.009	0.009	0.007	0.011	0.007	0.004	0.011	0.074	0.05	0.117	0.003	0.023	0.008	0.004	0.014	0.028	0.019	0.016	0.013	0.047	0.002	0.009	0.144	0.045	0.161	0.149	0.108	0.02	0.66
Yb	0.07	0.06	0.038	0.076	0.06	0.045	0.086	0.484	0.38	0.798	0.028	0.14	0.056	0.037	0.08	0.21	0.147	0.125	0.089	0.309	0.024	0.056	1.075	0.325	1.24	1.14	0.79	0.136	4.4
Lu	0.013	0.012	0.008	0.014	0.012	0.006	0.014	0.072	0.061	0.111	0.005	0.023	0.01	0.008	0.017	0.03	0.035	0.023	0.016	0.055	0.004	0.013	0.156	0.048	0.199	0.165	0.121	0.022	0.617
Hf	0.004	0.024	<0.004	0.03	0.004	0.016	0.008	0.141	0.086	0.184	<0.004	0.009	0.004	0.004	0.029	0.073	0.027	0.011	0.014	0.048	0.009	0.006	0.131	0.028	0.083	0.116	0.067	0.077	2.76
Ta	<0.01	<0.01	<0.01	<0.01	<0.01	<0.01	0.01	0.06	0.03	0.03	<0.01	0.01	<0.01	<0.01	<0.01	0.01	<0.01	0.01	0.01	0.03	<0.01	<0.01	0.06	0.03	0.18	0.08	0.08	0.02	0.15
Pb	0.21	0.18	0.19	0.28	0.12	0.08	0.24	0.18	0.06	0.06	0.26	0.09	0.13	0.07	0.02	0.04	0.03	0.07	0.06	0.03	0.02	0.01	0.17	0.34	0.23	0.16	0.37	0.06	0.3
Th	<0.004	0.005	<0.004	0.005	<0.004	<0.004	<0.004	0.1	0.088	0.107	0.008	0.006	0.007	<0.004	0.013	0.005	0.005	0.042	0.007	0.016	0.007	<0.004	0.215	0.03	0.294	0.125	0.128	0.009	0.221
U	1	1.01	1.21	0.34	0.58	0.49	0.01	0.03	0.07	0.08	0.54	0.61	0.53	1.23	0.94	0.91	0.82	0.44	1.01	0.76	0.63	1.04	0.05	0.36	0.29	0.55	0.14	0.07	0.04

Notes:

bdl, below detection limit.

abbreviations: mm-i, mafic melt-impregnated; t-aa, talc-amphibole altered.

Type I serpentinites include Ca-rich serpentinites; Type II mm-i serpentinites include plagioclase-impregnated (plag-impreg.) serpentinites.

*Protolith of the schist is probably mafic (compare HFSE concentrations with remaining samples).

Supplementary file

Click here to access/download
Supplementary file
Archive.zip

Declaration of interests

☒ The authors declare that they have no known competing financial interests or personal relationships that could have appeared to influence the work reported in this paper.

☐The authors declare the following financial interests/personal relationships which may be considered as potential competing interests: